DISSERTATION

Consequences of the CMR Effect in EELS by using TEM

ausgeführt zum Zwecke der Erlangung des akademischen Grades eines
Doktors der technischen Wissenschaften
unter der Leitung von

Priv.Doz. Dr.techn. Dipl.-Ing. Michael Stöger-Pollach, MInstP

E057-02
Universitäre Service-Einrichtung für Transmissions-Elektronenmikroskopie

E138
Institut für Festkörperphysik

eingereicht an der Technischen Universität Wien
Fakultät für Physik

von

Dipl.-Ing. Wolfgang Wallisch, BSc
Matr.Nr.: 0725346

Wien, im Mai 2019

Kurzfassung

In den vergangenen Jahrzehnten wurde die Forschung und Entwicklung von immer kleineren und leistungsfähigeren Geräten intensiviert. Vielversprechende Kandidaten in der Nanotechnologie sind die Dünnschichtmetalloxide $La_{0.8}Sr_{0.2}MnO_3$ und La_2CoMnO_6. Aufgrund ihres breiten Spektrums an physikalischen und chemischen Eigenschaften sind diese Doppelperovskitoxide von besonderem Interesse. Das Forschungsprojekt FOXSI untersucht die Oberflächenchemie sowie -physik von Oxiden und deren Struktur-Funktions-Beziehung. Diese Arbeit befasst sich im Rahmen von FOXSI mit den Auswirkungen des kolossalen Magnetowiderstandseffekts in der Elektronen-Energieverlustspektrometrie im Transmissionselektronenmikroskop an Doppelperovskitoxiden. Die Auswirkungen auf das untersuchte Material spiegeln Änderungen der Magnetisierung sowie des Widerstands wider.

Die besondere Eigenschaft eines Doppelperovskitmanganits ist sein enorm negativer Magnetowiderstand in der Gegenwart eines magnetischen Feldes. Dieser Effekt wird auch kolossaler Magnetowiderstandseffekt genannt. Durch das Einschalten eines externen Magnetfelds kommt es zu einem Metall-Isolator-Übergang. Die Untersuchung von $La_{0.8}Sr_{0.2}MnO_3$ und La_2CoMnO_6 mittels des Transmissionselektronenmikroskops ermöglicht die Analyse des kolossalen Magnetowiderstandseffekts mit sehr hoher räumlicher Auflösung und bietet neue Möglichkeiten in der Nanotechnologie.

Strukturelle, dielektrische, elektronische sowie magnetische Eigenschaften können mit der Kombination aus Transmissionselektronenmikroskopie und Elektronen-Energieverlustspektrometrie im Nanometerbereich ermittelt werden. Wie die Untersuchungen im Transmissionselektronenmikroskop zeigen, wird der kolossale Magnetowiderstandseffekt von der bei der Probenherstellung entstandenen Mikrostruktur und ihren Inhomogenitäten (z. B. Gitterfehlanpassungen zwischen Substrat und Dünnschicht) beeinflusst. Er ist daher sensitiv gegenüber induzierter Spannung in der Grenzfläche. Die Mikrostruktur der untersuchten Probe hat ebenfalls Einfluss auf die gemessenen Spektren im Niedrigenergieverlustbereich und dies führt zu einer Änderung der Bandlücke. Eine Methode zur Bestimmung von Bandlücken und dielektrischen Eigenschaften ist die Valenzelektronenspektrometrie. Die Messungen mittels Valenzelektronenspektrometrie zeigen bei Anlegung eines externen Magnetfelds von etwa 0,9 T und durch Änderung der Temperatur von Raumtemperatur auf 85 K eine Verschiebung eines Interbandübergangs um 0,14 eV. Optische Materialeigenschaften von La_2CoMnO_6 wurden mittels Ellipsometer gemessen und anschließend mit Hilfe der Kröger Gleichung in Relation zu den Ergebnissen aus der Valenzelektronenspektrometrie gesetzt. Außerdem wurden Dichte-Funktional-Theorie Simulationen unter Verwendung des WIEN2k Codes und seines Pakets OPTICS zur Unterstützung der experimentellen Ergebnisse durchgeführt. Das magnetische Verhalten der Proben wurde im Transmissionselektronenmikroskop anhand von Messungen des magnetischen Zirkulardichroismus unterhalb und oberhalb der Curie Temperatur untersucht. Dabei wurde ein magnetisches Moment bei 85 K gemessen, während bei Raumtemperatur kein magnetisches Verhalten der Probe festgestellt wurde.

In dieser Arbeit wurde durch Kombination von Valenzelektronenspektrometrie und Messungen des magnetischen Zirkulardichroismus im Transmissionselektronenmikroskop ein neuer Ansatz entwickelt um die Konsequenzen des kolossalen Magnetowiderstandseffektes im Nanometerbereich zu messen.

Abstract

Nowadays, new electronic and electrical devices have to be stronger, more efficient and of course smaller to manage the needs of nanotechnology. Thin film metal oxides, for example $La_{0.8}Sr_{0.2}MnO_3$ and La_2CoMnO_6, are promising candidates. These double perovskite oxides are of great interest due to their large spectrum of diverse physical and chemical properties. The research project FOXSI aims to understand the surface chemistry and physics as well as the structure-function relationship with respect to smaller scales, which generally deviate from the bulk characteristics. As a part of FOXSI, this thesis aims to detect changes of magnetisation and resistivity on thin films to describe the consequences of the colossal magnetoresistance in electron energy loss spectrometry by using transmission electron microscopy.

Double perovskite manganites show a huge negative magnetoresistance when applying an external magnetic field. The resulting metal-insulator transition is also known as the colossal magnetoresistance effect. Hence, the behaviour of the colossal magnetoresistance effect on $La_{0.8}Sr_{0.2}MnO_3$ and La_2CoMnO_6 in the nanometre scale is interesting to investigate by transmission electron microscopy.

A transmission electron microscopy combined with an electron energy loss spectrometer offers structural, dielectric, electronic and magnetic measurements with high spatial resolution. The colossal magnetoresistance effect is sensitive to changes within the microstructure, e.g. to the lattice misfit between substrate and thin film and thus the induced strain in the interface. The characteristics of the microstructure influence the performance of measured low loss spectra and lead to a bandgap variation. In particular, valence electron energy loss spectrometry is a method to determine the bandgap and characterise the dielectric properties. An interband transition shift of 0.14 eV was determined for La_2CoMnO_6 at an external magnetic field of around 0.9 T and by changing the temperature from room temperature to 85 K. The results of valence electron energy loss spectrometry were compared with data that was measured by an ellipsometer and simulated on the basis of the Kröger equation. Additionally, the experimental results are supported by numerical density functional theory simulations using the WIEN2k code and its package OPTICS. The magnetic behaviour of the specimens is observed with chemical sensitivity by energy-loss magnetic circular dichroism below and above the Curie temperature. Even magnetic moments are detected at 85 K, while at room temperature no magnetic behaviour is measured.

In conclusion, a new approach was developed to detect the consequences of the colossal magnetoresistance effect in the nanometre scale by valence electron energy loss spectrometry and energy-loss magnetic circular dichroism in transmission electron microscopy.

Acknowledgements

It is a pleasure for me to thank those who accompanied me on my way and kindly supported me with suggestions. First of all, I owe my deepest gratitude to my supervisor Dr. Michael Stöger-Pollach and the head of USTEM Prof. Johannes Bernardi for giving me the opportunity to work at this great institute and the project FOXSI. In particular, I want to thank Michael for his technical and advisory discussions, his prevision, patience and inspiring my interest to develop a new approach. Special thanks to Johannes for the support and possibility to gain many great experiences at conferences and workshops all over the world. Furthermore, I would like to express my gratitude to Prof. Karin Föttinger and Prof. Andreas Hütten for reviewing this thesis.

My deepest appreciation goes to Prof. Stefan Löffler for our never-ending discussions on VEELS and EMCD as well as your helpful advice. In addition, my special thanks are extended to Dipl.-Ing. Andreas Steiger-Thirsfeld, Jakob Gruber and the whole USTEM team for the support with the TEM sample preparation and the great work environment in our group.

Moreover, I want to thank Dr. Edvinas Navickas and the group of Prof. Jürgen Fleig for the thin film synthesis. Also many thanks to Viktoria Ritter, MSc for supporting me with optical measurements on the ellipsometer. For the support during the TEM measurements at CEITEC I want to express my thanks to Ing. Michal Horák. I also acknowledge financial support by the Austrian Science Fund (FWF, F4501-N16), the Austrian Society for Electron Microscopy, the European Microscopy Society, the TU Wien and of course, USTEM.

For the fruitful discussions and learning many aspects of WIEN2k I would like to offer my special thanks to Dipl.-Ing. Ahmad Asali and Dipl.-Ing. Stephan Sorta.

To my friends and family thank you for your faithful support and being around. Above all I want to thank Dipl.-Ing. Katharina Lebiedzinski and my special friend Blacky. Without your tireless support, encouragement and endless love this way would not have been possible. Words cannot express how grateful I am to have you in my life.

Preface

The title for the first draft *The mystery case of the CMR effect* of the present work reminds of a literary crime novel. This genre is focused on the systematic processing of the crime starting with the observation followed by some assumptions and detections, and finally the unbundling of mystery. Curiously, the storyline of a crime novel does not significantly differ from a scientific work. It will start with the description of the frame story...

The knowledge of thin film oxide characteristics opens new ways to manage the needs of modern technologies. Progresses in the field of nanotechnology rely on a fundamental understanding of the surface chemistry and physics, and the identification of structure-function relationships. Metal oxides are promising candidates and multilateral group of materials with the applicable properties to fulfil the expectations of modern nanotechnologies. Over the past years, a lot of research has been done in this area and a project which is occupied with this research is FOXSI. The name FOXSI is composed of Functional OXide Surfaces and Interfaces. The concerns of FOXSI are centred around the structure of functional oxide surfaces and interfaces, the gas-oxide interactions and the functional oxides under working conditions. This thesis was accomplished within the scope of FOXSI at the University Service Center for Transmission Electron Microscopy.

The investigation by electron microscopy provides a comprehensive range of experimental opportunities as the determination of the nanostructure, crystallography, chemical analysis, electronic, optical and magnetic properties. In particular, transmission electron microscopy has a extensive spectrum of applications beside the investigation of the nanostructure with high spatial resolution. A huge variety of analytical methods are available to study the characteristics of the specimen in nanometre scale. The electron energy loss spectrometry combined with transmission electron microscopy offers great insights in electronic, optical and magnetic properties of the specimen.

A novel approach for detecting the consequences of the colossal magnetoresistance effect in the nanometre range by means of electron energy loss spectrometry in transmission electron microscopy is presented in this work beside the classical transmission electron microscopy investigations for the FOXSI project partners. In collaboration with project partners new outcomes were successfully published and are described within this work being an important part of the author's work at University Service Center for Transmission Electron Microscopy.

Contents

Chapter 1

Introduction

This thesis offers an overview of electron energy loss spectrometry (EELS) and its applications in transmission electron microscopy (TEM) with respect to analyse the consequences of the colossal magnetoresistance (CMR) effect using La_2CoMnO_6 (LCMO).

First, the introduction provides an access to the scientific discovery and the achievements of the CMR effect and its specific characteristics on double perovskites over the years. It describes the necessity of a local CMR study on nanometre scale and introduces a novel approach to analyse the CMR effect on thin films in TEM. The second chapter refers to the theoretical background and completes the elementary knowledge of both, the CMR effect and the inelastic scattering theory. In the third chapter the applied methods and the materials are presented. Chapter four gives an overview of the collaboration work within FOXSI and highlights the published outcomes. The next two parts are focussed on applications and results of the core techniques, which are valence electron energy loss spectrometry (VEELS) (chapter 5) and energy-loss magnetic circular dichroism (EMCD) (chapter 6). Finally, chapter seven summarises the main results, reviews the applicability of the new approach and concludes the major achievements.

1.1 Motivation

In the 1950s the CMR effect was discovered by Jonker and Van Santen [1]. It was observed during an investigation of perovskite manganite pellets with an apparatus for measuring magnetic moments [2]. A transition at the Curie temperature (T_C)

from antiferromagnetic to ferromagnetic by reducing the temperature was detected and attributed to the indirect exchange interaction of Mn^{3+} and Mn^{4+}. Further investigations of these manganite oxides by Volger [3] exhibit apart from this characteristic property the specific resistance and the magnetoresistance in the presence of a magnetic field. It is reported that a metal-insulator transition is achieved when the temperature is changing from approximately 100 K to over 300 K. This process is connected to a transition from the ferromagnetic to the paramagnetic state.

Several years later, an amplification of this effect with the usage of stronger magnetic fields was measured by Kusters et al. [4] and for thin films by Helmolt et al. [5]. The application of strong magnetic fields enables the determination of a rapid resistivity decrease. The resulting large negative magnetoresistance is known as CMR.

These days, the double perovskite LCMO is a promising candidate for a wide variety of applications due to its magnetic [6], electric [7], dielectric [8], magnetoelectric [9] and magnetoresistant [10] properties. Thin film metal oxides and especially double perovskite manganites have been of great interest in many fields such as cathodes of solid oxide fuel cells [11], magnetic storage and magnetic field sensing functions at room temperature (RT) [12]. The requirements to new electric, electronic and magnetic devices are to be smaller, stronger and more efficient compared to the previous model. The preparation of thin films has a great advantage compared to other techniques. The specimen synthesis requires less row material, which is cost saving and contributes to a sustainable use of resources. Functional oxides are used in devices that are in every day use. The size of the devices is getting smaller and smaller. Knowing this fact it is important to consider the structural, physical and chemical properties of functional oxides in smaller scales, which generally deviate from the bulk characteristic. Hence, it is of great interest to investigate the consequences of the CMR effect and the behaviour of the sample in smaller ranges.

The specific characteristics of LCMO like the relation between the magnetisation and the applied field is reported in the literature [10] and exhibits a coercive field of approximately 0.6 T at 10 K, while at RT the coercive field is almost zero. Additionally a CMR of 80 % is achieved at 5 K in the presence of an applied field of 8 T [10]. In figure 1.1 the LCMO manganites show an interesting behaviour of both resistivity and magnetisation below the T_C at 210 K [10, 13, 14]. The resistivity is altering with the temperature and an increase is observed when the temperature is reduced

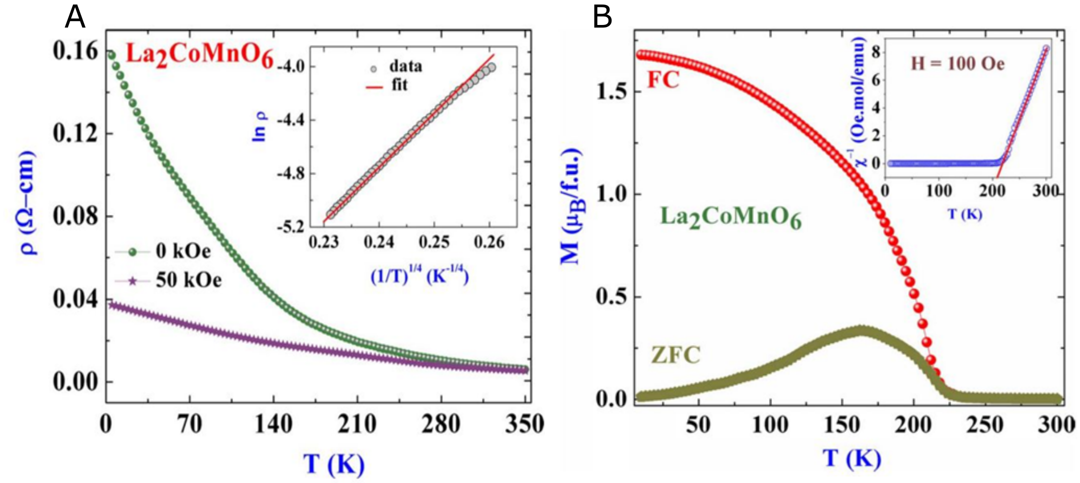

Figure 1.1: A) Electrical resistivity of La_2MnCoO_6 depending on temperature. The inset shows the fit to the variable range hopping model. B) ZFC and FC magnetisation of La_2MnCoO_6 in an applied field of 0.01 T under consideration of the temperature. [10]

below T_C. The temperature dependence of the resistivity (figure 1.1A) was observed inter alia by Yáñez-Vilar et al. [15] and Yang et al. [9]. If a strong magnetic field is applied than the resistance is nearly unchanged below T_C compared to the measured values at RT. Another side effect concerns the magnetisation, which is changing its behaviour below T_C (see figure 1.1B) when an external magnetic field is applied to the specimen (named field-cooled (FC)) or not (named zero-field-cooled (ZFC)) [10, 15]. The LCMO manganites were also investigated by density functional theory (DFT) calculations [16–18]. Yuan et al. [17] analysed the formation of bulk oxygen vacancies and refers that LCMO with antisite defects is a promising solid oxide fuel cell cathode material. Ullah et al. [16] characterised LCMO as ferromagnetic material with a small bandgap. The investigation of the electronic structure shows a dependence of LCMO as ferromagnetic insulator on Coulomb-assisted spin-orbit coupling as reported by Baidya and Saha-Dasgupta [18].

In this regard, the specific behaviours of the LCMO oxides under the influence of temperature and magnetic field are changing resistivity and magnetisation of the sample and make it worth to investigate the consequences of the CMR effect on EELS in TEM. The analysis of the structural, physical and chemical properties of the thin film manganites by means of TEM equipped with an electron energy loss spectrometer is a powerful tool and offers the possibility to investigate the specimen in microscopic scale. The main advantage compared to other techniques is the high spatial resolution, which offers the investigation of the CMR effect with respect to defects and strains. However, limiting factors are the inelastic delocalisation of the energy loss and the Čerenkov light excitation. Both effects are related to the beam energy of the probe electron and are more dominant at higher beam energies. Inelastic delocalisation is defined as the localisation distance between atom and probe electron. Stöger-Pollach [19] calculated the dependency of the inelastic delocalisation on the energy loss for different beam energies and exhibit a bisection of the delocalisation to 15 nm at 5 eV energy loss when the beam energy is decreased from 200 keV to 40 keV. In the case of the Čerenkov effect, only the high tension can be changed in order to minimise its impact, because the refractive index of the observed material can not be changed. Hence, the decrease of beam energy implies a reduction of inelastic delocalisation and prevents the Čerenkov loss excitations. A positive side effect of the reduction is that beam sensitive samples can be analysed without sustaining damage. In addition, the zero loss peak (ZLP) tail of the spectrum is narrowed and results in an analytical improvement of the bandstructure determination, which is positive for the semiconductor and insulator analysis [19].

VEELS and EMCD were used for the investigation to obtain precise results concerning the alteration of resistivity and magnetisation above and below T_C. The combination of TEM and EELS can be employed to prove the conductivity and dielectric properties [20]. Fundamental properties as plasmon resonances, bandgaps and optical properties are probed in the VEELS spectrum [21], which covers approximately the first 50 eV of an energy loss spectrum. The advantage of VEELS apart from the wide spectral range (from 1 eV up to 50 eV) is the high spatial resolution compared to conventional optical methods, which are limited by the wavelength of light. Another benefit is the opportunity of angular dependent measurements with a momentum transfer being unequal zero. Low voltage TEM with respect to VEELS enables a direct bandgap determination due to the absence of relativistic energy losses [22]. The characterisation of the magnetisation with chemical sensitivity [23] and a high spatial resolution [24, 25] can be achieved by EMCD with a resolution of at least two nanometres. Nevertheless, the local determination of magnetic moments with regard to EMCD has to consider all possible aspects of magnetism and oxidation [26].

The approach to combine these two techniques, VEELS and EMCD, has been demonstrated by Wallisch et al. [27]. The consequences of the CMR effect on the bandstructure and the element specific magnetisation were detected by using EELS.

1.2 Objectives

The novel approach has a huge potential as a new analytical method in the field of nanotechnology for detecting changes of magnetisation and resistivity at different temperatures on thin films. The combination of VEELS and EMCD obtains precise results by determining the consequences of CMR effect on the nanometre scale. The following milestones of this work are:

- Observation of the microstructure concerning the behaviour of defects and strains when changing the layer thickness.
- VEELS measurements to observe a bandgap alteration of double perovskite manganites by changing the external magnetic field and the temperature.
- EMCD investigations to proof the magnetic behaviour of double perovskite manganites by changing the temperature.
- Optical measurements by ellipsometry to compare them with the VEELS results.
- Numerical simulations based on the fully relativistic Kröger equation to analyse influence of Čerenkov losses on double perovskite manganites.
- Application of a monochromated TEM for the VEELS investigations to reduce the spread of the ZLP and improve the energy resolution of the low loss spectra.
- Numerical simulations of the electronic structure of double perovskite manganites by using the WIEN2k code.

Chapter 2

Theoretical Background

In this chapter a general introduction of fundamental requirements for inelastic interaction of electrons is given to interested readers. The theoretical tour starts with the description of the CMR effect and its consequences on resistivity and magnetisation followed by the inelastic scattering theory with some intermediate stops in quantum mechanics and electrodynamics. The journey ends with the correlation of electronic and dielectric properties.

2.1 Colossal Magnetoresistance Effect

The great interest in the CMR effect relies on the dramatic alteration of the resistivity in the presence of a magnetic field. In particular, manganese oxide compounds exhibit an extremely large negative magnetoresistance below $\mathrm{T_C}$ when applying a magnetic field. Additionally, a metal-insulator transition can be observed, when the magnetic field is changed. The phenomena, which describes this alteration of resistivity and magnetisation, is known as the CMR effect. The application of a magnetic field reduces the disorder in the spin system and thus, ferromagnetic state can be achieved and the electric resistivity is strongly degraded.

The CMR in mixed valence manganites was discovered in the 1950s by Jonker and Van Santen [1] in Philips Research Laboratories. The experimental observations of $\mathrm{La_{0.8}Sr_{0.2}MnO_3}$ (LSMO) and $\mathrm{Nd_{0.5}Pb_{0.5}MnO_3}$ by Volger [3] and Kusters et al. [4] exhibit the classical understanding of the CMR effect as shown in figure 2.1. The temperature variation from low temperature to RT shows a change of the resistivity, the saturation magnetisation and an increase of the negative magnetoresistance by applying a field of 0.3 T. The increase of the external magnetic field leads to a rapid decrease in resistivity as shown in figure 2.1D. Structural, electronic and magnetic properties of manganites are closely intertwined with the CMR effect. Slight changes in the composition or through the synthesis affect the properties of the material. On this account, the origins of the CMR effect are analysed and discussed in this section.

A requirement behind this effect is the appropriate crystal structure. Only materials with a perovskite structure exhibit the CMR behaviour. The ideal perovskite possesses a cubic close packed ABX_3 structure [28–30], which is named after the mineral perovskite, $CaTiO_3$. The ABO_3 compound of manganites crystallises in modifications of the perovskite structure. Many perovskites do not possess the ideal cubic structure, however, displacements and rotations can also lead to important physical properties.

A crucial characteristic of the perovskite structure is the manganese ion surrounded by the oxygen octahedron. The unit cell of the perovskite structure is given in figure 2.2 and consist of two cations, A and B, and three oxygen anions. The A ions are placed at the corners of the unit cell, the B ion is in the centre and the oxygen ions are situated at the centres of the faces. In order to achieve the desired material properties, the ABO_3 compound is doped at the A and the B site, respectively. As a consequence, displacements and strain arise during the synthesis. The lattice site A denotes a large ion like La^{3+}, which can be doped by alkaline earth ions, e.g. Sr^{2+}, whereupon an A' position is added to the compound. In view of B site ordering, the $A_2BB'O_6$ notation of the composition is used, which is called double perovskite. The stability of the perovskite structure is described by the Goldschmidt tolerance factor t [31]:

$$t = \frac{1}{\sqrt{2}} \frac{r_A + r_O}{r_B + r_O} \tag{2.1}$$

where r_A, r_B, r_O are respectively the radii of the ions A, B and oxygen. The Goldschmidt tolerance factor in equation 2.1 is a measure of distortion and the stability of the perovskite structure is given in the range from $0.89 < t < 1.02$ [29]. In the case of an ideal cubic perovskite the Goldschmidt tolerance factor is equal one and the manganese-oxygen-manganese bond angle has 180° as shown in the top right side in figure 2.2. When $t < 1$ then distortions are present and thus the bond angle is decreasing. The cubic structure transforms to rhombohedral ($0.96 < t < 1$) and

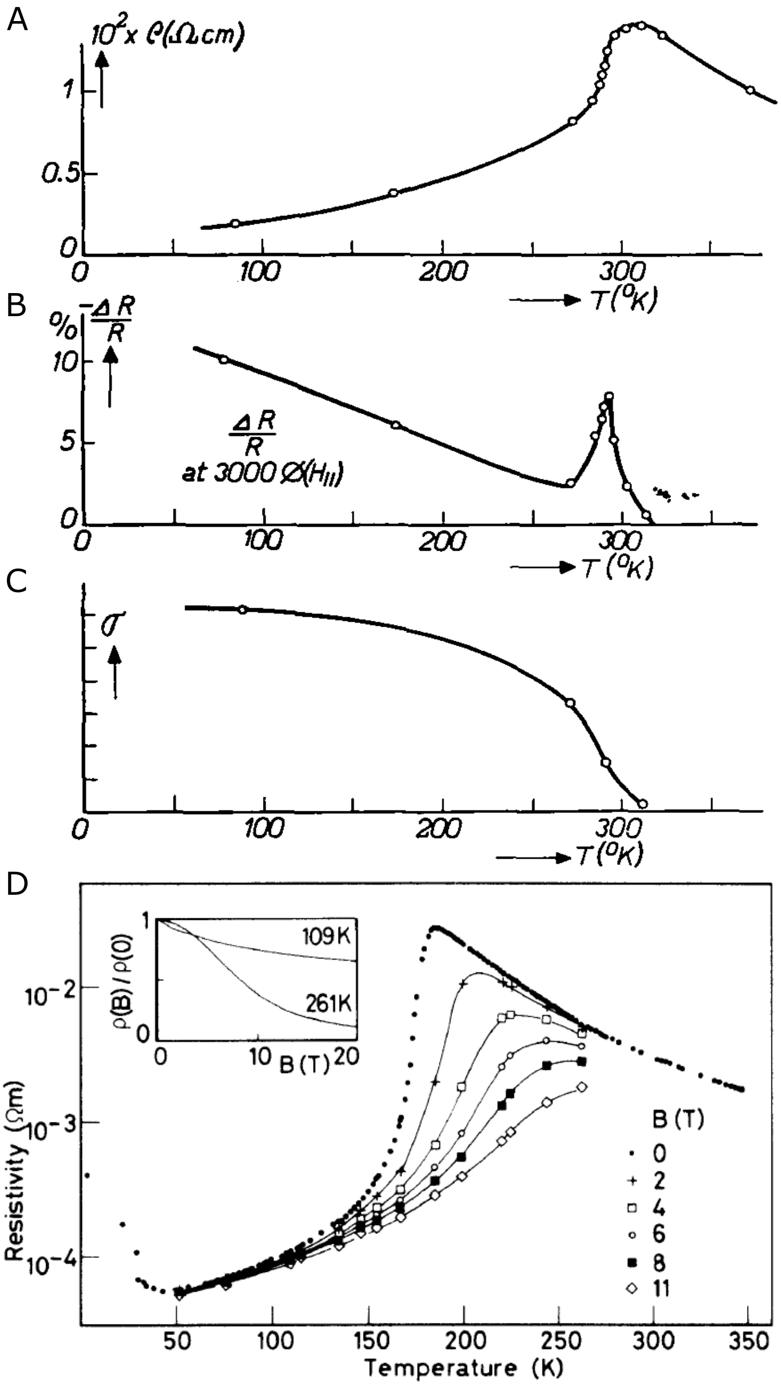

Figure 2.1: Temperature dependent characteristics of LSMO according to Volger [3]: A) resistivity, B) magnetoresistance by applying a magnetic field of 0.3 T and C) saturation magnetisation. D) Electric resistivity of $Nd_{0.5}Pb_{0.5}MnO_3$ as function of various external magnetic fields according to Kusters et al. [4]. The inset shows the magnetoresistance above and below T_C.

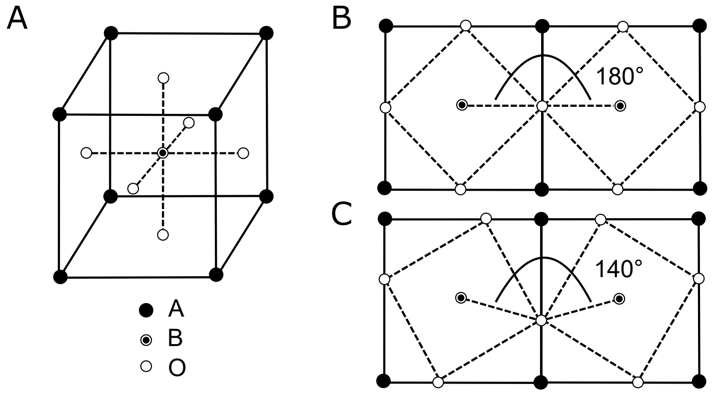

Figure 2.2: A) The schematic unit cell of the perovskite structure. B) Undistorted and C) distorted structure after tilting of the oxygen octahedron showing the change of the bond angle.

then to orthorhombic ($t < 0.96$), which is nearly monoclinic [30]. The Goldschmidt tolerance factor was calculated and achieves a value of 0.905 for $La_{0.8}Sr_{0.2}MnO_3$ and for La_2CoMnO_6 0.913. Hence, the crystal structure of both compounds tends to be monoclinic.

Beside the crystal structure, a view on the electronic structure has to be done for a deeper insight in the mechanisms of the CMR effect. Nowadays, a huge variety of $A^{3+}_{1-x}A'^{2+}_{x}(Mn^{3+}_{1-y}Mn^{4+}_{y})O^{2-}_{3}$ or $A^{3+}_{2}(Mn^{3+}_{1-y}Mn^{4+}_{y})_{1-x}B'^{3+}_{x}O^{2-}_{3}$ doped manganese oxides compounds was investigated. Without changing the carrier concentration x, a distortion of the lattice can be achieved by the substitution of ion A through rare earth ions or ion A' through alkaline earth ions. As a consequence, the Mn-O-Mn bond angle is changing as well as magnetic and electronic properties, which is reported by Hwang et al. [32]. A decrease of the bond angle is obtained by increasing distortion of the oxygen octahedron and smaller bond angles leads to a reduction of the overlap between the electron orbitals, which affects the electron hopping and in particular the magnetic exchange interaction.

The electronic structure of manganites is based on the oxygen octahedron and the corresponding Mn-O-Mn bond angle. The ground state of manganese is orbital degenerated and possesses five degenerated 3d orbitals into low energy three fold degenerated t_{2g}- and high energy two fold degenerated e_g-level as shown in figure 2.3. The crystal field is ordered due to the Coulomb rejection of the O^{2-} ions in the oxygen octahedron. Three electrons of the Mn^{3+} are filling the t_{2g}-orbitals and the

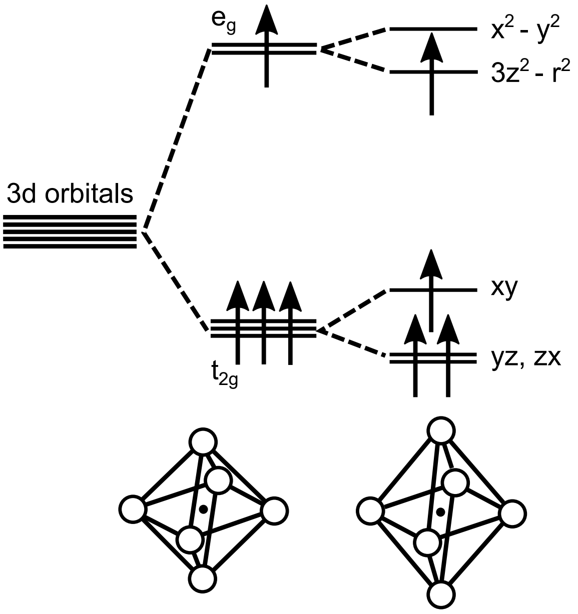

Figure 2.3: Crystal field splitting into lower-lying t_{2g} and high-lying e_g states; due to Jahn-Teller distortion the degeneracy of the d orbital is lifted. Adapted from Tokura and Tomioka [30]

fourth electron occupies one of both e_g orbitals. The resulting orbital degeneration makes the crystal lattice unstable and the system tries to lower the symmetry by means of distortions, which reverse this degeneration. The reason for this behaviour is the Jahn-Teller effect [33]. Preferably, this effect happens in transition metal oxides, e.g. Mn^{3+} or Cu^{2+}. Additionally the hybridisation of Mn 3d and O 2d orbitals leads to the splitting of the d- and p-levels, which affects the electronic structure.

The doping of $LaMnO_3$ with alkaline earth metals or transition metals influences the structure and enables a mixed valence of Mnions (Mn^{3+}, Mn^{4+}). The Mn^{4+} ion possesses three electrons and all of them occupy the t_{2g}-states. Thus, the distortion of the lattice due to the Jahn-Teller effect is decreasing with an increase of Mn^{4+} ions [30].

On the basis of the mentioned crystal and electronic structure two transport phenomena arise, which can describe the change of resistivity and magnetisation. The orbital overlap of the oxygen p orbitals and the manganese d orbitals enables a super exchange. The super exchange is an indirect magnetic interaction of two magnetic cations through a diamagnetic anion [34]. It is a strong antiferromagnetic coupling, which describes the interaction of a 3d electron of the Mn ions with p electron of the O ion. Due to the Pauli exclusion principle only antiparallel ordering of the spins is energetically favoured. The hopping of the electrons leads to antiferromagnetic Heisenberg exchange interaction [35].

Another indirect exchange interaction is the double exchange, which describes the ferromagnetism of perovskite manganite systems coupled by the electrical conductivity [36–38]. The interaction of magnetic ions in two different valence states exhibits interesting electronic and magnetic properties like the increase of the conductivity accompanied by the change of the former non-magnetic sample to ferromagnetic. The e_g-electron of a Mn^{3+} ion is moving to the filled p orbital of the oxygen and simultaneously an electron with the same spin is hopping from the oxygen orbital to an unoccupied e_g-state of a Mn^{4+} ion. The double exchange mechanism makes the CMR effect roughly explainable, however, the resistivity behaviour of the manganites is not adequately clarified as reported by Millis et al. [39]. It was claimed that the modelling of the double exchange does not perfectly fit the experimental observations and as a possible solution, polarons are mentioned to cause this discrepancy.

On the lookout for the missing piece of the puzzle, the more recent literature is reporting that the missing link are phase separations, which lead to state transitions due to small perturbations. The involved phases are chemical and structural similar, while the electronic properties are different [40]. The description of these phase separations are analysed with the aid on percolation theory [41, 42], which deals with the formation of associated clusters. Becker et al. [43] was able to demonstrate a temperature dependent percolation transition on thin film manganites. A coexistence of different phases was documented by Jooss et al. [44] in a temperature range from 80 K to RT.

In the newest approaches polarons are the charge carriers [39, 45]. A polaron is an electron-distortion coupling and its agility influences the electrical conductivity. It is reported by Jaime et al. [46], that small polarons affect lattice distortions and magnetic characteristics, and at low temperature a small band of localised states arise. Neutron scattering investigations at low temperature discover the CMR effect caused by the structural and magnetic polarons, which show a transition from ferromagnetic-metallic to paramagnetic-insulator [47, 48].

The first model, which described the CMR effect with a reasonable approximation was the double exchange model [36–38]. It gives a simple characterisation of the processes below the surface. The spins of the observed material are oriented ferromagnetically by applying a magnetic field and enable a great conductivity. A variety of promising mechanisms and effects contributes to the description of the CMR effect, however, the complete solution is still lacking [40, 49].

2.2 Inelastic Electron Scattering

The scattering theory gives an insight in the interaction of two particles. It is a question of the definition concerning the target whether an interaction is elastic or inelastic. The classical description of inelastic scattering is based on the inner energy change of the scatterers. This subchapter covers the description of the inelastic interaction using quantum mechanic and electrodynamic considerations.

2.2.1 Quantum Mechanical Approach

The most important variable in the theoretical investigation and description of scattering (collision) processes is the cross section. It is directly linked to the experiment and defined as:

$$\frac{number\,of\,processes\,per\,time}{incident\,particle\,current\,density} \tag{2.2}$$

The cross section is proportional to the probability of the scattering process. In other words, the number of particles per unit time entering the detector within a solid angle Ω is given by $\Gamma = N \cdot d\Omega$ and the flux of particles in the incident beam is defined as the incident particle current density j_i. Hence, the scattering probability is given by the differential scattering cross section $\partial\sigma$:

$$\partial\sigma = \frac{\Gamma}{j_i} \tag{2.3}$$

The calculation of the inelastic cross section can be done by first order perturbation theory due to the small scattering potential compared to the conventional beam energy (200 keV) in TEM. A suitable approach for this endeavour is Fermi's golden rule, which is the relation of the transition rate Γ, the transition matrix element

M_{fi} and the density of the final state $\rho(E')$:

$$\Gamma = \frac{2\pi}{\hbar}|M_{fi}|^2 \cdot \rho(E') \tag{2.4}$$

where $\hbar$ is the reduced Planck constant. The transition matrix element is

$$M_{fi} = \langle\psi_f|H_{int}|\psi_i\rangle = \int \psi_f^* H_{int}\psi_i dV \tag{2.5}$$

where H_{int} is the interaction Hamiltonian operator and $\psi_{i,f}$ are the wave functions of initial and final states. The asterisk at ψ_f^* denotes the complex conjugated wave function of ψ_f. Considering equation 2.3, for the characterisation of the collisions the differential cross section is given by:

$$\frac{\partial\sigma}{\partial\Omega} = \sum_f \frac{2\pi k_f m}{\hbar^3 j_i} |\langle\psi_f|V|\psi_i\rangle|^2 \delta(E_i - E_f) \tag{2.6}$$

where m is the mass of the particle, k_f is the wave vector of the final state and V is the perturbation potential. The related quantum mechanical current density j_i according to [50] is

$$j_i = \frac{\hbar}{2m_i}(\psi_i^*\nabla\psi_i - \psi_i\nabla\psi_i^*) = \frac{\hbar k_i}{(2\pi)^3 m} \tag{2.7}$$

where ψ_i is the wave function of the initial state and k_i is the wave vector of the initial state. By combining (2.6) and (2.7)

$$\frac{\partial\sigma}{\partial\Omega} = (\frac{2\pi}{\hbar})^4 m^2 \sum_f \frac{k_f}{k_i} |\langle\psi_f|V|\psi_i\rangle|^2 \delta(E_i - E_f) \tag{2.8}$$

is obtained. On the basis of elastic scattering, the potential V in equation 2.8 is static. In the inelastic case the scatterer has to be treated as wave function and due to this issue a Coulomb potential is used as a perturbation potential V:

$$V = -\frac{Ne^2}{r} + \sum_{j=1}^{N} \frac{e^2}{|\vec{r} - \vec{r_j}|} \tag{2.9}$$

The first term of equation 2.9 describes the Coulomb attraction by the nucleus. The second term is the electron part at the potential of the scatterer and represents the repulsive electrostatic interaction between the fast incident electron and the atomic electrons. The nuclear part becomes zero due to the orthogonality of the initial and final wave functions. Hence, only collisions with atomic electrons contribute to the inelastic interaction. The mass of the incident electron and an atomic electron is comparable, which leads to an energy transfer in inelastic interactions. After short derivation and transformation of equations 2.8 and 2.9 according to [51, 52] the double differential inelastic cross section is obtained:

$$\begin{aligned}\frac{\partial^2\sigma}{\partial E\partial\Omega} &= \frac{m^2e^4(4\pi)^2}{(2\pi)^2\hbar^4q^4}\frac{k_f}{k_i}\sum_{\phi_f}\left|\langle\phi_f|\sum_{j=1}^{N}e^{i\vec{q}\vec{r}_j}|\phi_i\rangle\right|^2\cdot\delta(E_{\phi_i}-E_{\phi_f}+E)\\ &= \left[\frac{2me^2}{\hbar^2q^2}\right]^2\frac{k_f}{k_i}\cdot S(\vec{q},E)\end{aligned} \tag{2.10}$$

where $S(\vec{q},E)$ is the dynamic form factor (DFF) and with $E = E_{\phi_i} - E_{\phi_f}$ the energy loss is introduced. The inelastic differential cross section calculated with a Coulomb potential is proportional to $1/q^4$, which is equivalent to the Rutherford cross section $(1/\sin^4\frac{\theta}{2})$. The DFF is the inelastic contribution of equation 2.10, which is the square of absolute value of the transition matrix element (equation 2.4). This dimensionless factor is a correction of the Rutherford scattering cross section that intervenes when the atomic electrons are free. If Bloch waves are used instead of plane waves than the DFF becomes generalised to the mixed dynamic form factor (MDFF) [53].

2.2.2 Electrodynamical Approach

Inelastic interactions with valence or conduction electrons are differently treated compared to energy losses of inner shell electrons. The quantum mechanical approach provides a good description of the ionisation losses, which are single particle excitations in quantum theory. In contrast to the previous approach, energy loss of valence electrons can not be treated in an atomic picture, because their wave functions are modified by chemical bondings [51]. Additionally, the collective effect is not a negligible issue and the descriptive theory should consider the solid as a many-body system, which is the case for valence electrons.

Many-body excitations are better treated by a continuum theory as the Maxwell theory, which describes the interaction of a transmitted electron with the entire solid. The main idea is the usage of the dielectric function ϵ as response function to an electrostatic perturbation, e.g. a fast electron. The eigenmodes of the system and the matter interactions with external perturbations [51] are determined by ϵ. In the following equations, the most simple case for the electromagnetic response is discussed regarding a homogeneous, isotropic and non-magnetic material. The eigenmodes are easier connected to the energy loss spectrum due to the application of Maxwell equations in Fourier space. The response of the material due to an electric field is given by the polarisation $\vec{P}$, which is proportional to the dielectric susceptibility χ and the electric field $\vec{E}$:

$$\vec{P} = \chi \cdot \vec{E} \tag{2.11}$$

The dielectric function (permittivity) ϵ includes the properties of the material and shows the following relation to χ:

$$\epsilon = 1 + 4\pi\chi \tag{2.12}$$

The displacement field $\vec{D}$ is connected with the electric field $\vec{E}$ via ϵ:

$$\vec{D} = \epsilon\vec{E}(\vec{r}, t) \tag{2.13}$$

In addition to the relation with the $\vec{E}$ field, the $\vec{D}$ field is connected to the polarisation $\vec{P}$ via the permittivity. The equation 2.13 can be written as Fourier transform (FT):

$$\vec{D}(\vec{r}, t) = \epsilon \cdot \vec{E}(\vec{r}, t) \leftrightarrow \vec{D}(\vec{k}, \omega) = \epsilon(\vec{k}, \omega)\vec{E}(\vec{k}, \omega) \tag{2.14}$$

The system is also described by conductivity σ and the magnetic permeability μ:

$$\vec{j}(\vec{r}, t) = \sigma \cdot \vec{E}(\vec{r}, t) \leftrightarrow \vec{j}(\vec{k}, \omega) = \sigma(\vec{k}, \omega)\vec{E}(\vec{k}, \omega) \tag{2.15}$$

$$\vec{B}(\vec{r}, t) = \mu \cdot \vec{H}(\vec{r}, t) \leftrightarrow \vec{B}(\vec{k}, \omega) = \mu(\vec{k}, \omega)\vec{H}(\vec{k}, \omega) \tag{2.16}$$

where $\vec{j}$ is the current density, $\vec{B}$ is the magnetic field and $\vec{H}$ is the magnetised field.

Maxwell Equations

The Maxwell equations are formed in FT and use the electrostatic system of units ($\mu = \epsilon = 1$) for simplification. Consequently, the fields $\vec{D}$ and $\vec{E}$ have the same dimension and that leads to some simplifications, for example in the following section "Dielectric Function".

$$\nabla \vec{D} = 4\pi\rho_{ex} \leftrightarrow i(\vec{k}, \vec{D}) = 4\pi\rho_{ex} \tag{2.17}$$

$$\nabla \vec{B} = 0 \leftrightarrow i(\vec{k}, \vec{B}) = 0 \tag{2.18}$$

$$\nabla \times \vec{E} = -\frac{1}{c}\frac{\partial}{\partial t}\vec{B} \leftrightarrow i(\vec{k} \times \vec{E}) = \frac{i\omega}{c}\vec{B} \tag{2.19}$$

$$\nabla \times \vec{H} = \frac{4\pi}{c}\vec{j_{ex}} + \frac{1}{c}\frac{\partial}{\partial t}\vec{D} \leftrightarrow i(\vec{k} \times \vec{H}) = \frac{4\pi}{c}\vec{j_{ex}} - \frac{i\omega}{c}\vec{D} \tag{2.20}$$

The external current density $\vec{j_{ex}}$ and the external charge density ρ_{ex} are vanishing when solving the Maxwell equations (equations 2.17 - 2.20) in the source-free case. The first two Maxwell equations (equations 2.17 and 2.18) can be rewritten with respect to the vector potential $\vec{A}$:

$$\vec{B} = \nabla \times \vec{A} \leftrightarrow \vec{B} = i\vec{k} \times \vec{A} \tag{2.21}$$

and the scalar potential ϕ:

$$\vec{E} = -\frac{1}{c}\frac{\partial}{\partial t}\vec{A} - \nabla\phi \leftrightarrow \vec{E} = \frac{i\omega}{c}\vec{A} - i\vec{k}\phi \tag{2.22}$$

By inserting the equations 2.21 and 2.22 into the Maxwell equations 2.17 and 2.20 and using the Coulomb gauge $\nabla\vec{A} = 0$, the equations can be rewritten:

$$\nabla \times (\nabla \times \vec{A}) = \frac{\epsilon\mu}{c}\frac{\partial}{\partial t}(-\frac{1}{c}\frac{\partial \vec{A}}{\partial t} - \nabla\phi) \leftrightarrow i\vec{k} \times (i\vec{k} \times \vec{A}) = -\frac{i\omega}{c}\epsilon\mu(\frac{i\omega}{c}\vec{A} - i\vec{k}\phi) \tag{2.23}$$

$$\nabla[\epsilon(-\frac{1}{c}\frac{\partial \vec{A}}{\partial t} - \nabla\phi)] = 0 \leftrightarrow -i\vec{k}\epsilon\mu(\frac{i\omega}{c}\vec{A} - i\vec{k}\phi) = 0 \tag{2.24}$$

Considering the Coulomb gauge and the cross product rule $\vec{a} \times (\vec{b} \times \vec{c}) = \vec{b}(\vec{a}\vec{c}) - \vec{c}(\vec{a}\vec{b})$ the following equations can be obtained:

$$\nabla^2 \vec{A} - \frac{\epsilon\mu}{c^2}\frac{\partial^2}{\partial t^2}\vec{A} - \frac{\epsilon}{c}\frac{\partial}{\partial t}\nabla\phi = 0 \leftrightarrow \vec{k}^2\vec{A} - \frac{\epsilon\mu\omega}{c^2}\vec{A} + \frac{\epsilon\mu\vec{k}}{c}\phi = 0 \tag{2.25}$$

$$\epsilon\nabla^2\phi = 0 \leftrightarrow \epsilon\vec{k}^2\phi = 0 \tag{2.26}$$

From equation 2.26 ϕ is

$$\phi = const \leftrightarrow \phi = const \cdot \delta^3(\vec{k}). \tag{2.27}$$

By inserting equation 2.27 into equation 2.25, the wave equation is achieved:

$$\Delta\vec{A} - \frac{\epsilon\mu}{c^2}\frac{\partial^2}{\partial t^2}\vec{A} = 0 \leftrightarrow (\vec{k}^2 - \frac{\epsilon\mu\omega^2}{c^2})\vec{A} = 0 \tag{2.28}$$

The immediate description of the FT (equation 2.28) through the derivation of the wave equation leads to the frequency dispersion law:

$$\frac{\epsilon\mu}{c^2}\omega^2 = \vec{k}^2 \tag{2.29}$$

The wave character can be analysed by means of the Maxwell equations and allows the following conclusions. From equation 2.22 follows that $\vec{E} \parallel \vec{A}$ and due to the Coulomb gauge $\vec{k} \perp \vec{A}$ is obtained. Consequently, the electric field $\vec{E}$ is normal to the wave vector $\vec{k}$ ($\vec{E} \perp \vec{k}$) and equation 2.21 leads to $\vec{B} \perp \vec{E}$ and $\vec{B} \perp \vec{k}$. The electric and the magnetic fields are normal to the wave vector and thus, only transversal electromagnetic waves are assumed to be inside the material. However, from equation 2.26 follows that either ϵ or ϕ is zero to obtain a solution. There might be cases (k_0, ω_0) where ϵ is vanished and ϕ is arbitrary. Hence, equation 2.25 leads to $\vec{A}(k_0, \omega_0) = 0$ and it can be conclude that $\vec{E} \parallel \vec{k}$. To sum up, longitudinal and transversal electromagnetic waves exist in the medium.

Dielectric Function

The relation between ϵ and σ is described by connecting the fourth Maxwell equation (equation 2.20) and the Ohm's law (equation 2.31). Only the external current density $\vec{j_{ex}}$ without the polarisation current density $\vec{j_{pol}}$ is included in equation 2.20.

Hence, this equation can be rewritten:

$$i(\vec{k} \times \vec{H}) = \frac{4\pi}{c}(\vec{j_{ex}} + \vec{j_{pol}}) - \frac{i\omega}{c}\vec{E} = \frac{4\pi}{c}\vec{j_{ex}} - \frac{i\omega\epsilon}{c}\vec{E} \tag{2.30}$$

The relation between ϵ and $\vec{E}$ is given by means of the Ohm's law

$$\vec{j_{pol}} = \sigma\vec{E}. \tag{2.31}$$

By inserting $\vec{j_{pol}}$ in equation 2.30 and comparing the coefficients of $\vec{E}$

$$\epsilon = 1 + \frac{4\pi i\sigma}{\omega} \tag{2.32}$$

is obtained. For non-magnetic materials the system is completely described by ϵ. The conductivity is necessary for metals to analyse the response of the material due to $\sigma(\vec{k}, 0) \neq 0$ and $\epsilon(\vec{k}, 0) \to \infty$. Nevertheless, ϵ describes the response function of the system due to electromagnetic perturbations excluding the $\omega = 0$ case. The well known relation from optics concerning the complex dielectric function $\epsilon = \Re(\epsilon) + i\Im(\epsilon)$ and the complex refractive index $n_c = n + i\kappa$ is described by

$$n^2 - \kappa^2 = \Re(\epsilon) \quad 2n\kappa = \Im(\epsilon) \tag{2.33}$$

Thus, it appears that the electrical and optical properties of a material are determined by the dielectric function ϵ.

Drude Model

The Drude model is a good approximation for the dielectric behaviour of free electrons like in metals. On the basis of this model the important characteristic of the permittivity is shown by an ideal metal without any resonant frequencies. This implies that the conduction electrons are moving free. For conduction electrons the equation of motion in a longitudinal field $\vec{E}$ is

$$m\frac{\partial\vec{v}}{\partial t} + m\frac{\vec{v}}{\tau} = e\vec{E} \leftrightarrow -i\omega m\vec{v} + \frac{m}{\tau}\vec{v} = e\vec{E} \tag{2.34}$$

where m is the mass of an electron, e is its charge and $\vec{v}$ is its velocity. The relaxation time is defined by τ. The current $\vec{j}$ is proportional to the charge density ρ_0 in the equilibrium state and the corresponding number of electrons n:

$$\vec{j} = \rho_0 \vec{v} = ne\vec{V} \tag{2.35}$$

The equation of motion (equation 2.34) is modified by multiplying $\rho_0/m = ne/m$:

$$\frac{\partial \vec{j}}{\partial t} + \frac{\vec{j}}{\tau} = \frac{ne^2}{m}\vec{E} \leftrightarrow \vec{j}(\frac{1}{\tau} - i\omega) = \frac{ne^2}{m}\vec{E} \tag{2.36}$$

In this case, the current is the polarisation current $\vec{j_p}$, which is caused by an external field $\vec{E}$. The relation between $\vec{j_p}$ and the dipol moment density $\vec{P} = ne(\vec{r}(t) - \vec{r_0})$, where $\vec{r_0}$ is the equilibrium position of an electron, is given in equation 2.35:

$$\vec{j} = ne\frac{\partial \vec{r}}{\partial t} = \frac{\partial}{\partial t}\vec{P} \leftrightarrow -i\omega\vec{P} \tag{2.37}$$

The combination of the equations 2.12 and 2.13 with 2.36 and 2.37 gives:

$$\epsilon = 1 + \frac{4\pi|\vec{P}|}{|\vec{E}|} = 1 + \frac{4\pi ne^2}{m}\frac{1}{-i\omega(\frac{1}{\tau} - i\omega)} \tag{2.38}$$

Since equation 2.13 is space-independent, the resulting ϵ in equation 2.38 is independent of $\vec{k}$. The plasma frequency is defined as:

$$\omega_p^2 = \frac{4\pi ne^2}{m} \tag{2.39}$$

Inserting the plasma frequency into equation 2.38 yields both the real part $\Re$ and the imaginary part $\Im$ of the complex dielectric function known as "Drude expressions" for a metal [51]:

$$\Re(\epsilon) = \epsilon_1 = 1 - \frac{\omega_p^2}{\omega^2 + \frac{1}{\tau^2}} \tag{2.40}$$

$$\Im(\epsilon) = \epsilon_2 = \frac{1}{\omega\tau}\frac{\omega_p^2}{\omega^2 + \frac{1}{\tau^2}} \tag{2.41}$$

Drude-Lorentz Model

The classical Drude model describes well many conducting media, however, insulating and semiconducting materials are inadequate depicted. The Drude-Lorentz model differs due to the point of view that the charges of an insulator are not moving freely and hence, it can be assumed that an insulator is an ensemble of charged particles on fixed positions. The charges oscillate at their rest position, so that oscillations occur.

In this case, the equation of motion (equation 2.34) is extended with harmonic restoring force $-\omega_0^2 mx$ to describe semiconductors and insulators as well. Hence, the real and imaginary part of the dielectric function are rewritten:

$$\epsilon_1 = 1 + \omega_p^2 \cdot \frac{(\omega_0^2 - \omega^2)}{(\omega_0^2 - \omega^2)^2 + (\frac{\omega}{\tau})^2} \tag{2.42}$$

$$\epsilon_2 = \omega_p^2 \cdot \frac{\omega}{(\omega_0^2 - \omega^2)^2 + (\frac{\omega}{\tau})^2} \tag{2.43}$$

The complex dielectric function is dependent on the frequency. If the resonant frequency ω_0 is zero than the Drude relation is obtained and the previous equations (equations 2.40 and 2.41) are valid.

Kramers-Kronig Analysis

The determination of dielectric properties is achieved by using the Kramers-Kronig analysis (KKA). According to Stöger-Pollach [21] the analysis consists of five steps:

- Removal of the ZLP
- Multiple scattering deconvolution
- Angular correction
- Normalisation
- Data treatment by use of the Kramers-Kronig relation (KKR)

For the theoretical description of the scattering process within the KKA, the double differential inelastic cross section (equation 2.10) is simplified and the resulting single volume scattering distribution (SSD) is

$$SSD(\omega) = \frac{2\pi e^2 I_0}{\pi^2 \hbar^2 v^2} \cdot d \cdot \Im\left[-\frac{1}{\epsilon(\omega)}\right] \cdot ln\left[1 + \left(\frac{\beta}{\theta_E}\right)^2\right] \tag{2.44}$$

where I_0 is the intensity of electron beam, d is the sample thickness, θ_E is the characteristic scattering angle and β the collection semi-angle. The k_f/k_i term of equation 2.10 is given by the logarithmic term, which includes the limit of acceptance angle β and is called the angular correction part. The first part in equation 2.44 including the thickness is known as the normalisation factor N. The $\Im(-1/\epsilon(\omega))$ term is the required loss function. A detailed description of KKA is given in Stöger-Pollach [21] and Egerton [52].

When the normalised loss function is known, then the Kramer-Kronig relation

$$\Re\left(\frac{1}{\epsilon(\omega)}\right) = 1 - P\frac{2}{\pi}\int_0^\infty \Im\left(-\frac{1}{\epsilon(\omega')}\right)\frac{d\omega'}{\omega'-\omega} \tag{2.45}$$

can be used to determine the dielectric function

$$\epsilon = \epsilon_1 + i\epsilon_2 = \frac{\Re\left(\frac{1}{\epsilon(\omega)}\right) - i\Im\left(\frac{1}{\epsilon(\omega)}\right)}{\left[\Re\left(\frac{1}{\epsilon(\omega)}\right)\right]^2 + \left[\Im\left(\frac{1}{\epsilon(\omega)}\right)\right]^2} \tag{2.46}$$

where P is the Cauchy principle part of the integral. The optical properties are now easily calculable:

$$\begin{aligned}
\text{complex refractive index } n_c(\omega) &= \sqrt{\epsilon} = n + i\kappa \\
\text{refractive index } n &= \sqrt{\frac{1}{2}\left(\epsilon_1 + \sqrt{\epsilon_1^2 + \epsilon_2^2}\right)} \\
\text{extinction coefficient } \kappa &= \sqrt{\frac{1}{2}\left(\sqrt{\epsilon_1^2 + \epsilon_2^2}\right) - \epsilon_1} \\
\text{absorption coefficient } \mu(\omega) &= \frac{2\pi}{c}\kappa \\
\text{reflection coefficient } R(\omega) &= \frac{(n-1)^2 + \kappa^2}{(n+1)^2 + \kappa^2} \\
\text{number of effective electrons } n_{eff}(\omega) &= \frac{m_e}{2\pi^2 e^2 n}\int_0^\infty \Im\left(-\frac{1}{\epsilon(\omega')}\right)\omega' \cdot d\omega'
\end{aligned} \tag{2.47}$$

2.2.3 Kröger Theory

The Kröger theory describes the differential energy loss probability of fast electrons passing through a dielectric thin film.In particular this derivation considers volume and surface losses, transition radiation and retardation effects.

In 1957 Ritchie [54] proposed to determine the energy loss probability of an fast electron scattering through a thin film by semiclassical calculations. These calculations correspond to some experiments such as in the case of Creuzburg [55] and Daniels [56]. However, the consequences of the retardation effects were neglected. Materials with a high dielectric constant and thick layers show an influence [57, 58] and can not disregarded. The inclusion of retardation in the theoretical description was succeeded by Kröger [59, 60]. Kröger [60] presented in his work the description of the differential energy loss probability of fast electrons, which pass through a dielectric thin film. The analysed thin film in figure 2.4 has a dielectric constant $\epsilon(\omega)$ and a thickness $2a$, and both surfaces are covered by a dielectric medium $\epsilon_0(\omega)$. The fast electron is a point charge $-e$, which penetrates the thin film at an angle α. After a detailed derivation according to [59, 60] the differential energy loss is given by

$$
\begin{aligned}
\frac{\partial^3 P(\vec{k}_\perp,\omega)}{\partial \Delta E \partial^2 \Omega} =& \frac{p_0^2}{\hbar^2}\cdot\frac{e^2}{\pi^2\hbar^2 v^2\cos\alpha}\Im\left[\frac{1-\epsilon\beta^2}{\epsilon\phi^2}\cdot 2a\right. \\
& - 2\cdot\frac{(\epsilon-\epsilon_0)^2}{\phi_0^4\phi^4}\left\{\left(\frac{\sin^2(b)}{L^+}+\frac{\cos^2(b)}{L^-}\right)\cdot\frac{B^2}{\epsilon\epsilon_0}\right. \\
& - \left(\frac{\cos^2(b)\tanh(\lambda a)}{L^+}+\frac{\sin^2(b)\coth(\lambda a)}{L^-}\right)\cdot A^2\lambda\lambda_0 \\
& + \left(\frac{1}{L^+}-\frac{1}{L^-}\right)\cdot\frac{\lambda_0}{\epsilon_0}\cdot A\cdot B\sin(2b) \\
& + \left(\frac{\omega}{v}\right)^4\beta^6\sin^2(\alpha)\sin^2(\phi)\left[\left(\frac{\kappa}{v_x}\right)^2\left(\frac{\sin^2(b)}{M^+}+\frac{\cos^2(b)}{M^-}\right)\right. \\
& - \lambda\lambda_0\left(\frac{\cos^2(b)\tanh(\lambda a)}{M^+}+\frac{\sin^2(b)\coth(\lambda a)}{M^-}\right) \\
& \left.\left.\left. -\lambda_0\frac{\kappa}{v_x}\sin(2b)\left(\frac{1}{M^+}-\frac{1}{M^-}\right)\right]\right\}\right]
\end{aligned}
\tag{2.48}
$$

where p_0 is the momentum of the incoming electron and the corresponding abbreviations are listed in equation 2.49. In equation 2.48 the first term is known as the volume part, the remaining terms are called surface part. In the case of thick samples the surface losses are infinitesimally small and can be neglected as known from [54, 61]. The last three lines of the Kröger equation (equation 2.48) can be neglected when the incidence of the probed electron is normal ($\alpha = 0$) to the surface. This approximation is used in several theoretical discussions due to simplification of the

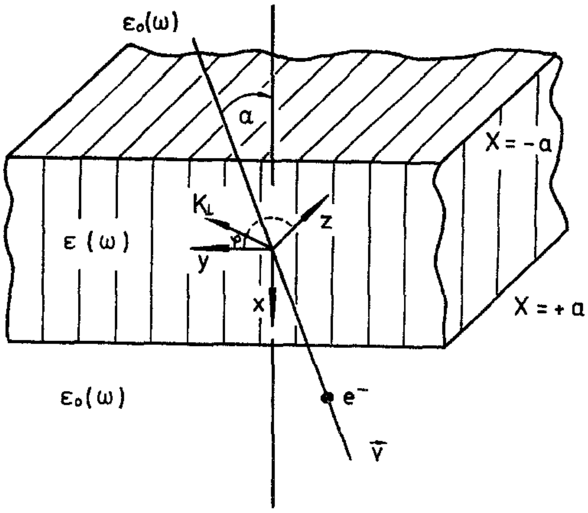

Figure 2.4: Overview of the thin film geometry according to Kröger [60].

investigated problem as known from [21, 52, 62, 63].

$$
\begin{aligned}
&\beta = \frac{v}{c}, \quad \vec{k}_\perp = (0, k_y, k_z), \quad k_\perp = \sqrt{k_y^2 + k_z^2} \\
&\cos\phi = \frac{k_y}{k_\perp}, \quad \lambda = \sqrt{k_\perp^2 - \frac{\epsilon\omega^2}{c^2}}, \quad \lambda_0 = \sqrt{k_\perp^2 - \frac{\epsilon_0\omega^2}{c^2}} \\
&\kappa = \omega + k_y v_y, \quad b = \frac{\kappa a}{v_x} \\
&L^+ = \lambda_0\epsilon + \lambda\epsilon_0 \tanh(\lambda a), \quad L^- = \lambda_0\epsilon + \lambda\epsilon_0 \coth(\lambda a) \\
&M^+ = \lambda_0 + \lambda \tanh(\lambda a), \quad M^- = \lambda_0 + \lambda \coth(\lambda a) \\
&\phi^2 = \left(k_\perp^2 + \frac{\kappa^2}{v_x^2}\right) - \frac{\epsilon\omega^2}{c^2}, \quad \phi_0^2 = \left(k_\perp^2 + \frac{\kappa^2}{v_x^2}\right) - \frac{\epsilon_0\omega^2}{c^2} \\
&\phi_{01}^2 = \left(k_\perp^2 + \frac{\kappa^2}{v_x^2}\right) - (\epsilon + \epsilon_0)\frac{\omega^2}{c^2} \\
&A = \left(k_\perp - \frac{\kappa}{v_x}\tan(\alpha)\cos(\phi)\right) \cdot \frac{\omega}{v} \cdot \beta^2 \cos(\alpha) \\
&B = k_\perp \phi_{01}^2 + \epsilon\epsilon_0\beta^4 \sin(\alpha)\cos(\phi) \cdot \left(\frac{\omega}{v}\right)^3
\end{aligned}
\tag{2.49}
$$

The Kröger equation 2.48 permits a review of the experimental data. The calculated relativistic energy loss probability can be set in relation to the measured EELS spectrum and offers an additional perspective. The initial data for the relativistic calculations are the measured dielectric properties of thin films by an ellipsometer as described later on in section 5.3.

2.3 Density Functional Theory

The microscopic comprehension of solids concerns the behaviour of electrons inside a periodic potential of a crystal. A solid consist of heavy, positively charged nuclei surrounded by light, negatively charged electrons. The formal description of this electromagnetically interacting particles leads to a many-body problem with a many-particle Hamiltonian $\hat{H}$ [64]:

$$\begin{aligned}\hat{H} = &-\frac{\hbar^2}{2}\left(\sum_i \frac{\nabla^2_{\vec{R}_i}}{M_i} + \sum_i \frac{\nabla^2_{\vec{r}_i}}{m_e}\right) \\ &- \frac{1}{4\pi\epsilon_0}\left(\sum_{i,j}\frac{e^2 Z_i}{|\vec{R}_i - \vec{r}_j|} - \frac{1}{2}\sum_{i\neq j}\frac{e^2}{|\vec{r}_i - \vec{r}_j|} - \frac{1}{2}\sum_{i\neq j}\frac{e^2 Z_i Z_j}{|\vec{R}_i - \vec{R}_j|}\right)\end{aligned} \tag{2.50}$$

where M_i is the mass of the nucleus at $\vec{R}_i$, m_e is the mass of the electrons at $\vec{r}_i$, e is the elementary charge and $Z_{i,j}$ are the atomic numbers of the nuclei. Equation 2.50 consists of a kinetic energy operator for the nuclei (first term), a kinetic energy operator for the electrons (second term) and the Coulomb interaction (other terms). The last three terms describe the electrons-nuclei interaction, electrons-electrons interaction and nuclei-nuclei interaction.

The basic approximation is the separation into atomic and electron movement. The movement of the heavy nuclei are much slower compared to the lighter electrons and hence, the nuclei can be seen as frozen. The independent treatment of atomic and electron movement is known as adiabatic or Born-Oppenheimer approximations. The consequences of this approximation are the vanishing of the first and the last term of equation 2.50. The nuclei are not moving and hence the kinetic energy is zero and the last term is only a constant. The resulting equation is

$$\hat{H} = \hat{T} + \hat{V}_{ext} + \hat{V} \tag{2.51}$$

where $\hat{T}$ is the kinetic energy of the electron gas, $\hat{V}_{ext}$ is the Coulomb potential between the electrons and the nuclei and $\hat{V}$ is the potential energy of the electron-

electron interactions. The observation of inhomogeneous systems leads to theories considering the energy of the many-electron problem as a functional of the local modified density, which is the basis of the local density functional approximation.

DFT can be attributed to the Hohenberg-Kohn-Sham theorem [65, 66]:

- The many-particle ground state E_0 is a unique functional of the density $n(\vec{r})$, $E_0 = E[n(\vec{r})]$.
- The unique functional $E[n(\vec{r})]$ has its minimum for the ground-state density corresponding to an external potential V_{ext}.

The first theorem shows the importance of the density. The second theorem explains that the functional is universal and can be used for any many-particle problem. Assuming that another potential V' with another ground state ϕ' leads to the same density $n_0(\vec{r})$:

$$E_0' = \langle \phi' | H' | \phi' \rangle < \langle \phi | H | \phi \rangle = \langle \phi | H + V' - V | \phi \rangle \tag{2.52}$$

so that

$$E_0' < E_0 + \int n_0(\vec{r})[V'(\vec{r}) - V(\vec{r})] d^3r \tag{2.53}$$

and by interchanging the primed and unprimed items:

$$E_0 < E_0' + \int n_0'(\vec{r})[V(\vec{r}) - V'(\vec{r})] d^3r. \tag{2.54}$$

An inconsistency is obtained by the addition of equation 2.53 and 2.54:

$$E_0 + E_0' < E_0 + E_0'. \tag{2.55}$$

Consequently, $n_0(\vec{r})$ and $n_0'(\vec{r})$ are not equal and the potential $V(\vec{r})$ is an unique functional of $n_0(\vec{r})$. If the particle density is known than the energy, the wave functions and the expectation values of any observable can be calculated.

Under consideration of the second theorem, the ground-state total functional $H[n(\vec{r})] = E[n(\vec{r})]$ is

$$\begin{aligned} E[n(\vec{r})] &= \langle \Phi | T + V | \Phi \rangle + \int n(\vec{r}) V_{ext}(\vec{r}) d^3r \\ &= F[n(\vec{r})] + \int n(\vec{r}) V_{ext}(\vec{r}) d^3r. \end{aligned} \tag{2.56}$$

Due to the variational principle of quantum mechanics

$$E[n'(\vec{r})] > E[n_0(\vec{r})] = E_0 = min\{E[n(\vec{r})]\} \tag{2.57}$$

with the variational condition

$$\frac{\partial E[n(\vec{r})]}{\partial n(\vec{r})}|_{n(\vec{r})=n_0(\vec{r})} = 0. \tag{2.58}$$

The ground-state energy in the local-density approximation can be written as:

$$E_{KS}[n(\vec{r})] = \int\int n(\vec{r})V_{ext}(\vec{r})d^3r + \frac{e^2}{2}\int\int \frac{n(\vec{r})n(\vec{r'})}{|\vec{r}-\vec{r'}|}d^3rd^3r' + G[n(\vec{r})] \tag{2.59}$$

on the basis of the Hohenberg-Kohn-Sham theorem. The functional $G[n(\vec{r})]$ in equation 2.59 consists of the kinetic energy functional and the exchange-correlation energy functional:

$$G[n(\vec{r})] = T[n(\vec{r})] + E_{xc}[n(\vec{r})] \tag{2.60}$$

The density for a single-particle wave functions is given by

$$n(\vec{r}) = \sum_i |\varphi_i(\vec{r})|^2. \tag{2.61}$$

The functional derivative according to the density is done by a variation of the orbitals $\varphi_i(\vec{r})$:

$$\left\{-\frac{\hbar^2}{2m}\nabla^2 + V_{ext}(\vec{r}) + e^2\int \frac{n(\vec{r'})}{|\vec{r}-\vec{r'}|}d^3r' + \frac{\partial E_{xc}[n(\vec{r})]}{\partial n(\vec{r})}\right\}\varphi_i(\vec{r}) = \epsilon_i \cdot \varphi_i(\vec{r}) \tag{2.62}$$

$$\left\{-\frac{\hbar^2}{2m}\nabla^2 + V_{eff}\right\}\varphi_i(\vec{r}) = \epsilon_i \cdot \varphi_i(\vec{r}) \tag{2.63}$$

Equation 2.62 is a generalised single-particle Schrödinger equation. The many-particle potential is replaced by an effective single-particle potential $V_{eff}(\vec{r})$ (equation 2.63).

The Kohn-Sham theorem consists of the ground-state density of an N-particle problem:

$$n(\vec{r}) = \sum_{i=1}^{N} |\varphi_i(\vec{r})|^2 \tag{2.64}$$

and the Kohn-Sham equation:

$$H_{KS} \cdot \varphi_i = \epsilon_i \cdot \varphi_i. \tag{2.65}$$

The Kohn-Sham equations have a self-consistency problem, which means that an iterative process is needed due to the fact that the solutions determine the original equations [64]. The solution has to be known to solve the problem.

DFT is the exact description of the quantum mechanical many-body problem and hence, the behaviour of electrons in a periodic potential like a crystal is described. The interpretation of the electronic structure and the corresponding material properties in EELS are supported by DFT simulations. The density of states and EELS spectra in chapter 5 and especially, in section 5.4 are calculated by using the WIEN2k code [67], a full potential, linearised augmented plane wave DFT method.

Chapter 3

Methods and Material

The following chapter informs about the instrumentation and the analytical methods used to describe the electronic and magnetic properties. A detailed description of the thin film synthesis is also given. Additionally it contains a section about the analysed characteristic microstructure of the thin films (LSMO and LCMO) on different substrates.

3.1 Instrumentation

3.1.1 Transmission Electron Microscope

Modern TEMs are complex analytical instruments with a large variety of applications, which informs about the microstructure of the material and its physical and chemical properties. Free electrons are accelerated to high tensions of about 200 kV and collected by electromagnetic lenses. The electron beam is focused by the condenser lens system and transferred to the sample. The objective and projective lens system deflect the transmitted beam to the viewing screen with a high spatial resolution.

In general, the visual perception of our environment is enabled via the sight of our eyes, which is a complex organ operating as a converging lens. Under a distance of most distinct vision of 25 cm, the resolution of the human eye is around 75 µm. The research of smaller structures beyond the limit of human sight is supported by the microscope (Greek: mikrós = small, skopeîn = see). The light microscope is known since the 16th century and its resolution was constantly improved and achieves a range of 300 nm nowadays [68]. The spatial resolution of the microscope is in principal limited by diffraction. In 1873 Abbe [69] found that structures smaller than the half wavelength of light cannot be resolved (equation 3.1), which is still valid. The resolution d of the microscope is defined by

$$d = 0.61\lambda/\sin\alpha \tag{3.1}$$

where λ is the wavelength of light and α the aperture angle. An improvement of the resolution can be achieved by using smaller wavelengths. In 1924 *Louis de Broglie* declared wave-particle duality of matter that particles with a rest mass greater than zero possess a wave character. Their wavelength λ is

$$\lambda = \frac{h}{p} = \frac{h}{m \cdot v} \tag{3.2}$$

where h describes the Planck's constant, p is the momentum, m is the mass and v is the velocity. The great achievement was to use a different medium, e.g. electrons, instead of light. The benefits of electrons are a simple production by thermionic emission, the simple manipulation and acceleration of these charged particles and their detection by electron multiplying devices. The state of the electron is described by five specifications: mass, charge, energy, momentum and spin. The small wavelength of fast electrons enables the investigation of small structures.

The challenge to overcome the Abbe's diffraction limit motivated Knoll and Ruska [70] to invent the TEM in 1932. The design resembles the light microscope, however, the utilised probes are electrons instead of photons. The imperfection of electromagnetic lenses is an important issue in electron optics due to the significantly reduction of the achieved resolution. The lens defects can be separated into two groups, monochromatic and chromatic defects. The monochromatic lens defects are astigmatism and spherical aberration. The astigmatism concerns deviations of the rotational symmetry of the lens field due to inhomogeneities and contaminations. The spherical aberration arises due to the inhomogeneity of the lens field resulting in a different behaviour of off-axis electrons. The second group of lens defects consists of chromatic aberrations. These chromatic aberrations result from electrons with different velocities, fluctuations of the acceleration voltages and energy losses after interaction with the sample.

As described at the beginning of this section the standard transmission mode in

TEM uses lenses to magnify the region of interest and form the image. Therefore, chromatic aberration limits the image resolution, which is absent in scanning TEM (STEM) mode provided by most TEMs. The main advantage compared to the TEM mode is the highly focused electron beam, which is scanning across the sample. The STEM mode works in the diffraction mode and additional to the lenses, deflection scan coils are installed between condenser and objective lens systems to probe with the electron beam across the sample. The transmitted beam is transferred through the projective lenses to the STEM detectors. The quality of the STEM image depends on the lens formed probe and thus, aberrations influence the probe.

For all experiments realised at USTEM two conventional TEMs equipped with a thermionic LaB_6 electron gun (FEI TECNAI G20) and a field emission gun (FEI TECNAI F20) were used. Both TEMs work in the free high tension mode, which allows to accelerate the electrons arbitrary adjustable in the range from 10 kV to 200 kV. Both TEMs at USTEM achieve a spatial resolution of 0.24 nm.

An important challenge in TEM beside the spatial resolution is the improvement of the energy resolution in EELS as shown in chapter 5. On the one hand an improvement is achieved by using Richardson-Lucy (RL) algorithm [71]. On the other hand the energy resolution becomes significant better by using a monochromator [72]. Within a collaboration with Ing. Michal Horák at Central European Institute of TEChnology (CEITEC) in Brno/Czech Republic some experiments were carried out using a FEI Titan Themis which is equipped with a monochromator. For all low temperature experiments a cryo-transfer holder (GATAN 915) was used to operate at a temperature of 85 K.

3.1.2 Electron Energy Loss Spectrometry

EELS in TEM is based on inelastically scattering of the high-energy electrons on atoms of a specimen (as already described in section 2.2). The EELS spectrum is characterised by the selection of transmitted electrons in accordance to their energy losses. These electrons provide compositional and chemical information from subnanometre areas of the specimen. The electronic, optical and magnetic properties describe a number of specimen characteristics, e.g. thickness, atomic structure, bonding, free-electron density, bandgap, dielectric response and magnetism. The advantages of EELS are:

- high spatial resolution of < 1 nm
- low detection limit of a few atoms
- in transmission geometry the whole volume is probed compared to surface sensitive methods (atomic force microscope or Auger detection)

In general, the EELS spectrum can be separated into two parts, the low loss (valence) section from 0 to 50 eV and the core loss section ($>$ 50 eV) [52, 68]. Figure 3.1 shows the whole EELS spectrum of NiO and the correlation between energy-level diagram for NiO and EELS spectrum [68]. As it is generally known, the inner shell electrons are placed deeper in the potential well and are not influenced by each other. Hence, high-energetically ionisation edges are at a characteristic energy, while low-energetically ionisation edges are influenced by a chemical shift.

For recording an EELS spectrum with a well defined energy dispersion two types of spectrometer exist: i) in-column spectrometer and ii) post-column spectrometer. The first one is implemented in the projector lens system. The latter is mounted at the end of the beam path and has the advantage that it can be retrofitted to almost any TEM. At USTEM the FEI TECNAI G20 is equipped with a GATAN post-column energy filter (GIF 2001) and the FEI TECNAI F20 has mounted a GATAN Tridiem energy filter. The FEI Titan Themis at CEITEC has a GATAN GIF Quantum ERS 966 post-column energy filter.

Valence EELS

Low energy losses are caused by the excitation of valence or conduction electrons. The experimental technique that deals with this part of the EELS spectrum is called VEELS for valence EELS. VEELS is used for detecting bandgaps or for characterising optical properties of materials. In contrary to inner shell electron excitations no sharp energy edges exist in the VEELS spectrum and it is more like a range of energy within the valence or conduction band [73]. These low losses can be described by the many-body theory (see section 2.2.2). Due to the collective excitation of the electrons the solution of the many-body problem is solved by using a response function like the dielectric function $\epsilon(q, \omega)$ which describe the electron-solid exchange. The theoretical observation of the VEELS spectrum is possible by measuring optical data like refractive index and absorption coefficient, which are coherent with the real

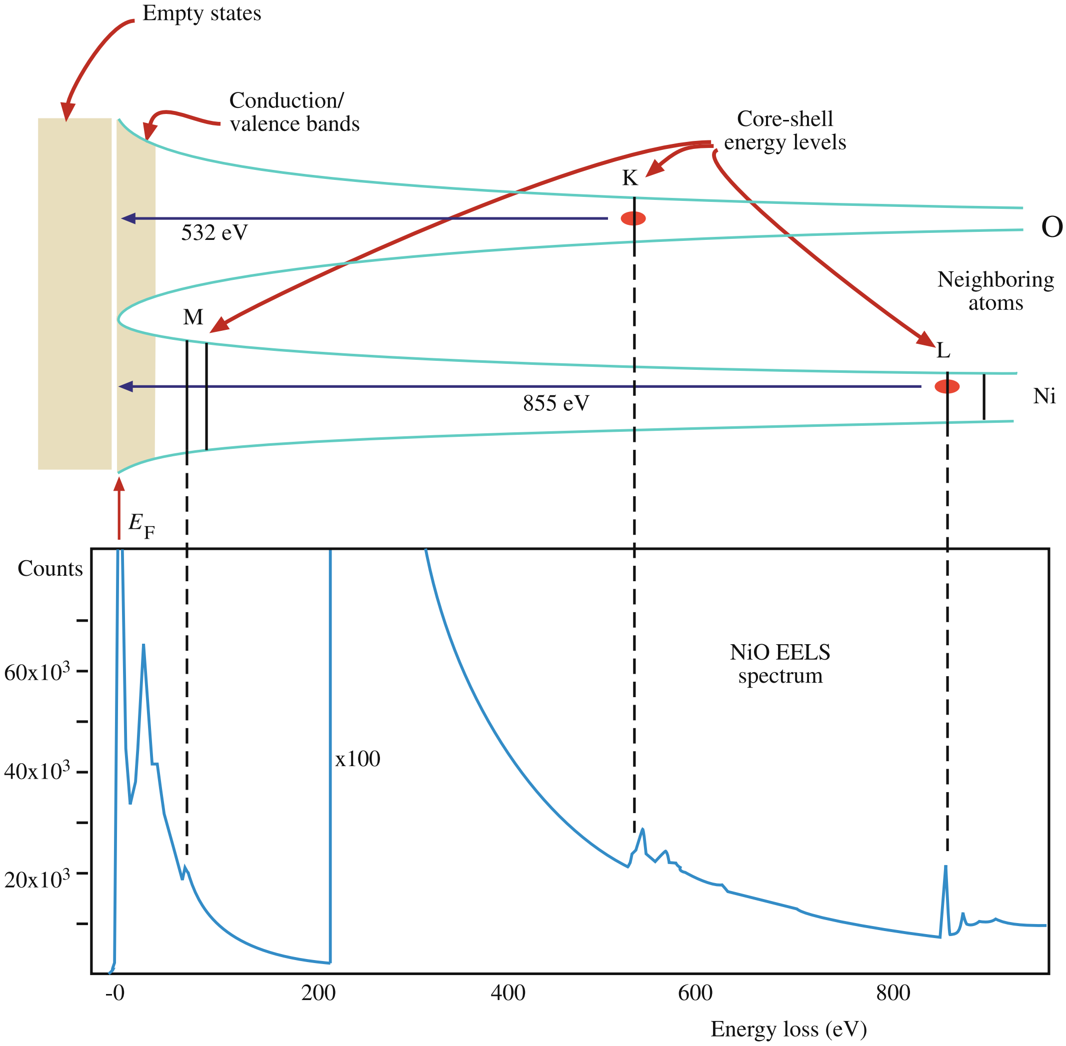

Figure 3.1: Correlation between potential well and EELS spectrum. [68]

and imaginary part of the dielectric function. The relation between dielectric function and energy loss probability is described by the Kröger equation (equation 2.48, section 2.2.3). The simplified assumption of the Kröger equation is the SSD (equation 2.44, section 2.2.2), which shows the direct proportionality of the scattering probabilty and the loss function $\Im\left[-\frac{1}{\epsilon(\omega)}\right]$:

$$SSD(\omega) \propto \Im\left[-\frac{1}{\epsilon(\omega)}\right] \tag{3.3}$$

A fundamental physical limit on spatial resolution for the inelastic signal at lower energy losses is the inelastic delocalisation [74, 75]. The inelastic delocalisation describes the localisation distance of an incident beam electron interacting with a bound atomic electron due to the long range Coulomb force. The observation of the delocalisation can be done under consideration of the Heisenberg uncertainty principle:

$$\Delta x \Delta p \sim h \tag{3.4}$$

where Δx is the localisation distance, Δp is the momentum uncertainty and h is the Planck's constant. The momentum uncertainty can be assumed as:

$$\Delta p = \hbar q \sim \left(\frac{h}{\lambda}\right)\Theta_E \tag{3.5}$$

and the characteristic angle is

$$\Theta_E \sim \frac{E}{2E_0} \tag{3.6}$$

where E is the specific energy loss and E_0 is the energy of the incident electrons. The inelastic delocalisation is decreasing with increasing energy loss E due to the fact that Δx is proportional to $1/E$:

$$\Delta x = \frac{\lambda}{\Theta_E} \tag{3.7}$$

Hence, observations in the very low loss part of a VEELS spectrum are always delocalised. The delocalisation length d_{50} contains 50 % of the inelastic scattered electrons and describes well the delocalisation considering the collector angle β:

$$(d_{50})^2 \approx \left(\frac{0.5\lambda}{\Theta_E^{3/4}}\right)^2 + \left(\frac{0.6\lambda}{\beta}\right)^2 . \tag{3.8}$$

The contribution of inelastic delocalisation is decreasing by reducing the beam energy, which improves the spatial resolution of VEELS. However, VEELS is a powerful tool and offers some significant advantages concerning classical optical methods:

- By using electrons a high spatial resolution is obtained, which is only limited by the delocalisation of the respective energy losses. Optical methods do not reach this high spatial resolution.
- Conventional optical methods for determining the dielectric properties are limited by the wave length of the light. However, the energy range of the VEELS spectrum reaches from 0 eV to 50 eV, whereas optical methods are limited from infra-red to ultra-violet (1.7-3.2 eV). Hence, $\Im\left[-\frac{1}{\epsilon(\omega)}\right]$ contains more information and the bulk of the specimen is also probed.
- Angle-resolved measurements of dielectric properties are possible. In contrast to optical methods, there are no limitations to direct and indirect bandgap measurements in VEELS.

In figure 3.2 the shape of a typical VEELS spectrum with its three main features is shown:

- ZLP at 0 eV followed by
- bandgap and interband transitions
- and the volume plasmon.

For the CMR effect investigations in TEM the bandgap and interband region of the VEELS spectrum are of great interest due to the dielectric properties. This region is following and partly covered by the ZLP. The full width half maximum (FWHM) of the ZLP informs about the energy resolution of VEELS spectrum, which is dependent on the electron source of the microscope. An improvement of the elastic peak of the VEELS spectrum can be achieved by using the RL algorithm or a monochromated TEM to reduce the spread of the ZLP. A typical ZLP width

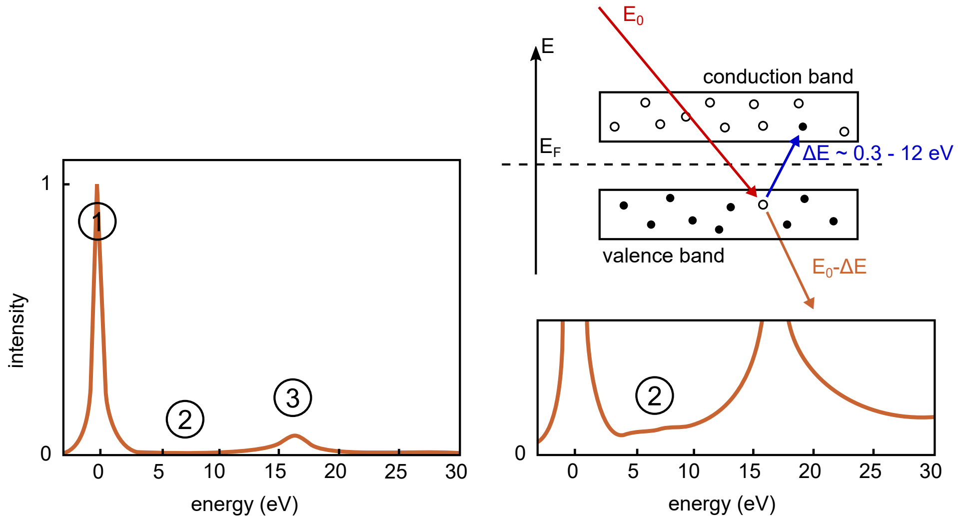

Figure 3.2: Typical VEELS spectrum showing the main features: (1) ZLP, (2) bandgap and interband region, and (3) volume plasmon.

is in the range of 0.2 - 2.0 eV. Nevertheless, the largest difficulty to overcome in VEELS analysis is the removal of this elastic peak, which is the dominant feature in the very low loss regime. Its low energy tail usually masks the signal stemming from interband transitions. Čerenkov losses and light guide modes also influence the shape of ZLP [76, 77]. These circumstances have to be taken into account when observing the energy loss spectrum.

The resistivity of double perovskites and in particular of LCMO is altering when the external magnetic field and the temperature are changed (as described in section 1.1). These environmental influences can be controlled by using a cryo holder and varying the magnetic field strength of the objective lens system in TEM for the VEELS experiments. However, a high dispersion of the spectrometer and a small FWHM are necessary to gain excellent measurements in the low loss region. The determination of the magnetoresistance is not straightforward by using VEELS. It is not a direct detection, and needs a closer look on the relation between potential well and energy loss spectrum shown by NiO in figure 3.1.

As known from the bandstructure model, a metal shows by definition no bandgap whereas an insulator or semiconductor exhibits a gap between valence and conduction band. Keeping that in mind, an energy shift in the bandgap and interband transition region due to the relation between the energy loss probability and the dielectric structure should be detectable when the material properties are changing.

All VEELS experiments at USTEM were done at the relative thickness of approximately 0.3 λ at the positions of interest at 85 K and RT. The mean free path length for inelastic scattering is λ at beam energies of 40 keV and 200 keV, respectively. The spectrometer dispersion setting was 0.1 eV per channel and the collection angle was chosen to be 8.4 mrad. The VEELS spectra were generated by multiple spectrum acquisitions. The 200 keV measurements are compiled by a summation over 50 spectra with 0.2 s for each spectrum. For the measurements at 40 keV 30 spectra were chosen with a recording times of 1.6 s. In both cases a energy resolution of 0.9 eV was achieved. For the measurements with the monochromated TEM at CEITEC the energy dispersion was 0.01 eV and the energy resolution 0.14 eV. At 60 keV and 300 keV 100 spectra were recorded with 0.1 s per spectrum.

Energy-loss Magnetic Circular Dichroism

The magnetic behaviour of an observed material can be investigated in TEM by EMCD. It is an EELS technique that gives access to the magnetisation with chemical sensitivity [23] in the nanometre scale [24, 25].

The term dichroism refers to changes of the optical absorption spectrum dependent on the polarisation by passing through a crystal. Magnetic anisotropy is needed for dichroism, while isotropic systems or cubic crystals do not exhibit this effect [78]. The classical circular dichroism depends on the helicity (handedness) of the incident light. However, in case of inorganic crystals, the chirality is induced by the magnetic moment, which is connected to circular currents in the atom [78].

A well-known standard technique for detecting the spin and orbital magnetic moments based on synchrotron radiation is X-ray magnetic circular dichroism (XMCD). XMCD determines the X-ray absorption cross selection, which depends on the polarisation [79]. The polarised X-ray absorption spectroscopy (XAS) analyses the change of X-ray absorption near edge structure (XANES) with respect to the helicity of radiation. Since it is known that dichroism of core-level transitions depends on external or internal magnetic fields, XMCD is widely used to probe the magnetic behaviour of a material.

The similarity of energy loss near edge structure (ELNES), which is the fine structure of ionisation edges in EELS, and XANES shows the availability of detecting

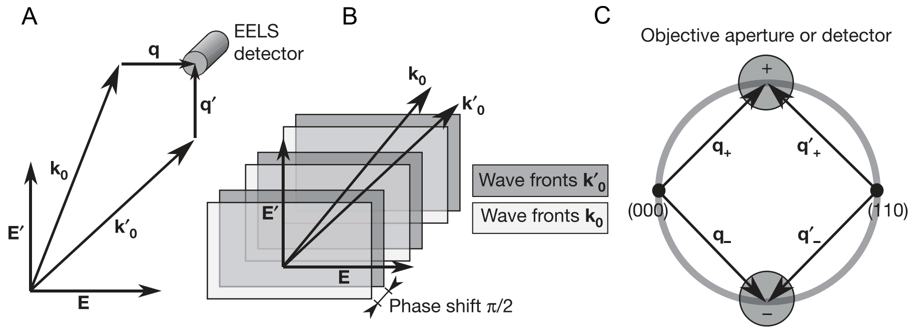

Figure 3.3: EMCD scattering geometry. A) The detector selects the wave vector transfer, B) coherent superposition of two incident plane waves with a phase shift of $\pi/2$ and C) the experimental setup shows the Thales circle with the two EELS measurement positions for the EMCD signal. [24]

circular dichroism with electrons and is theoretical described by Schattschneider et al. [80]. Already in 2003 Hébert and Schattschneider [81] suggested that EMCD is feasible due to the fact that spin-polarised electrons are not necessary. The important distinctions in EMCD compared to XMCD are the usage of the double differential scattering cross section as well as the momentum transfer $\hbar\vec{q}$ instead of the polarisation vector $\vec{e}$ [80]. The cross section for photon absorption σ of energy E is

$$\sigma(E) = 4\pi^2 E\alpha \sum_{i,f} |\langle f|\vec{e}\cdot\vec{R}|i\rangle|^2 \times \delta(E_i - E_f + E) \tag{3.9}$$

with $\alpha = e^2/(4\pi\epsilon_0\hbar c)$ being the fine structure constant, $\vec{e}$ the polarisation vector, $|i\rangle$, $|f\rangle$ are the initial and final states and $\vec{R}$ is the position operator of the target electron. In contrast to the previous expression for XMCD, the double differential cross section for EMCD is

$$\frac{\partial^2\sigma}{\partial E\partial\Omega} = \sum_{i,f} \frac{4\gamma^2}{a_0^2 q^4}\frac{k_f}{k_i} |\langle f|\vec{q}\cdot\vec{R}|i\rangle|^2 \delta(E_i - E_f + E) \tag{3.10}$$

where $\gamma = 1/\sqrt{1-\beta^2}$ is the relativistic factor, a_0 is the Bohr radius and $\vec{q} = k_i - k_f$ is the momentum transfer vector. The comparison of equations 3.9 and 3.10 shows the equivalence of polarisation vector $\vec{e}$ and momentum transfer vector $\vec{q}$ [81]. Hence, dichroism can be measured with EMCD, which was proven by Schattschneider et al. [24]. The equivalence of $\vec{e}$ and $\vec{q}$ can be described by means of special diffraction geometry called two-beam case (see figure 3.3). The circular polarisation of the incident plane waves generates a rotating electric field at the observed atom. Depending on the polarisation, this electric field achieves an alteration of the magnetic quantum number [78]. Hence, the two incident plane waves must show a phase shift of $k\lambda/4 = \pi/2$ between the horizontal and vertical electric field component [80], which is controlled by the exact EMCD setup. The phase difference of $\pi/2$ (figure 3.3B) between the two non-parallel scattered momentum transfer vector is an essential requirement to observe the EMCD effect. The double differential inelastic scattering cross section in section 2.2 is

$$\frac{\partial^2\sigma}{\partial E\partial\Omega} = \frac{4\gamma^2}{a_0^2 q^4}\frac{k_f}{k_i} \cdot S(\vec{q}, E) \tag{3.11}$$

where $S(\vec{q}, E)$ is the DFF. In case of EMCD, the expression of equation 3.11 is modified and for two off-axis positions it becomes:

$$\frac{\partial^2\sigma_\pm}{\partial E\partial\Omega} = \frac{4\gamma^2}{a_0^2}\frac{k_f}{k_i}\left[|a|^2\frac{S(\vec{q}, E)}{q^4} + |b|^2\frac{S(\vec{q'}, E)}{q'^4} \pm 2\Re\left(ab^*\frac{S(\vec{q}, \vec{q'}, E)}{q^2q'^2}\right)\right] \tag{3.12}$$

with $\vec{q} = \vec{k_i} - \vec{k_f}$ and $\vec{q'} = \vec{k'_i} - \vec{k_f}$ are the momentum transfer vectors from two incident plane waves, while a and b are the corresponding complex amplitudes. The last term in brackets of equation 3.12 relates to the MDFF [82], which is $S(\vec{q}, \vec{q'}, E)$. This interference part describes the coherence of transition with momentum transfer $\hbar\vec{q}$ and energy loss E.

The EMCD signal is the difference of the EELS spectra at specific off-axis positions (named "+" and "-") on the Thales circle (figure 3.3C), where the entrance aperture of the spectrometer is placed. It is given by

$$\frac{\partial^2\sigma_+ - \partial^2\sigma_-}{\partial E\partial\Omega} = \frac{16\gamma^2}{a_0^2}\frac{k_f}{k_i} \cdot \Re\left(ab^*\frac{S(\vec{q}, \vec{q'}, E)}{q^2q'^2}\right) \tag{3.13}$$

The symmetric parts of equation 3.12 are cancelled and the resulting dichroic signal is twice the interference part.

There are several methods to measure the EMCD effect, e.g. the classical scheme shown in figure 3.4A. Here, the crystal lattice of the sample is used as a beam splitter to achieve specific three-beam diffraction geometries. A superposition of coherent

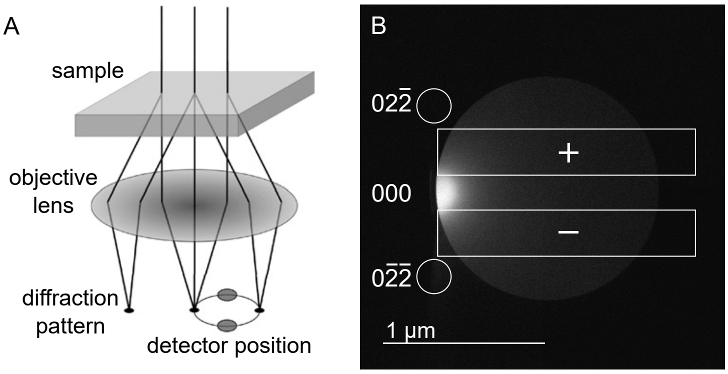

Figure 3.4: A) Experimental setup for EMCD with specific off-axis positions [83]. B) Three beam configuration of LCM100/Si for simultaneously EMCD recording [27].

wave vectors at chiral positions is achieved due to this experimental configuration described in [83]. Another method to investigate the magnetic behaviour is to record an energy ΔE - momentum transfer $\vec{q}$ map. For the acquisition a three-beam case is configured in this way that a simultaneously recording of both positions with different chiralities is achieved as shown in figure 3.4B. An advantage of this method is of course the simultaneously recording of both signals and consequently the reduced acquisition time. EMCD has some limitations, which are the aberrations of the microscope and low intensity due to the specific off-axes measurement geometry. In addition, the EMCD signal depends on the sample thickness as reported by Schattschneider et al. [80] and Löffler and Schattschneider [84]. Due to this fact, experiments were measured at an approximate thickness of 20 nm to 25 nm in the direction of electron beam.

3.1.3 Ellipsometry

The dielectric properties of surfaces and thin film specimen can be measured by ellipsometry, which analyses the polarisation alteration of the reflected light. The change of polarisation is given by the amplitude ratio Ψ and the phase difference Δ. Unpolarised light generated from a light source traverses a polariser, where light of specific electric field orientation travels trough and reflects on the specimen surface. The reflected light becomes elliptically polarised and is transferred through the rotating analyser towards the detector. [85]

For the experiments within this work an alpha-SE Ellipsometer (J.A. Woollam) with a rotating compensator ellipsometer (RCE) configuration was used. To measure the dielectric function of the specimens the whole wavelength ranging from 380 nm to 900 nm was utilized.

The ellipsometry measurements were carried out in collaboration with Viktoria Ritter, MSc of Prof. Alois Lugstein's group at the Institute of Solid State Electronics at Technische Universität Wien.

The results from the ellipsometer measurements give some indications of the dielectric properties in the low loss region of the EELS spectrum. Hence, the ellipsometry data are processed by the Kröger equation to achieve an energy loss spectrum, which is comparable to the experimental VEELS spectrum.

3.2 Synthesis and Sample preparation

Thin film specimen synthesis was carried out by pulse laser deposition (PLD) preparation technique. The PLD target synthesis of LCMO was done by the Pechini method using stoichiometric mixture of high purity La_2O_3, Co_3O_4 and $MnCO_3$. In case of LSMO, a LSMO (Sigma-Aldrich) powder was used for the PLD target production. The preparation procedure was similar to Mahato et al. [86]. The deposition conditions were as follows: the oxygen pressure was set under 0.12 mbar at 1033 K, a wavelength of 248 nm and a pulse frequency of 5 Hz was achieved by using a KrF excimer laser. The energy of the laser beam was set to 400 mJ per pulse and the target-substrate distance was adjusted to 0.06 m. Three different substrates were used: $LaAlO_3$ (LAO), $SrTiO_3$ (STO) and Si. An overview of the synthesised specimen and their deposition conditions is given in table 3.1.

The synthesis of thin film samples was done in collaboration with our FOXSI project partner Dr. Edvinas Navickas in the research division electrochemistry of Prof. Jürgen Fleig at Technische Universität Wien.

TEM sample preparation of the cross section lamella was performed by focused ion beam (FIB) FEI Quanta 200 3D DualBeam. The Ga^+ ions were accelerated to 30 kV operating voltage for the cutting process and reduced to 5 kV for the cleaning process. As final step of the preparation, soft Ar^+ ion polishing was done by using a Technoorg-Linda GentleMill operated in the range of 0.5 keV to 1 keV.

Table 3.1: The observed samples with their deposition conditions: LF = laser frequency, t = time, T = temperature, OPP = oxygen partial pressure, LT = layer thickness.

sample	LF	t	T	OPP	LT	substrate
LSM40/STO[1]	10 Hz	5 min	650 °C	10 mTorr	40 nm	STO
LSM40/LAO[1]	10 Hz	5 min	650 °C	10 mTorr	40 nm	LAO
LSM70/LAO[1]	10 Hz	8 min	650 °C	10 mTorr	70 nm	LAO
LSM100/LAO[1]	10 Hz	15 min	650 °C	10 mTorr	100 nm	LAO
LCM100/STO[2]	5 Hz	20 min	760 °C	90 mTorr	100 nm	STO
LCM80/LAO[2]	5 Hz	30 min	650 °C	900 mTorr	80 nm	LAO
LCM300/Si[2]	10 Hz	155 min	610 °C	30 mTorr	300 nm	Si

[1] $La_{0.8}Sr_{0.2}MnO_3$ (LSMO)
[2] La_2CoMnO_6 (LCMO)

3.3 Microstructure and Characteristics

Double perovskites, in particular with ABO_3 structured compounds, are multifunctional materials and promise a wide range of applications, eg. cathodes of solid oxide fuel cells [11] and magnetic storage [12]. Concerning the comparison of thin film samples and bulk, the material properties behave different at various scales. For modern technologies like nanotechnologies, it is of great interest to understand and know the microstructure and its characteristics of the thin films. The investigated thin films are epitaxially grown on a single crystal (STO, LAO and Si) and their orientations are particularly affected by the lattice parameter of the substrate and the layer. Concerning the different materials (heteroepitaxy) of the film and the substrate, the misfit induces epitaxial stress, which can be degraded through the growth of the film. The morphology of the substrate is essential for the epitaxial growth of the deposited layer. The structure is easily influenced by defects and strains. The impact of these perturbations to the material properties like CMR is reported by Haghiri-Gosnet et al. [12]. Stress in the structure of manganites correlates with their physical properties. Due to this fact, the microstructure and its behaviour were investigated with respect to the thin film thicknesses by means of bright field (BF) and dark field (DF) TEM images, diffraction and high-resolution TEM (HRTEM). Structural characteristics are different compared to the individual grown thin films.

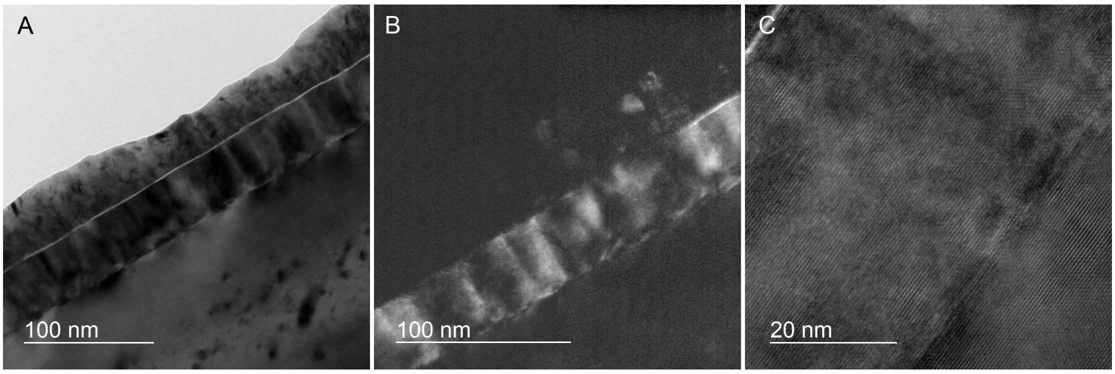

Figure 3.5: LSMO film on LAO substrate (LSM40/LAO). A) BF image shows the cross section of a multilayer, which consists of the substrate at the bottom followed by the LSMO layer and the FIB protection layer on the top. A kind of columnar structure is visible in the thin film layer. B) The corresponding DF image of previous BF image confirms this impression. C) The HRTEM image shows the epitaxially grown layer with induced strain.

3.3.1 $La_{0.8}Sr_{0.2}MnO_3$

The investigation of LSMO thin films at 40 nm, 70 nm and 100 nm thickness exhibits an interesting structure caused by defects, induced strain and lattice mismatch. In figure 3.5 a contrast difference in the grown layer between the substrate and the protection layer can be seen, which is mostly perpendicular to the surface of the substrate and is drawn through the thin film. This is a typical behaviour of the perovskite microstructure as known from [29, 87] and evokes connotations of columnar artefacts, which is shown in the TEM images at BF and DF mode. However, this effect induced by strain and lattice mismatch is not very pronounced (figure 3.5C) and there are no columnar structures visible in the HRTEM images.

The layer of LSM40/LAO and LSM40/STO are epitaxially grown as shown in figure 3.5C and have a thickness of about 40 nm. These two samples vary in terms of their substrate. As the name of the sample suggests, the substrates are LAO and STO, respectively. The TEM analysis of these specimens confirms tensile in-plane strain in the film layer growing on STO and compressive in-plane strain for the layer on LAO as reported by Navickas et al. [88]. The X-ray diffraction (XRD) investigations of Navickas came to the same conclusions. This behaviour was also expected due to the comparison of the known bulk lattice parameters from LAO, STO and LSMO ($a_{LAO} = c_{LAO} = 3.820$ Å, $a_{STO} = c_{STO} = 3.910$ Å, $a_{LSMO} = c_{LSMO} = 3.989$ Å), which supports a lattice mismatch. The misfit Δ from the bulk parameters in percentage is given by

$$\Delta = \frac{d_{Substrate} - d_{LSMO}}{d_{Substrate}} \cdot 100 \tag{3.14}$$

where d_{LSMO} and $d_{Substrate}$ are the lattice plane distances of LSMO and the substrate. The lattice mismatch of LSM40/STO is 0.31 % and thus, tensile in-plane strain is expected. In the case of LSM40/LAO the misfit is -2.04 % due to the smaller lattice parameter and which causes compressive in-plane strain. No significant changes of the microstructure of thin film or interface are observed by changing the substrate.

In the next step the layer thickness was increased and this specimen is named LSM70/LAO. Compared to LSM40/LAO only the deposition time has changed and as a result of the extended deposition time the layer reaches a thickness of around 70 nm. By taking a closer look to the cross section of the LSMO thin film a featureless layer grown on the LAO surface and a non-homogeneous layer are revealed as also reported by Lebedev et al. [89]. The BF image (figure 3.6A) and especially the DF image (figure 3.6B) illustrate two separate layer inside the LSMO film due to the difference in contrast. Both layers are epitaxially grown, however, the second layer of the thin film convey the impression of a strong inhomogeneity and shows the same features as the previous samples. More dislocations and strain evolve in this layer as shown in the HRTEM images of figure 3.6C-F. The columnar features occurs perpendicular to the interface of the featureless band and a tendency to columnar structures is visible for example due to the shading effect (figure 3.6C). These columnar features mainly arise at the interface of the featureless band and grows to the surface of the LSMO film. However, this is not a mandatory behaviour, the features can arise somewhere within the layer and vanish before achieving the surface. Only the growth direction is more or less normal to the interface.

By extending the layer thickness to 100 nm, a non-uniform distribution of the LSMO compound in sample LSM100/LAO was detected. The high-angle annular dark field (HAADF) image in STEM mode gives an impression of the elemental distribution in the thin film (figure 3.7). Lighter elements appear darker than heavier elements under a certain camera length of below 100 nm and due to this fact it is also called Z-contrast map. This result can be affected by thickness effects because a

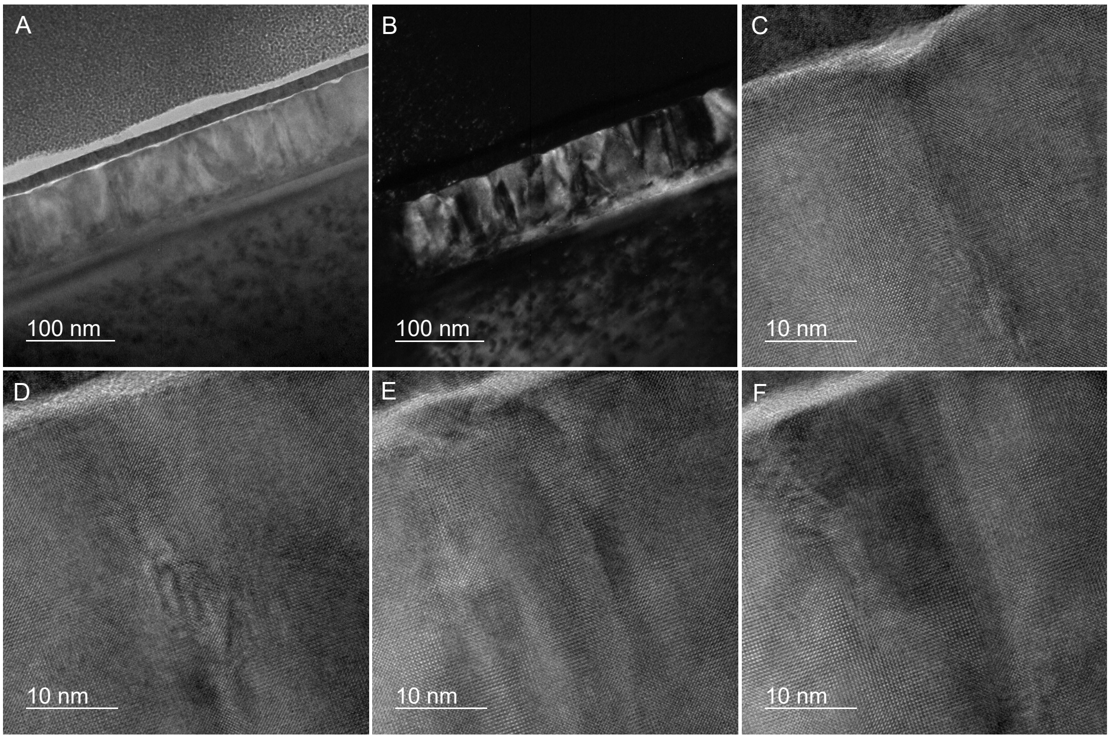

Figure 3.6: A) BF image and B) DF image of LSM70/LAO show an inhomogeneity of the thin film. C-F) HRTEM images convey the impression of more induced strain and dislocations.

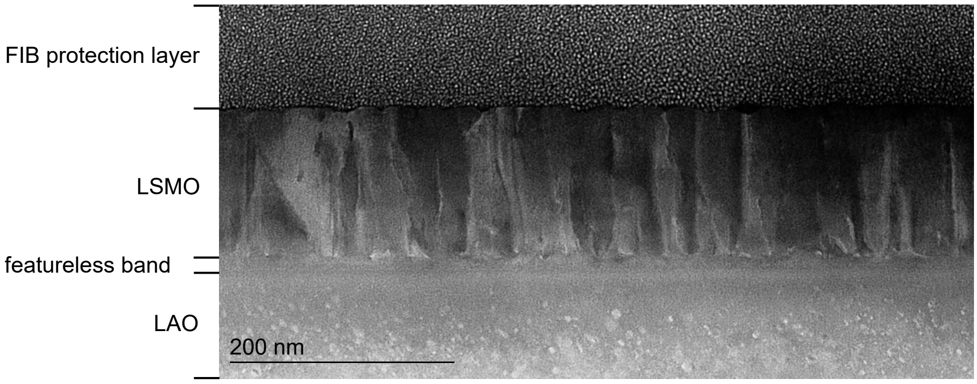

Figure 3.7: The structure of LSM100/LAO consists of the substrate on the bottom side, the LSMO film is placed in the middle and on the top the Pt-C FIB protection layer. This HAADF image of LSM100/LAO enables a Z-contrast map and exhibits a segmentation into a featureless band parallel to the LAO substrate and the second LSMO layer with non-homogeneous element distribution.

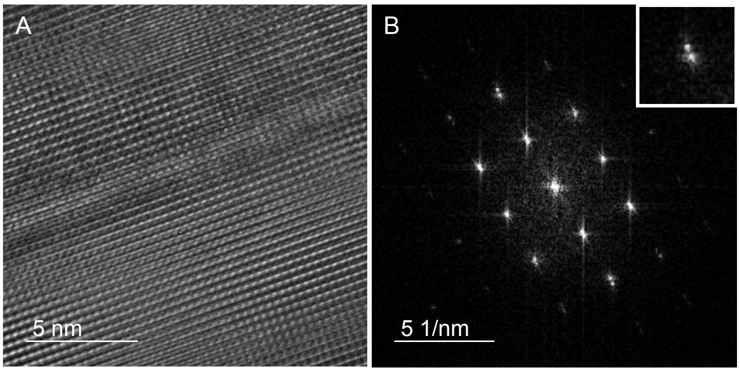

Figure 3.8: A) The HRTEM image shows the interface between LSMO and LAO. B) The corresponding FT at this position exhibits in the insertion spot splitting of diffraction spot (300).

essential precondition is that the observed area has the same lamella thickness. If the lamella thickness in the observed area is homogenous than a Z-contrast assumption can be done.

Nevertheless, LSM100/LAO behaves similar to the previous samples, which is why a segmentation of the LSMO film can be observed here as well. A small featureless band parallel to the substrate surface due to the contrast difference compared to the substrate is visible in figure 3.7. The substrate itself shows some bright inclusions, which can be attributed to the final TEM lamella preparation step done by soft Ar^+ ion polishing. The second LSMO layer placed on this band exhibits the columnar features with an elemental distribution, which shows that heavier elements are more accumulated in these columnar structures and the lighter elements are in between. The sputtering geometry of the final thinning process by GentleMill has to be in mind, when thinking of Z- or Bragg contrast. The TEM lamella is placed into the GentleMill in a way that the FIB protection layer is facing the Ar^+ beam. The lamella was polished under a certain angle of six degree. As a result the region at the interface between LSMO and protection layer is slightly thinner than the region at the LSMO-LAO interface. The bright spots in the substrate can be material sputtered from the TEM grid or the protection layer, which consist of Cu or Pt-C. Considering the polishing step, the HAADF image shows also columnar structures in the thicker region of the LSMO film.

In figure 3.8 a HRTEM image and the corresponding FT of the LSMO-LAO interface are shown. A spot splitting perpendicular to the interface is determined by observing the FT (figure 3.8B) and occurs from lattice mismatch. The FT can be well indexed, the lattice parameter of LSMO is 3.901 Å and of LAO 3.787 Å. A misfit of -3.01 % is detected and thus, it is in a good agreement to the bulk value. Due to the small lattice mismatch the unit cell becomes slightly elongated normal to the interface and a splitting of the (300) diffraction spot is readily observable.

In addition, a series of HRTEM images was recorded and merged together (figure 3.9). This figure displays the LSMO layer and also the polycrystalline FIB protection layer on the top left side. The thin film exhibits columnar features packed very close to each other. The distance between the features is around 20 nm and in between there is no structural change observable. The epitaxy in the microstructure is only interrupted by the columnar features, which arise directly at the interface within a heavily strained region as confirmed by Van Tendeloo et al. [87].

3.3.2 La_2CoMnO_6

The previous samples differ in substrate and deposition time, which only influences the layer thickness, whereas the LCMO samples were synthesised under different deposition conditions. The LCMO thin film of LCM100/STO was grown by lower laser frequency, higher temperature and a oxygen partial pressure which was nine times higher than for the previous samples (see table 3.1). LCM100/STO behaves similar to LSM100/LAO, but there is no precise interface between the featureless band and the columnar layer. However, a small band parallel to the surface of the STO substrate is visible in figure 3.10A. The thickness of this band varies and is interrupted by columnar structures which arise due to the strain at the LCMO-STO interface as shown in the BF (figure 3.10B) and DF (figure 3.10C) image.

LCM80/LAO possess a completely different microstructure than previous samples due to the formation of a polycrystalline film of around 80 nm with a different orientation of each grain. The reason for this behaviour of the microstructure is the extreme high oxygen partial pressure during the synthesis compared to the other samples. Crystalline and amorphous grains are randomly deposited side by side in a cluster as shown in figure 3.11. Compared to the previous LCMO specimen the substrate has changed to LAO and the oxygen partial pressure is ten times higher. This is attributed to the attempt to produce a thicker double perovskite film. The layer lost its epitaxially microstructure and formed grains. Nearly each grain is

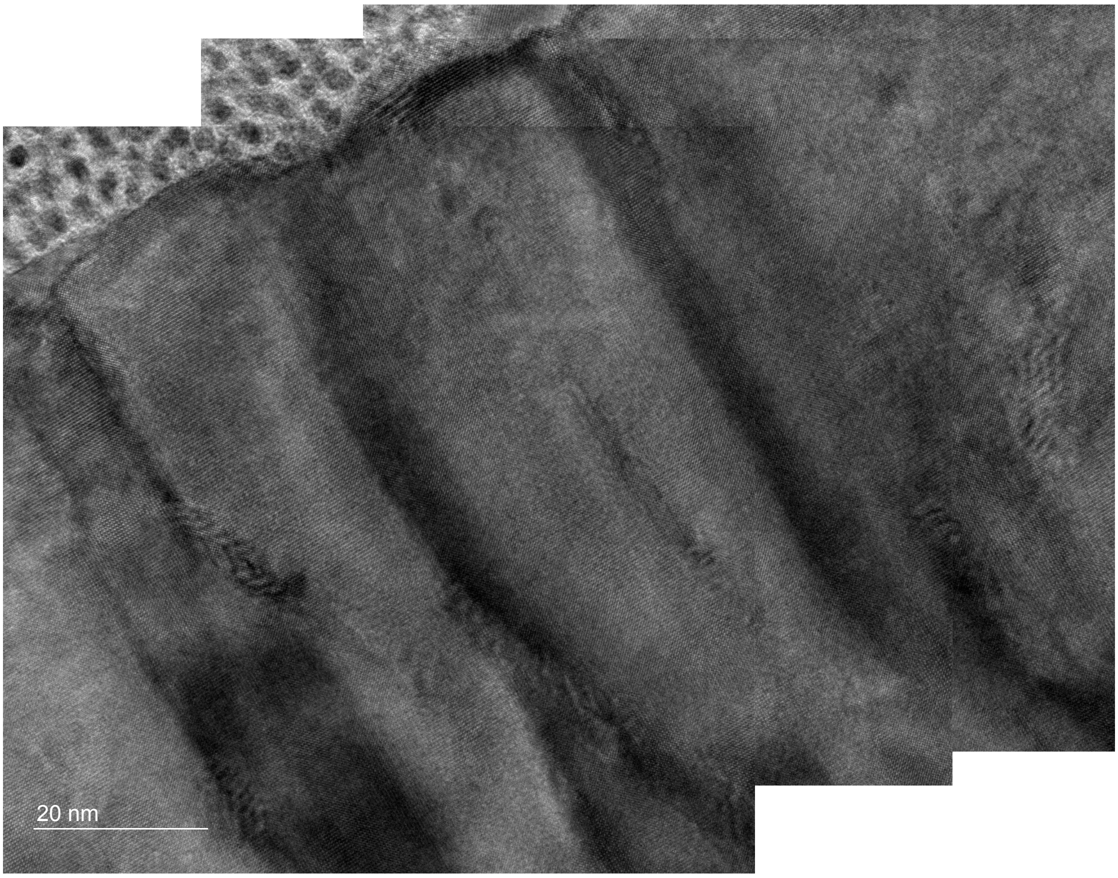

Figure 3.9: HRTEM images of the LSMO layer merged together and showing a columnar structure arising from the LSMO-LAO interface (on the bottom right side) to the FIB protection layer (on the top left side).

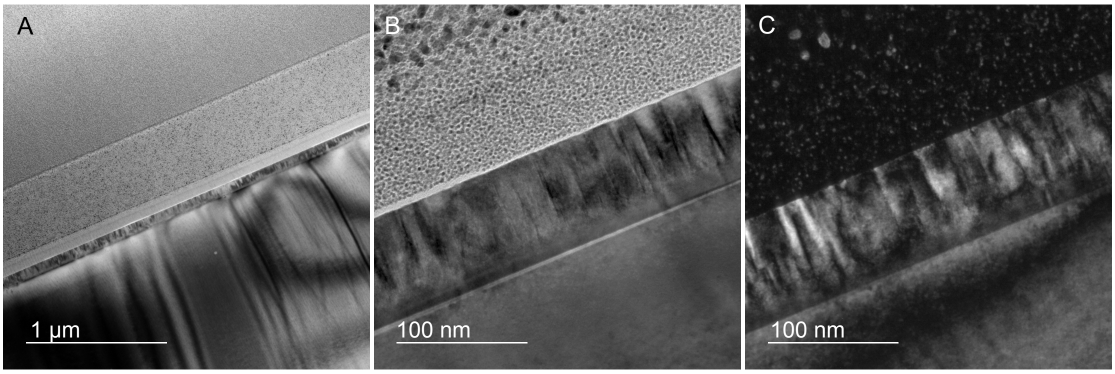

Figure 3.10: LCMO on STO (LCM100/STO). A) Overview of the multilayer shows the tense LCMO film. The B) BF and C) DF images confirm the columnar structure in the 100 nm layer.

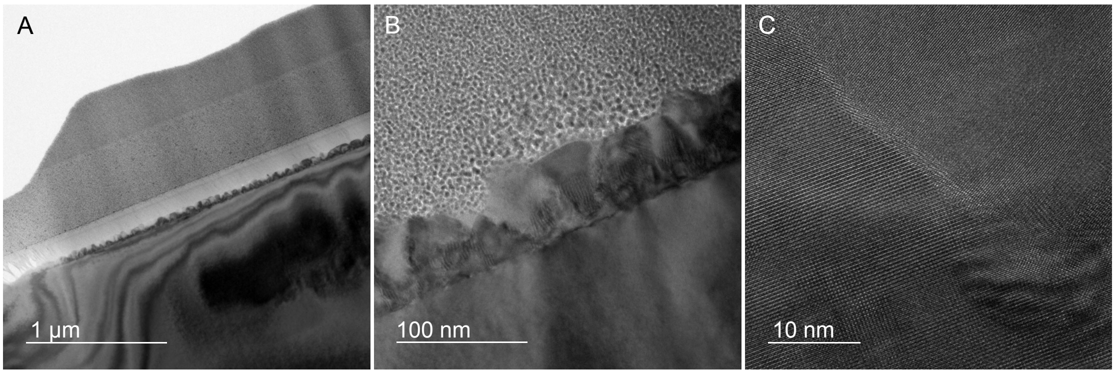

Figure 3.11: A) Polycrystalline microstructure of LCMO on LAO (LCM80/LAO). The B) BF image shows the non-epitaxial growth of the layer and C) the different orientations of the grains.

distorted by tensile and compressive strain as shown in figure 3.11B. The HRTEM image (figure 3.11C) exhibits a grain boundary, where two differently oriented grains converge.

Figure 3.12 gives an impression of specimen LCM300/Si. The film was deposited by means of magneton sputtering on monocrystalline Si and the deposition time was five times longer due to the production trail of a thicker LCMO film. The layer confirms the previous results and shows columnar growth due to lattice mismatch of -1.84 % between Si (lattice parameter a = 5.43 Å) and LCMO (a = 5.53 Å). The columns are more dominant and the induced strain is packed more dense compared to other samples. Different crystallographic oriented regions are separated by columns as shown in the HRTEM image (figure 3.12C).

In conclusion, microstructural characteristics of thin films are strongly affected by strain. The lattice mismatch caused in the interface region between layer and substrate imposes a strain pattern, which also influences the epitaxial growth. Epitaxy means an oriented growth of the layer crystal on the surface of the single crystalline substrate. The deposited films of 40 nm thickness on STO and LAO possess tensile and compressive in-plane strain. The induced stress in the structure correlates with defects and dislocations. Hence, LSM40/STO and LSM40/LAO exhibit contrast variations in the BF and DF images, while at HRTEM mode only epitaxial growth is detected and convey the impression of a monocrystalline layer. By extending the layer thickness to 70 nm and 100 nm the same contrast indications as shown for the previous samples are observed at lower magnifications. However, columnar features

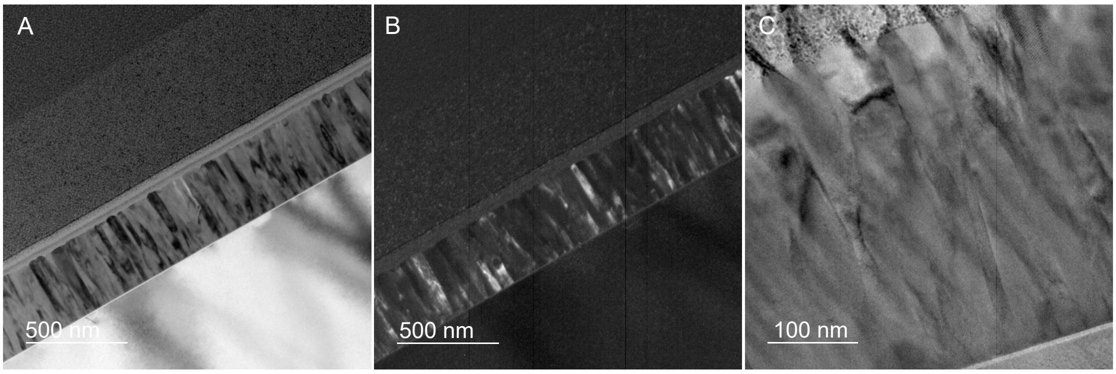

Figure 3.12: Specimen LCM300/Si consist of LCMO placed on Si: A) BF image of the multilayer shows the inhomogeneity of LCMO layer confirmed by the B) DF image. The presence of the columnar structure is affirmed and exhibits at the HRTEM image dense packed strain and defects.

were detected by means of HRTEM imaging and confirmed by HAADF analysis.

The evolution of these columnar features arises from a featureless band grown on the LSMO-LAO interface. The deposition parameters and the substrate were changed, which leads to columnar features in LCM100/STO. However, the featureless band exhibits interruptions due to these columnar structures. A strong increase of the oxygen partial pressure in the synthesis of LCM80/LAO results in polycrystalline cluster of heavily strain and randomly oriented crystalline and amorphous grains. An additional change of the deposition parameters and by using a single crystalline Si substrate for the synthesis of LCM300/Si enables a growth of a 300 nm thick LCMO layer, which is fully relaxed and non-epitaxial. Columnar structures were clearly visible with in geometric randomly orientated phases. The increasing thickness of the thin films results in large strain energies and formations due to misfit dislocations are more favourable [88]. All analysed specimens and their specific characteristics are summarised in table 3.2.

Table 3.2: Synoptic table of the investigated samples with their microstructural characteristics.

sample	layer thickness	substrate	crystallinity	columnar structure
LSM40/STO[1]	40 nm	STO	mono	indications
LSM40/LAO[1]	40 nm	LAO	mono	indications
LSM70/LAO[1]	70 nm	LAO	mono	indications
LSM100/LAO[1]	100 nm	LAO	mono	indications
LCM100/STO[2]	100 nm	STO	mono	indications
LCM80/LAO[2]	80 nm	LAO	poly	no
LCM300/Si[2]	300 nm	Si	poly	yes

[1] $La_{0.8}Sr_{0.2}MnO_3$ (LSMO)

[2] La_2CoMnO_6 (LCMO)

Chapter 4

FOXSI Collaborations

This chapter is an excerpt of the collaborations within the FOXSI project. The project partners are supported by TEM investigations on their specific concerns. The outcomes of these collaborations are summarised and reflect the contribution of the author to the rendered research.

4.1 Yttria-stabilised Zirconia

The chemical and structural alteration of yttria-stabilised zirconia (YSZ) thin films were analysed in collaboration with the research group of Prof. Bernhard Klötzer (Institute of Physical Chemistry, University of Innsbruck) and is published by Götsch et al. [90]. A well-known and widely used material due to its various properties is YSZ. Nevertheless, the influence of yttria on the crystal structure and the ionic conductivity is often not considered as reported [90]. The investigated YSZ thin films have different yttria compositions, which consist of 3 mol% (3YSZ), 8 mol% (8YSZ), 20 mol% (20YSZ) and 40 mol% (40YSZ) Y_2O_3.

These four samples were analysed with respect to chemistry and structure with energy-dispersive X-ray spectroscopy (EDX) and EELS in TEM and STEM mode. The respective spectra of these samples are shown in figure 4.1. The EDX spectra exhibit more than the expected elements Zr, Y and O, which can be easily explained: For the TEM investigations, the YSZ thin films are placed on a TEM grid made of Au and that is responsible for the Au peak. The Cu peak stems from the specimen holder and due to the pole pieces of the objective lens system Fe and Co are detected. The Na and Cl contributions are caused by the substrate. However, an intensity

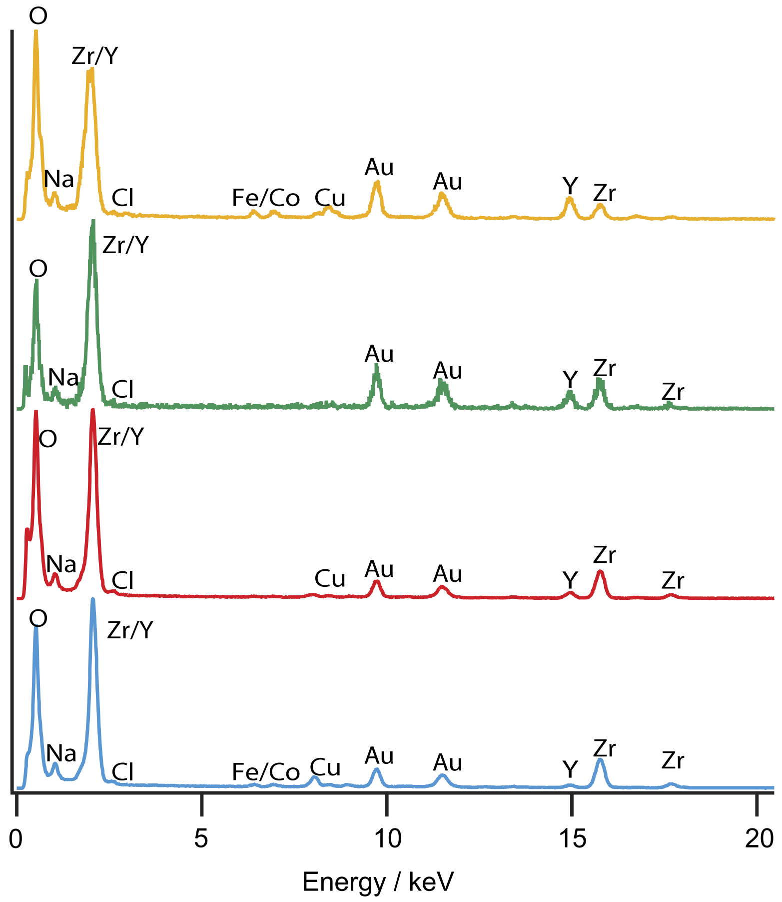

Figure 4.1: EDX spectra of different compositions recorded in TEM. The 3YSZ spectrum is blue, 8YSZ is red, 20YSZ is green and 40YSZ is yellow. Beside the expected elements additional contributions to the EDX spectra are detected, which are attributed to TEM grid, specimen holder, pole pieces and preparation process. [90]

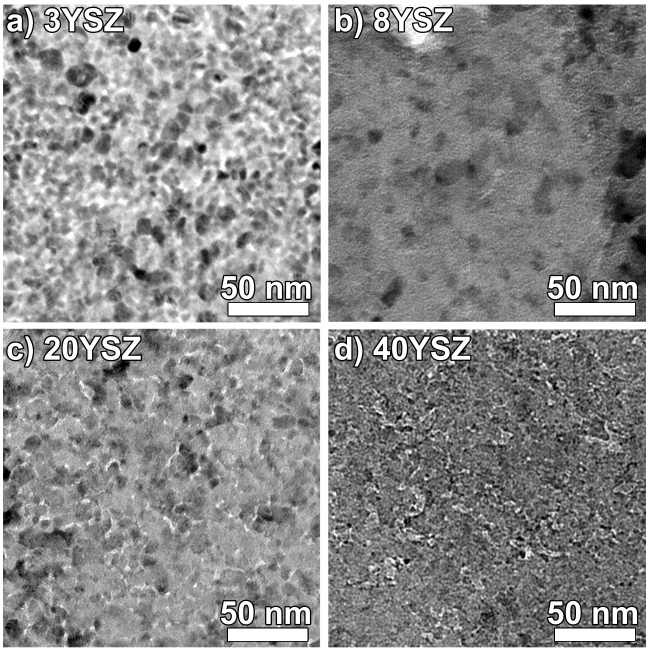

Figure 4.2: BF images of the four specimens show the microstructure at different Y_2O_3 content. The sample with the smallest grains is c) 20YSZ followed by a) 3YSZ and b) 8YSZ. Sample 40YSZ shows a corrugate and irregular microstructure. [90]

variation of the interesting Zr and Y edges is detected.

The quantification of EDX-TEM, EDX-STEM and EELS spectra results by calculating the mean in the following values: for 3YSZ 3.3(7) mol% Y_2O_3 is measured, for 8YSZ 8(2) mol%, for 20YSZ 17(2) mol%, and for 40YSZ 38(3) mol%. An overview of the microstructure is shown in figure 4.2. The morphology of the thin films exhibits small nanocrystallites. The smallest crystals are found in sample 20YSZ, the crystal size increases in 3YSZ and in case of 8YSZ the largest grains are measured. The diffraction contrast results from different Bragg orientations of the grains. The crystals are of different size having the darker and brighter ones randomly ordered. Sample 40YSZ has a corrugated and irregular microstructure compared to the others.

However, all four samples confirm the polycrystalline impression due to the selected area electron diffraction patterns (see figure 4.3). The diffraction patterns show more or less the typical diffraction circles. The distinction between cubic or tetragonal YSZ is impossible only by observing the diffraction patterns. Götsch

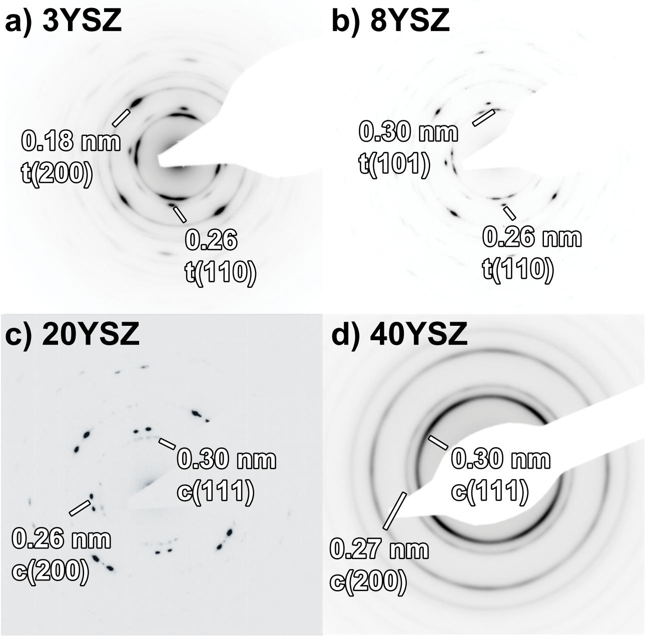

Figure 4.3: Diffraction pattern of the specimens. The letter in front of the indication refers to the structure whether it is cubic c or tetragonal t. [90]

et al. [90] simulated intensity profiles by angular integration of each diffraction pattern with the PASAD software [91]. The calculated lattice parameter c is in the range between 0.51 nm and 0.53 nm. The diffraction analysis offers a clearer idea of the structural behaviour by increasing the yttria content, which gives support in the following investigation.

Additionally, the crystallography of the samples is observed by using HRTEM. The HRTEM images offer a closer insight in the microstructure, which contain lattice fringes as shown in figure 4.4. The observation of the grains enables an attribution of the four samples to cubic or tetragonal crystal structure. At low yttria content, which includes 3YSZ and 8YSZ, a tetragonal structure can be attributed by comparing it with theoretical calculations. 20YSZ and 40YSZ exhibit a cubic crystal structure due to their higher yttria content.

The TEM investigations of the samples with different yttria content are an important part for the observation of these thin films and enable to get an overview of different YSZ compositions, which is helpful with respect to the choice of the desired ionic conductivity and at least to the desired application.

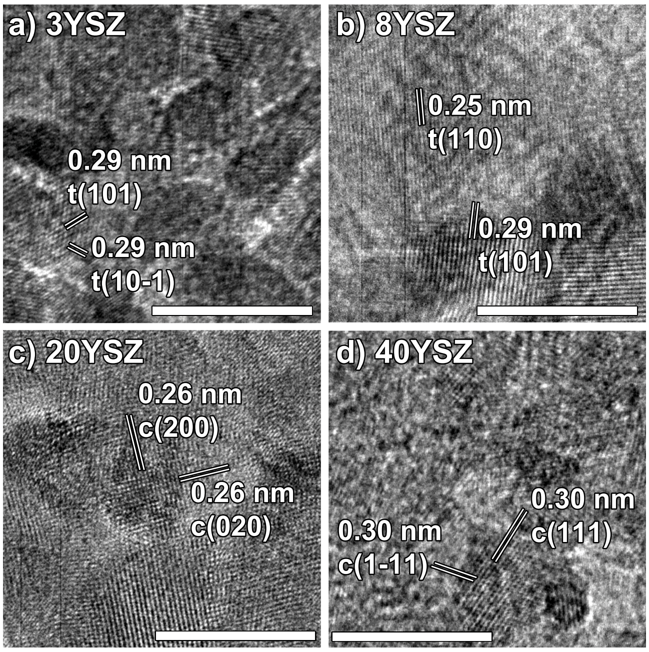

Figure 4.4: HRTEM images of the specimens containing lattice fringes with a scale bar of 10 nm. For a) 3YSZ and b) 8YSZ a tetragonal crystal structure and for c) 20YSZ and d) 40YSZ a cubic crystal structure is classified. [90]

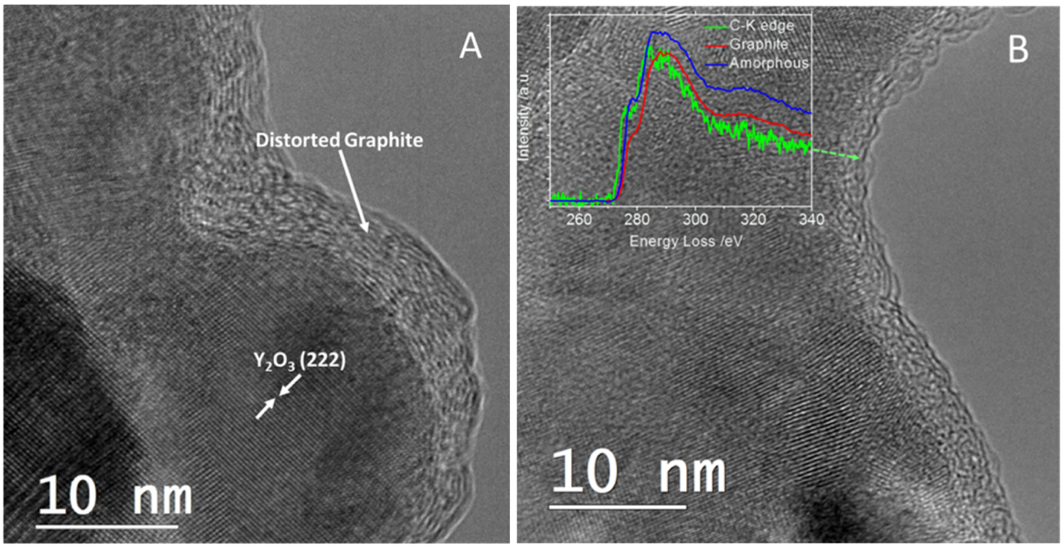

Figure 4.5: HRTEM images of Y_2O_3 grains are showing A) heavily distorted carbon graphene layers and a (222) lattice spacing of Y_2O_3 grains. B) EELS measurement along the green arrow exhibits the detected C-K edge (green), which is compared to the reference spectra of crystalline graphite (red) and amorphous carbon (blue) [92].

4.2 High-Temperature Carbon Deposition

To support the results of FT infrared spectroscopy and Raman measurements, TEM investigations were applied as additional method to analyse the microstructure and in fact the carbon behaviour. These investigations were done in collaboration with the research group of Prof. Bernhard Klötzer (Institute of Physical Chemistry, University of Innsbruck), which is published by Kogler et al. [92].

The need of more efficient energy technologies drives the research forward. A promising candidate is a solid oxide fuel cell, which produces electricity by electrochemical combination. Therefore, the aim of Kogler et al. [92] is to analyse the interaction of the reformate component carbon monoxide with Y_2O_3, YSZ and ZrO_2.

The structure of deposited carbon layers are shown in figure 4.5 and 4.6. The carbon layers of Y_2O_3 are the thickest films of about ten graphitic layers as exhibit in figure 4.5A. The Y_2O_3 grain has a lattice distance of 3.1 Å, which is consistent with the (222) orientation. The EELS measurements in figure 4.5B present the chemical nature of graphitic layers. The carbon shell has five heavily distorted graphitic

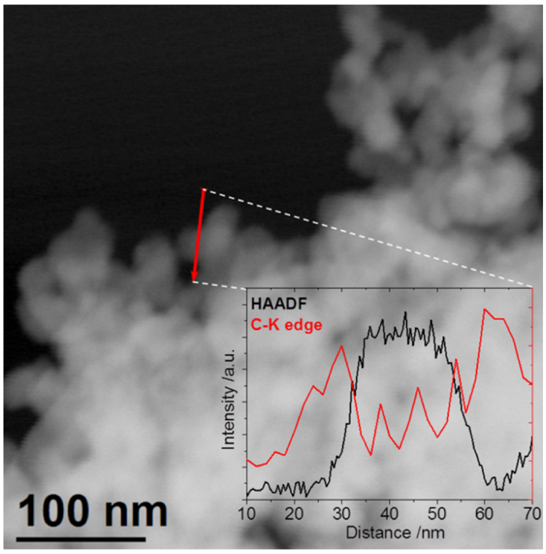

Figure 4.6: HAADF image of YSZ particles. The inset shows the EELS spectrum of the C-K edge and the total HAADF intensity measured along the red arrow. [92]

layers and the EELS spectrum exhibits inhomogeneous graphitic-like features. The inserted EELS spectra in figure 4.5B are the measured C-K edge spectrum (marked green) and the reference spectra from the literature for crystalline graphite (red) and amorphous carbon (blue).

The experiments with YSZ were done by HAADF imaging with EELS as shown in figure 4.6. The inset exhibits the EELS spectrum of the carbon K edge and the total HAADF intensity. The carbon signal is only dominant at the particle edges.

The investigations on TEM with EELS show structurally and electronically graphite-type C layers with the highest amount of deposited carbon on Y_2O_3 followed by the other materials, YSZ and ZrO_2. The TEM results are in a good agreement to additional studies of Kogler et al. [92] and confirm the structure of the carbon islands.

4.3 Metal-Support Interaction in Rhodium-Perovskite Systems

TEM investigations of archetypical rhodium-perovskite systems Rh-$La_{0.6}Sr_{0.4}FeO_{3-\delta}$

(LSF) and Rh-$SrTi_{0.7}Fe_{0.3}O_{3-\delta}$ (STF) were done to support the research group of Prof. Bernhard Klötzer (Institute of Physical Chemistry, University of Innsbruck) by the disentanglement of different manifestations of strong or reactive metal-support interactions. This collaboration is published by Thalinger et al. [93].
The rhodium-perovskite systems are characterised by the combination of TEM and EDX. Figure 4.7A2 shows a core-shell structure and as exhibited in this HRTEM image the core particle is surrounded by an amorphous shell. The lattice spacing of the particle corresponds to the value of Rh (111). An overview of the chemical composition is provided by the EDX line scan across this particle in the HAADF image (figure 4.7A3). The quantification of this line scan is shown in figure 4.7A1. Following the line scan from outside to inside the particle Fe and Rh signals are first detected. While coming closer to the centre the intensities increase and in the centre La and Sr signals are measured. Figure 4.7B shows the EDX line scan across three Rh-STF particles. The signal of Rh behaves independently from the perovskite. Fe, Sr and Ti signals possess the same increasing trend.

EELS measurement of Rh-STF confirms the reactivity of Fe as shown in figure 4.8. By means of the HRTEM and the corresponding FT, Fe_2O_3 (110) and (104) can be identified.

The study of rhodium-perovskite systems showed no classical, reversible strong metal-support interaction effects due to the missing structural and catalytic restorage capabilities of these systems. Therefore, more systematic studies of metal–support interaction effects on this material class are advisable.

4.4 Dislocations in $La_{0.8}Sr_{0.2}MnO_3$ Epitaxial Thin Films

The affection of dislocations on oxygen ion diffusion in Sr-doped $LaMnO_3$ is reported by Navickas et al. [88]. The corresponding TEM investigations are done in collaboration with the research group of Prof. Jürgen Fleig (Institute of Chemical Technologies and Analytics, Technische Universität Wien). Crucial parameters are strain and dislocations, which influence the properties of LSMO (or abbreviated LSM as in [88]) perovskite oxides and thus their applications. The LSMO thin film was deposited on two different single crystalline substrates LAO and STO. Mis-

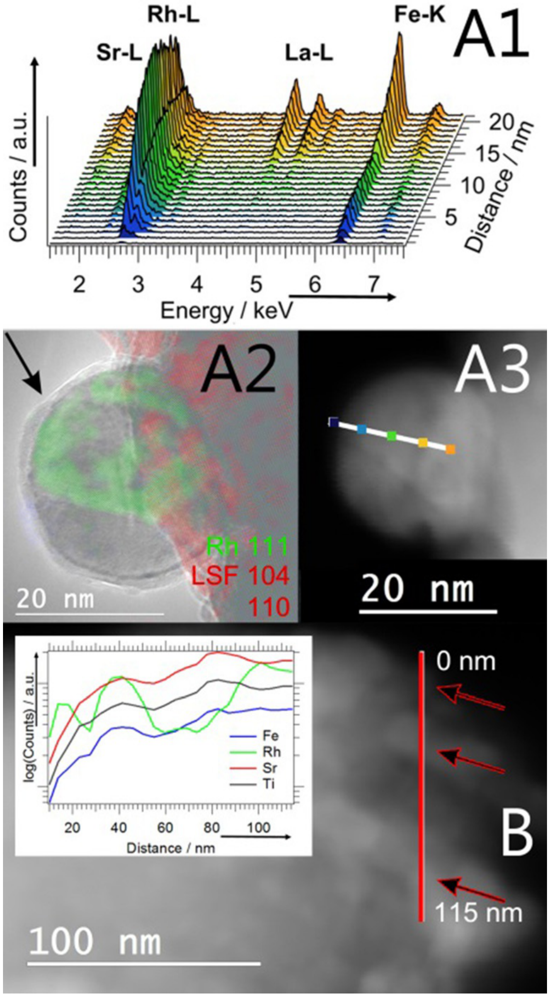

Figure 4.7: TEM and EDX investigations of A) Rh-LSF and B) Rh-STF. A2) HRTEM image shows the core-shell structure with the lattice fringes of Rh (green) and LSF (red). A3) Corresponding HAADF image with an EDX line scan, which provides A1) an overview of the chemical composition. B) The HAADF image exhibits an EDX line scan (red line) across three Rh-STF particles. The inset shows the signal of Fe, Rh, Sr and Ti. [93]

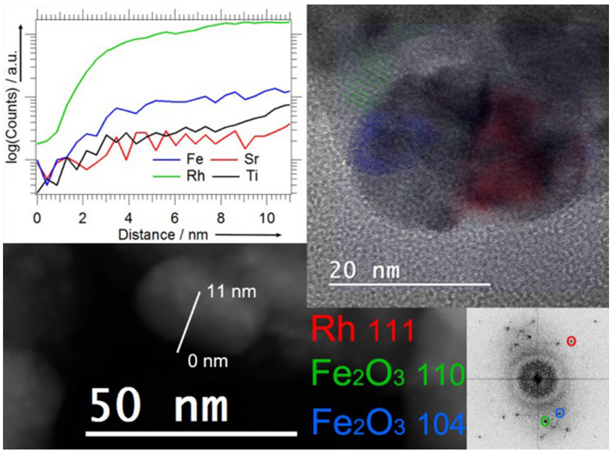

Figure 4.8: HAADF image of Rh-STF (bottom left) with an EELS line scan (top left) over a particle. HRTEM image (top right) and the corresponding FT (bottom right) identify Fe_2O_3 (110) and (104) in the perovskite. [93]

matches of the lattice between film and substrate are attributed to compressive or tensile in-plane strain in the LSMO layer.

The TEM images give an overview of the microstructure. In figure 4.9b) the DF and d) BF images show a grain-boundary free and epitaxially grown LSMO thin film layer. When the LSMO layer becomes thicker during the preparation, special microstructural features are more visible and show interesting defects, which are kind of columnar structures (figure 4.9c). These vertical structures are usually related to dislocations, which are marked with red circles in figure 4.9d). These cores of misfit dislocations are placed at the interface.

The dislocation cores are representative at the interface between LSMO and LAO, while for the sample deposited on STO no dark spotted cores exist at the interface. This impression is confirmed by the images in figure 4.10a) and d). The LSMO layer follows the substrate as shown in the HRTEM images (figure 4.10b) and d)). The behaviour of the lattice parameter c was analysed at different regions as marked in figure 4.10c and a relaxation of c was observed from interface to thin film surface.

The vertical fringes in the LSMO layer deposited on LAO shown in figure 4.11a were analysed by geometric phase analysis (GPA) [94, 95], which measures the displacement and strain fields of HRTEM images. This method is based upon centring a Gaussian mask around a Bragg reflection in the FT (see figure 4.11b) of the

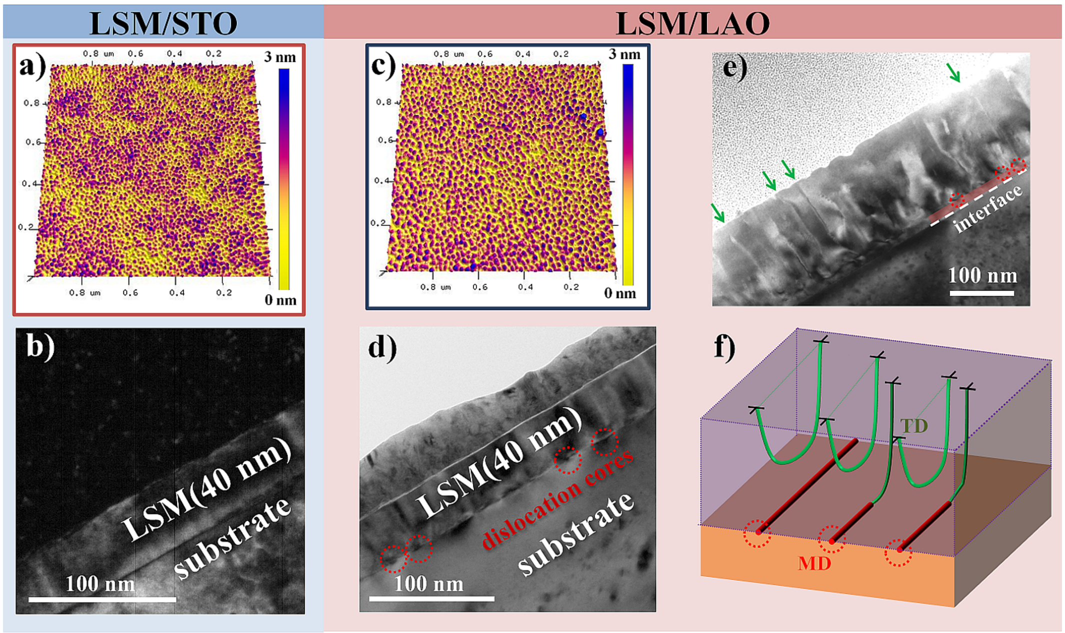

Figure 4.9: The surface topography of LSMO on different substrates a) STO and c) LAO is shown by atomic force microscope images. b) The DF image of LSMO on STO and d) the BF image of LSMO on LAO exhibit a grain boundary free LSMO layer, only interface dislocations are visible in LSMO on LAO, which are marked red. e) The BF image of a thicker LSMO layer (126 nm) on LAO substrate shows structural irregularities like threading dislocations. The red region above the interface is free of threading dislocations. f) Dislocation half-loops. [88]

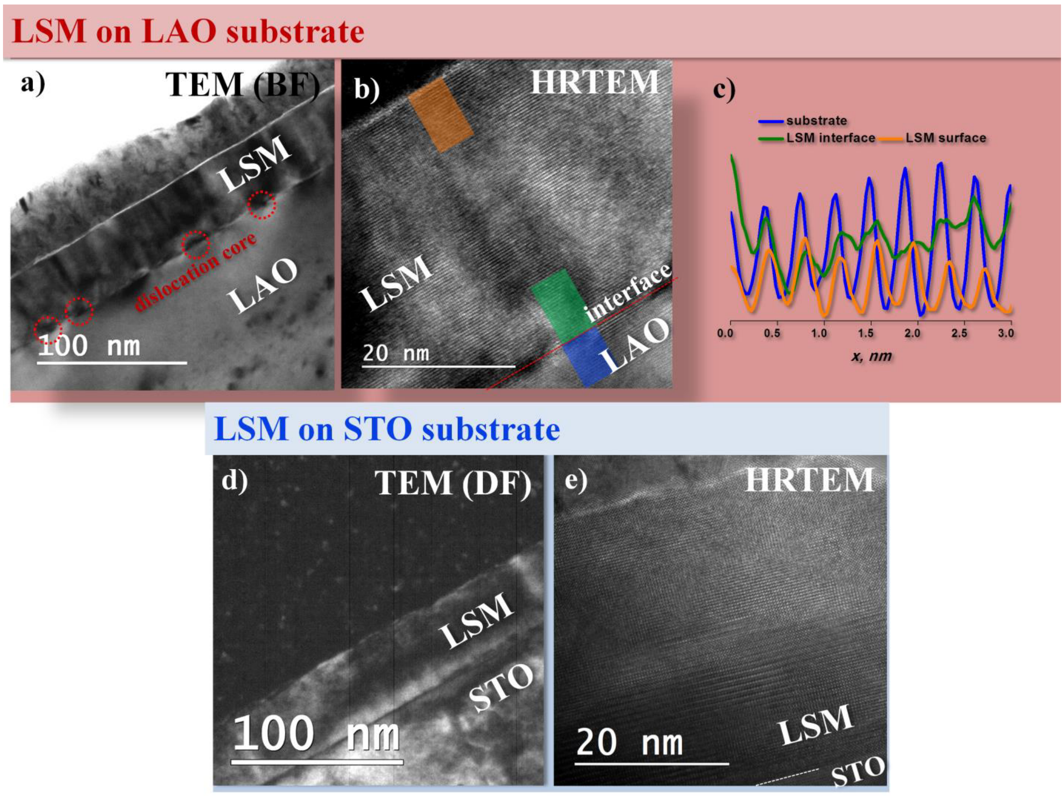

Figure 4.10: TEM investigation of LSMO on LAO and STO. a) The BF image shows dislocations at the interface. b) The atomic planes in the coloured regions are analysed and c) the graph exhibits a decrease of the lattice parameter c towards the interface. The TEM images d) and e) show epitaxially growth. [88]

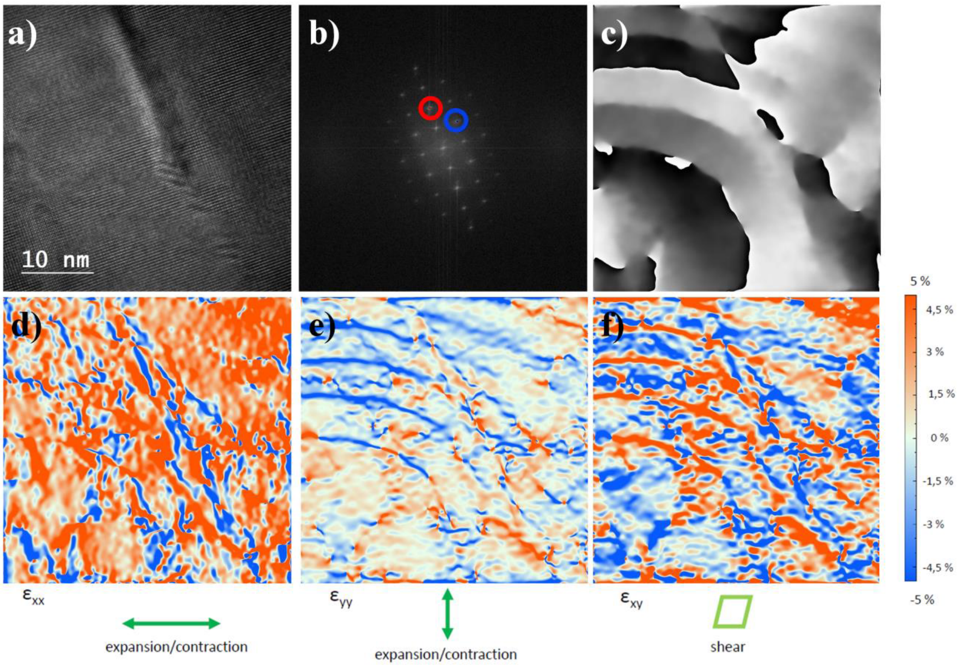

Figure 4.11: GPA of the LSMO layer on LAO. a) HRTEM image showing a typical vertical fringe. b) In the FT of the previous image two reflections are marked. c) Phase component of the red marked Bragg spot. The strain map in d) x direction ϵ_{xx}, e) y direction ϵ_{yy} and f) shear stress ϵ_{xy} are sown. [88]

HRTEM image and performing an inverse FT. The phase component of the resulting complex image gives information about local displacements of atomic planes as shown in the case of the Bragg reflection marked with the red circle in figure 4.11c. Two-dimensional displacement fields can be obtained by applying two non-colinear reciprocal lattice vectors in the FT and all variations of the lattice can be referred to it.

In principle, the strain maps are measured by using the GPA method with respect to the undistorted lattice. Since a unstrained region in the HRTEM is not known, the distortion of the lattice is measured with respect to the chosen reference lattice [95]. The phase component of the inverse FT of the red marked Bragg spot in figure 4.11c shows some irregularities of the lattice fringes and a diagonal edge from top left side to the bottom right side. It suggests to be a kind of boundary and thus like a columnar structure. The right side of the diagonal consists of mainly one phase, the left side shows several phases. The strain mapping in x direction (ϵ_{xx}) in figure 4.11d exhibits a mixing of two phases along the described diagonal in the phase image. On the left and right side of this strained region the red phase is more dominant and indicates a lattice expansion in the x direction of the image. The diagonal is also presented in the ϵ_{yy} strain map (figure 4.11e), which is perpendicular to the interface and shows the same behaviour like the phase component of the red marked Bragg reflection. Some blue phase regions bend like curves from the diagonal to the left side and suggest contractions of the lattice. The shear stress (ϵ_{xy}) confirms the impression of bending phase on the left side of the diagonal. However, there is no clear structure change as expected in the case of a columnar structure. Strain regions are observed on both sides of the vertical fringe.

The investigation of oxygen ion diffusion in epitaxial grown thin film layers like LSMO on single crystalline LAO and STO substrates shows strain, which relax with an increase of the layer thickness. Dislocations affect the oxygen ion transport and the surface exchange kinetics and thus they could be important by influencing the kinetic properties.

Chapter 5

Low Losses

This chapter describes the experimental investigation of the low losses in EELS and its interpretation by means of numerical simulations.

5.1 Crucial Requirements

The CMR effect induces a strong change in resistivity and magnetisation of the specimen, which are affected by temperature and external magnetic field. Therefore, it is expected that the consequences of the CMR effect have some significant impacts on the electronic properties, inter alia, on the joint density of states (JDOS), which is not easy to interpret. The behaviour of the specimen and thus indirectly the CMR effect is studied during the VEELS experiments under certain conditions by varying the temperature and the magnetic field in TEM. The temperature change is achieved by using a cryo-transfer holder, which cools the sample with liquid nitrogen to 85 K.

The more complex issue is to apply and change the magnetic field inside the TEM. In TEM magnetic lenses are used instead of optical lenses. The specimen is placed inside the objective lens system, which means it is surrounded by pole pieces and the resulting magnetic field of the objective lens affects the specimen. The change of the TEM operating voltage influences the alignment of the lens system and thus the magnetic field of the objective lens. Several approaches can be chosen to determine the objective lens magnetic field, e.g. by inserting a Hall sensor into the objective lens pole piece [96]. For the VEELS experiments the strength of the objective lens field was approximated by using the approach of Schachinger et al. [97], where the

Larmor rotation in the magnetic lens field can be detected due to electron optics:

$$\dot{\phi} = \frac{e}{2m} \cdot B_z \tag{5.1}$$

where $\dot{\phi}$ is the angular velocity defined by the axial component of the magnetic field strength B_z. The equation 5.1 is also known as the Larmor precision. After further consideration of Glaser [98], who included the high tension, the image rotation is achieved by

$$\phi(z) = \sqrt{\frac{e}{8mU}} \int_{z_0}^{z_1} B_z(z) dz \tag{5.2}$$

For the investigations of Schachinger et al. [97] the same microscope was used and based on this knowledge, a magnetic lens field strength of 1.9 T at a high tension of 200 kV was determined. For this study the magnetic field of the objective lens at 40 kV was approximated by the following assumption under consideration that the specimen is in the eucentric height:

$$M_{40kV} = \frac{M_{200kV}}{\sqrt[2]{\frac{200}{40}}} \tag{5.3}$$

The strength of the objective lens field is changing from 1.9 T to 0.9 T, when the beam energy decreases from 200 keV to 40 keV. In this case the CMR effect induces a change of the electronic properties, which results in an increase of the bandgap width (section 2.1) and a reduction of the conductivity as reported in [10, 15]. The behaviour of the CMR effect is strongly connected to the investigation temperature [9, 10, 15] and in particular above and below $\mathrm{T_C}$ of 210 K. Hence, two temperatures, 85 K and RT, were chosen for the VEELS measurements. The reason behind this decision was that the microscope is operating very stable at RT, which is the normal working condition in TEM. On the other hand 85 K was chosen because it is the lowest reachable temperature of the cryo-transfer holder due to the fact that liquid nitrogen is used. Therefore, 85 K is also a very stable working condition for this cryo holder.

The low loss spectrum in EELS contains information about the dielectric properties of the specimen. An accurate investigation of the bandgap depends on the EELS spectrum and its influencing factors like relativistic losses. However, the removal of the ZLP is essential to avoid the tails of this elastic peak in the bandgap signal

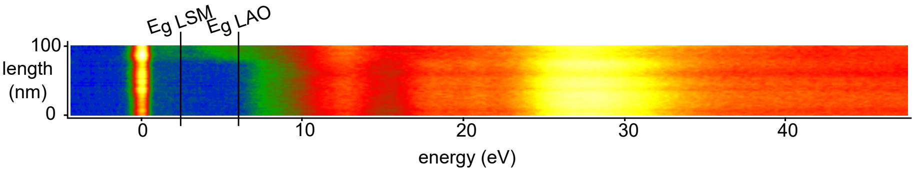

Figure 5.1: Intensity map of VEELS spectra recorded across the LSM100/LAO interface without Čerenkov losses measured at 40 keV. The bandgap energies are marked for LSMO and LAO.

[21]. The tail of the elastic peak, which is affected by relativistic effects, typically covers the bandgap and interband transition signal. The alteration of the beam energy causes not only a change of the magnetic field: Lowering the speed of the probe electrons prevents knock-on damage of LSMO and LCMO, and avoids the excitation of the Čerenkov losses, which influences the shape of the very low loss part of the EELS spectrum. The Čerenkov losses arise by charged particles losing energy by emitting radiation when passing through a medium with a speed being faster than light inside the medium. The refractive index of the probed material defines the Čerenkov limit [99]:

$$v_e \geq \frac{c_0}{n} \tag{5.4}$$

where v_e describes the speed of the electron, c_0 is the vacuum speed of light and n is the refractive index of the medium. The refractive index of LSMO is 2.73 according to [100]. The LCMO refractive index of 2.40 was calculated by means of KKA on a measured VEELS spectrum at 40 keV. The resulting Čerenkov limits for both materials are approximately 38 keV for LSMO and 50 keV for LCMO, respectively. This contribution to the bandgap signal is not negligible and there are two possibilities in order to circumvent the influences of the Čerenkov effect: probing an extremely thin sample area [101] or reducing the beam energy [22].

5.2 VEELS Observations

The accomplished VEELS measurements were investigated at thin regions of the TEM lamella, which finally had a thickness of lower than 30 nm. In order to observe the behaviour of the properties with and without Čerenkov losses, a low operating voltage of 40 kV was also chosen beside the common operating voltage of

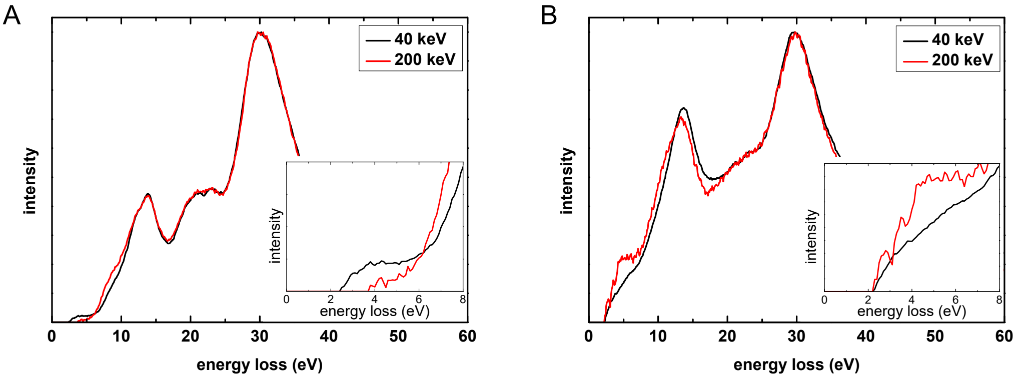

Figure 5.2: VEELS spectra of A) LAO and B) LSMO at two different beam energies (40 keV and 200 keV) after ZLP removal by a pre-measured elastic peak. The inset of the LAO experiments shows some artefacts from 2 eV to 5 eV and in the range between 5 eV and 7 eV there is a steep intensity increase. The inset of the LSMO experiments shows an increase of intensity at around 2 eV.

200 kV. Figure 5.1 shows a low loss spectrum image of the LSM100/LAO interface measured at 40 keV in STEM mode, which exhibits a bandgap transition from the LAO substrate to the LSMO layer. A steep interface transition is detected for both materials from the LAO bandgap ∼6 eV [102, 103] to the LSMO bandgap ∼1.95 eV [100]. After the ZLP removal the VEELS spectra of LAO and LSMO in figure 5.2 show that Čerenkov contribution is nearly vanished at 40 keV beam energy, whereas these losses are observed at 200 keV. The removal was done by acquiring separately a vacuum ZLP under the same conditions and subtracting it from the spectrum. The difficulty of this solution is that the ZLP of the spectrum gets broaden by the specimen and does not reach the height of the vacuum ZLP. This suggests that the vacuum ZLP is narrower and higher than the ZLP of the spectrum due to less losses, however, the shape of both elastic peaks is similar and this leads to a sufficient good result for the determination of the bandgap signal. However, some artefacts in the bandgap region can be seen in the insertion in figure 5.2A and highlights the importance of ZLP removal as mentioned before. Both spectra measured at an acceleration voltage of 200 kV exhibit additional intensity in the very low loss range caused by the Čerenkov effect.

Even small changes of the high tension above the Čerenkov limit from 60 kV to 80 kV have an influence on the intensity in the VEELS spectrum as shown in

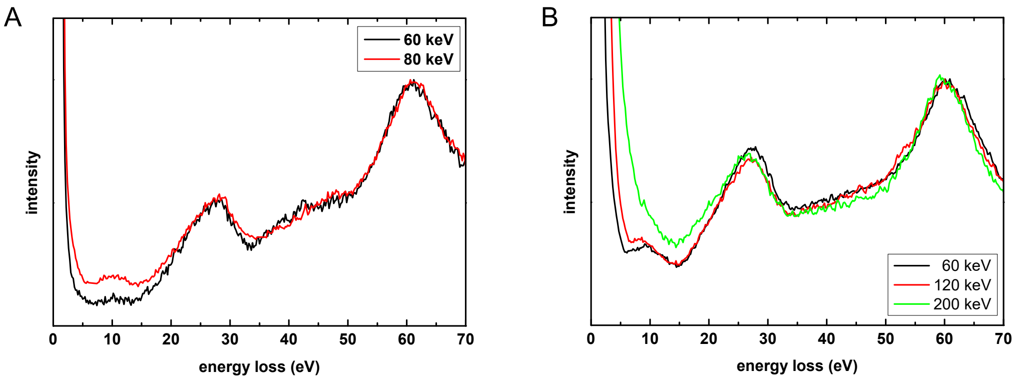

Figure 5.3: A) VEELS spectra at 60 kV and 80 kV high tension confirm the different behaviour of bandgap signal at higher beam energies considering the attendance of Čerenkov radiation. B) LSMO spectra at different beam energies integrated over the inelastic part showing the resulting shape of ZLP tails.

figure 5.3A. The spectra at different beam energies should conscientiously be compared due to the relation of elastically and inelastically scattered part of the low loss spectrum, and the shape of the ZLP. Figure 5.3B gives an insight in the complexity of the bandgap distinction. All spectra were integrated over the inelastic part, which show the same shape excluding the tails of the ZLP. As expected, the reduction of the beam energy causes a change of intensity in the energy range from approximately 2 eV to 10 eV and presents a new shape of the spectrum at 60 kV, 80 kV and 120 kV high tension compared to the spectrum measured at 200 kV.

The experiments with LCM100/STO at different beam energies and temperatures show an interesting behaviour (figure 5.4). In figure 5.4B the low loss spectra at 40 keV and 200 keV are recorded at RT and no difference of the spectra can be seen in this graph. In this case, the bandgap was not detected at RT due to the small bandgap width of LCMO (1.6 eV) as reported by Ullah et al. [16]. Hence, the shape of the ZLP covers the bandgap. Figure 5.4A presents the spectra with the same beam energies measured at 85 K and exhibit a variation in the bandgap region. This intensity variation in the very low loss part of the VEELS spectrum at 85 K is between 1.5 eV and 4 eV. The shift can be caused by to different reasons: One of them is the contribution of Čerenkov losses in the 200 keV spectrum because of the additional intensity which changes the original spectrum. The other reason can be the CMR effect, which narrows the bandgap on account of increasing the magnetic

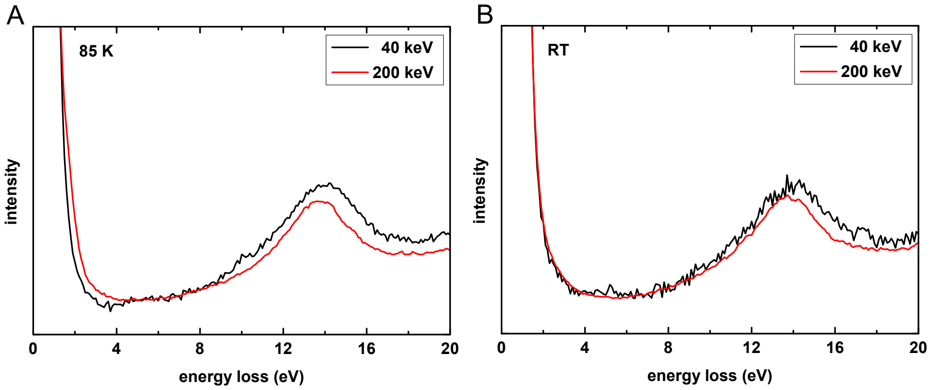

Figure 5.4: Low loss spectra of LCM100/STO recorded with two beam energies, 40 keV and 200 keV, at A) 85 K and B) RT. [27]

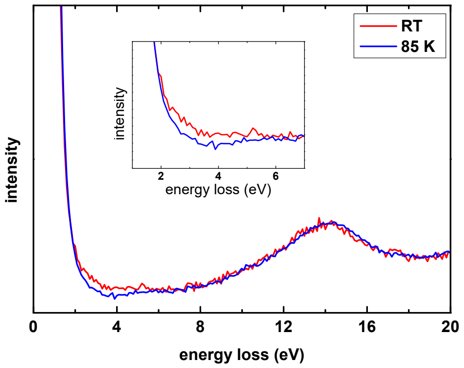

Figure 5.5: VEELS measurements of LCM100/STO at 40 keV beam energy acquired at 85 K and RT showing an intensity variation in the bandgap region. The insertion presents a magnified view. [27]

field in the objective lens system. As mentioned before, an increase of the magnetic field is achieved by increasing the accelerating voltage.

In consideration of these various aspects, which can influence the VEELS spectra, the measurements of LCM100/STO below the Čerenkov limit were compared. Figure 5.5 shows the experiments at 40 keV by only changing the temperature and exhibits a variation of the spectra in the bandgap region. The presented intensity difference in the low loss region is induced by the CMR effect due to the reason that the experiments were done below the Čerenkov limit. This LCMO behaviour is reported by Mahato et al. [10], where the CMR effect is becoming stronger by applying a magnetic field and reducing the temperature as presented in figure 1.1.

A completely different type of sample compared to the previous two is LCM80/LAO.

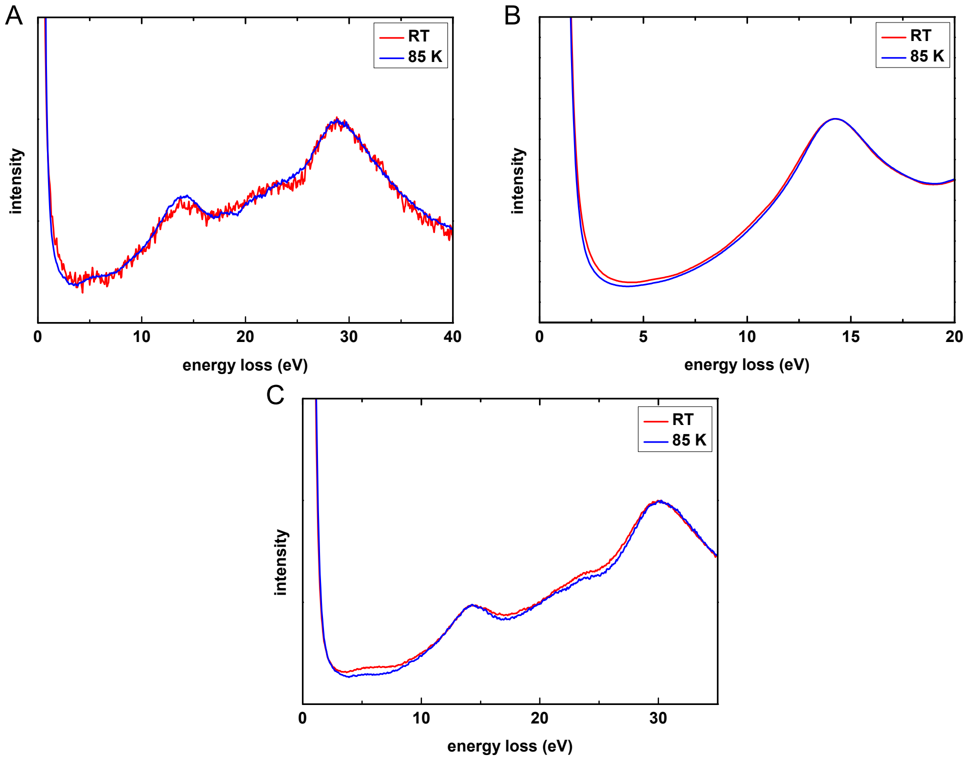

Figure 5.6: VEELS measurements of LCM80/LAO at different temperatures. A) EELS spectra recorded at 20 kV beam energy showing a slight difference of the intensity by comparing 85 K and RT. B) A difference of the investigated spectra at 40 keV is presented after one iteration of the RL algorithm. C) Measurements at 85 K and RT on another grain exhibit an intensity variation starting at different eV compared to other results.

It is a polycrystalline sample with non-homogeneously distribution of the layer due to the high pressure during the synthesis of the specimen. Single grains in this layer (see section 3.1.1) are expected to have a slightly different composition and orientation. It cannot be assumed that all grains show the same effect due to the strong induced strain in this layer. Cesaria et al. [104] reported that the pressure during the synthesis has a main influence on the material properties.

A change of the pressure during the sample synthesis results in different intensity variations in the bandgap region as shown in figures 5.6. Comparing figure 5.6A and C, the intensity variation arises at different energies. Also a change to lower high tension like 20 kV (figure 5.6A) compared to 40 kV (figure 5.6B) exhibits no

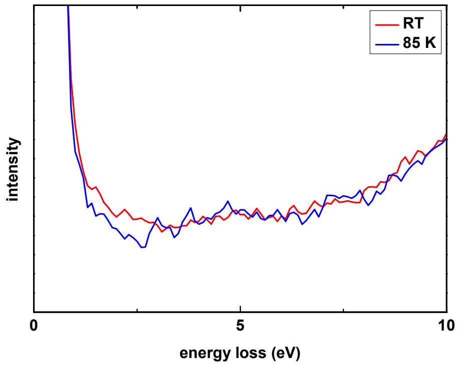

Figure 5.7: Low loss spectrum of LCM300/Si showing a intensity divergence between the measurement at 85 K and RT.

stronger influence of intensity difference. In addition, the strength of the difference is depending on the sensitivity of the composition and the induced strain. The spectra in figure 5.6B were deconvolved by RL and stopped after one iteration. The usage of RL was done to deconvolve the FWHM of the ZLP. The variation of the spectra in the low loss region is clearly visible.

The investigation of the sample LCM300/Si at 40 keV beam energy presents a intensity divergence in the bandgap region as shown in figure 5.7. The signal-to-noise ratio is not satisfying. LCM300/Si has a different nanostructure and clearly shows columnar defects very dense packed as shown in figure 3.12, which leads to a non-homogeneous crystallographic orientation and makes it difficult to investigate this layer.

The energy resolution was improved by using a monochromated TEM at CEITEC. Two samples, LCM80/LAO and LCM300/Si, were analysed again at 60 kV. In figure 5.8 the VEELS investigations of specimen LCM300/Si are shown. The measurements were done at various layer positions and exhibit the sensitive influence of strain on material properties. The VEELS experiments compared at different temperatures give an intensity variation from 1 eV to 5 eV (figure 5.8A).

Due to the polycrystalline layer structure sample LCM80/LAO is interesting to observe by monochromated TEM. Figure 5.9A shows the small spread of the ZLP and the bandgap region, where an intensity variation by comparing measurements at different temperatures is detected. In figure 5.9B the bandgap region is presented with a finer energy scale. The distinction of intensity starts at 1 eV and ends at

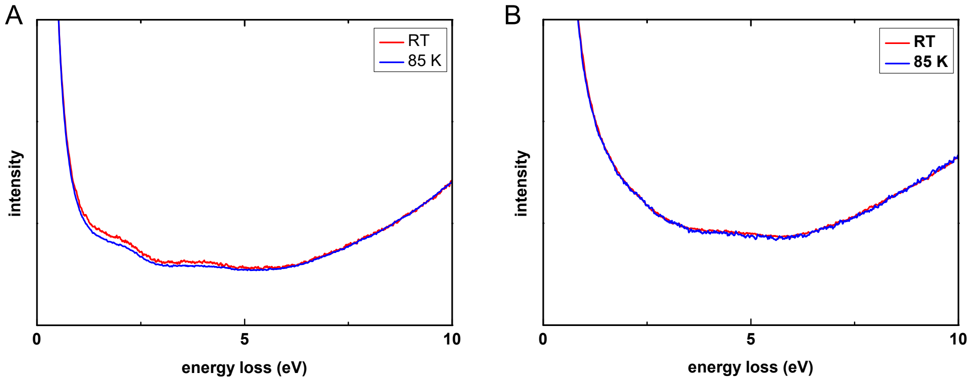

Figure 5.8: LCM300/Si was investigated with a high tension of 60 keV at different layer positions by using a monochromated TEM. A) A small intensity variation is presented in the low loss part. B) Close to the previous position no difference in bandgap region was measured.

5 eV, which is similar to the specimen LCM300/Si. By investigating a different grain the behaviour of VEELS spectra in the bandgap region is changed and exhibits in figure 5.9C a shift of the intensity variation form 3 eV to 5 eV.

The removal of the ZLP for a direct observation of the bandgap is a delicate venture because of the shape of the elastic peak tail [21] as mentioned in the section 5.1. Hence, an improvement of the bandgap signal was determined by the subtraction of a pre-measured vacuum ZLP or by using a monochromator. Another possibility to determine a change in the bandgap region is to observe the interband transitions. The change of the bandgap width induces a shift of the conduction band and therefore, the energy of the interband transitions is altered. On this account, the RL algorithm [71] was used to improve the energy resolution in the spectrum. For the investigation of the interband transitions the LCM100/STO spectra at 40 keV were processed by the RL algorithm and aborted after five iterations (figure 5.10). The features of the interband transitions are more detailed. In order to achieve a better determination of the interband transition position, a non-linear least square Gaussian fit routine was used.

An improvement of the spectrometer dispersion of around 50 percentage was achieved by the post-data treatment with the Gaussian fit routine and the accuracy of the energy resolution was increased to lower than 0.5 channels. The fitting range was moved over several channels of the spectrum [27]. The results are listed in table 5.1.

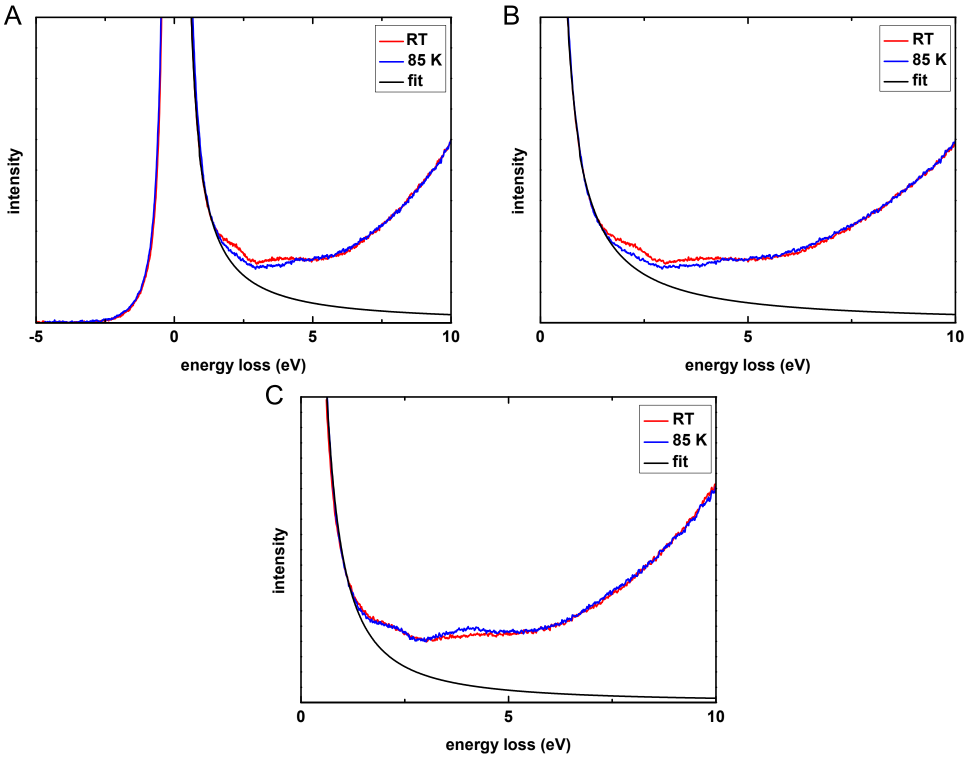

Figure 5.9: VEELS investigation of LCM80/LAO at 60 keV. A) Low loss region exhibits an intensity variation, B) which is shown with a finer energy scale. C) Shift of the intensity distinction is detected on another grain.

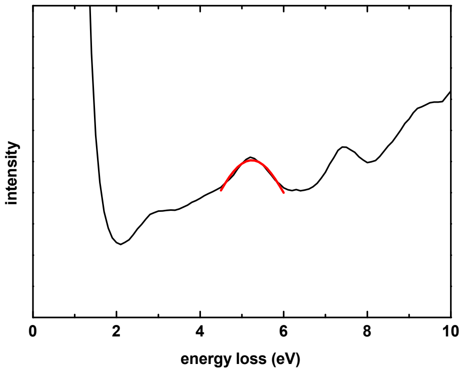

Figure 5.10: VEELS spectrum of LCM100/STO at 40 keV and RT sharpened by RL algorithm. The red curve represents the Gaussian fit routine for determining the position of the interband transition. [27]

Table 5.1: The accurate interband transition positions of LCMO measured at 40 keV and 200 keV for two temperatures, 85 K and RT, and the value of the resulting bandgap shift ΔE.

E_0	85 K	RT	ΔE
200 keV	4.92 eV	4.88 eV	0.04 eV
40 keV	5.38 eV	5.24 eV	0.14 eV

The values of table 5.1 verify the expected behaviour from the literature, which means that the change of the magnetic field to higher values narrows the bandgap. Hence, the Čerenkov effect has to be taken into account while comparing spectra at different energy beams. However, when the temperature is increasing, the bandgap is decreasing. Considering the measurements at 40 keV, there is an interband transition at 5.38 eV ± 0.05 eV of standard deviation at 85 K and at RT the position is shifted to 5.24 eV ± 0.01 eV. A bandgap variation ΔE of 0.14 eV was detected by changing the temperature from 85 K to RT and applying a constant external magnetic field of 0.9 T [27].

5.3 Ellipsometry Data

In addition to the VEELS experiments, the ellipsometer measurements of sample LCM300/Si were done to compare them with the very low loss region of the EELS spectrum. The optical properties of specimen are described by two measured values, the refractive index n and the extinction coefficient κ, and both are related to the complex refractive index n_c (see equation 2.47). Alternatively, the measured data from ellipsometry can be expressed by using equation 2.46 as complex dielectric function. Complex refractive index and complex dielectric function are closely related and can be easily converted into each other (see section 2.2).

The raw data from the ellipsometer measurements at RT are presented in figure 5.11A. From the increase of the extinction coefficient the size of the bandgap is derived, which is approximately around 1.6 eV. This impression is in good accordance to the knowledge from literature [16].

Figure 5.11B shows the behaviour of the loss function by means of the non-relativistic description of inelastic energy loss based on the complex dielectric func-

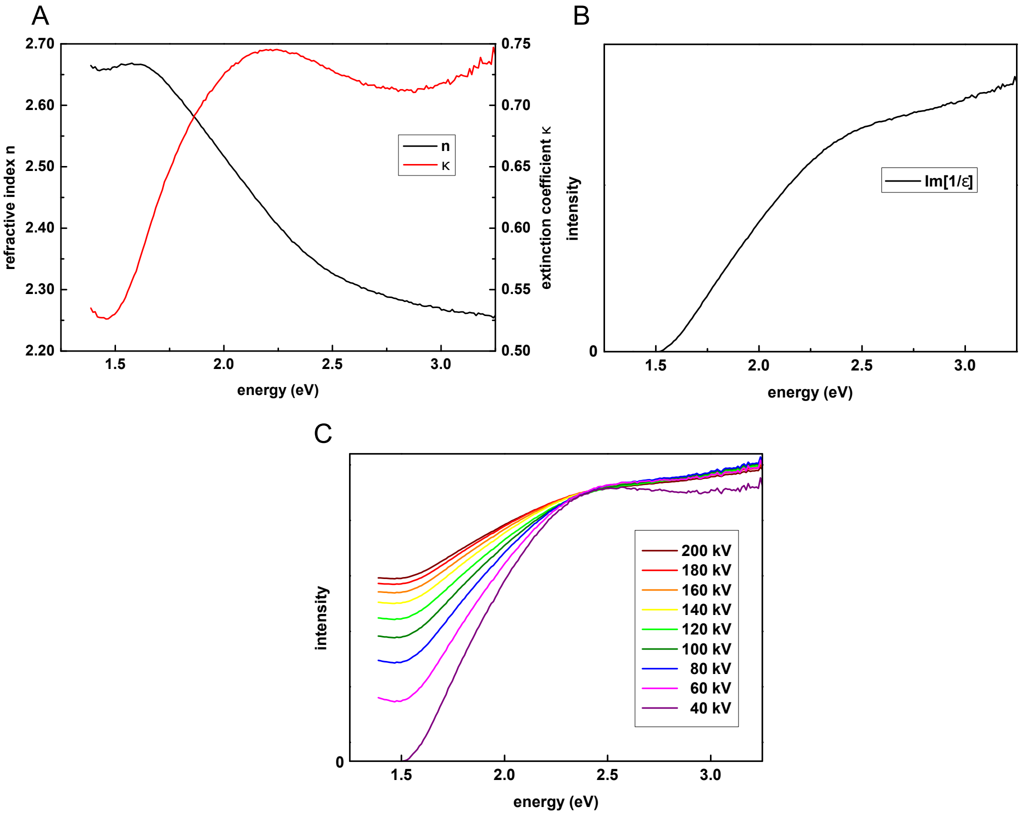

Figure 5.11: Ellipsometry data of LCM300/Si over the energy loss showing A) the raw data, B) the loss function $\Im[1/\epsilon]$ and C) the calculated VEELS spectra with $\beta = 2.8$ mrad at various high tensions.

tion:

$$\Im\left[\frac{1}{\epsilon}\right] = \frac{\epsilon_2}{\epsilon_1^2 + \epsilon_2^2} \tag{5.5}$$

The relativistic energy loss (figure 5.11C) was calculated by using the Kröger equation (see equation 2.48) for a normal incident beam ($\alpha = 0$). For the theoretical observation of the VEELS spectrum a constant sample thickness of 40 nm was assumed, the collection angle β was 2.8 mrad and the operation voltage has been changed in the range between 40 kV and 200 kV. The graph in figure 5.11C shows the ratio of intensity gradient, which gives information about the consequences of relativistic effects. Hence, an increase of intensity in the low loss region is shown by increasing the high tension.

Due to the theoretical observations the alteration of the VEELS spectrum for the case when the speed of the probed electron is faster than light inside the medium is ascribed to the Čerenkov losses. Hence, the accurate determination of the optical and electronic properties by using EELS leads to a solvable task concerning the correct beam energy and sample thickness as shown within the previous sections.

5.4 Numerical Simulations

The complexity of the CMR effect necessitates a theoretical observation. The behaviour of electrons in a periodic potential like a crystal can be described by DFT (see section 2.3) and give a microscopic comprehension of solids. Ab initio quantum mechanical calculations are a great support in the interpretation of the electronic structure and the corresponding material properties in energy loss spectrometry [105].

EELS is related to optical, electronic and magnetic material properties. Two ab initio methods for EELS are based on multiple scattering [106] and bandstructure calculations [107]. Bandstructure methods enable a coherent interpretation of the crystal by providing density of states, bandstructure diagrams, optical properties and EELS spectra. These methods are based on the Hohenberg-Kohn-Sham theorem [65, 66]. The DFT calculations are carried out using the WIEN2k code [67], a full potential, linearised augmented plane wave DFT method.

The crystal structure of LCMO for the ab initio calculations is built based on the monoclinic P2_1/n space group [108] and is shown in figure 5.12. The special char-

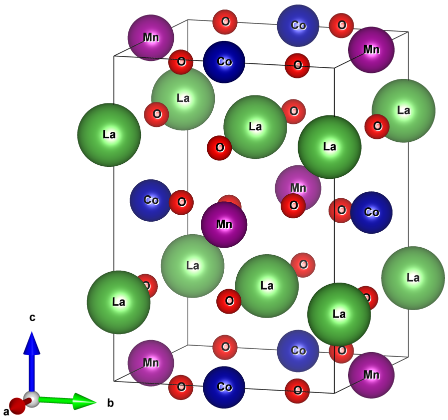

Figure 5.12: LCMO crystal structure with a monoclinic space group P2_1/n. The elements of the LCMO compound are marked with the following colour: La is green, Co is blue, Mn is violet and O is red.

acteristic of this double perovskite structure is that Co and Mn occupy a separate atomic position in the crystal. Normally, these two elements, Co and Mn, share the same atomic position and are the B-site cations in the ABO_3 compound with a certain occupancy. In this case, a supercell [17] has to be created to solve the distribution of Co/Mn occupancy in the unit cell. The disadvantage of the supercell is the enormous computation time. Hence, to save computation time and due to literature study [109–111], the LCMO crystal structure was chosen for the DFT calculations as reported by Bull et al. [108]. In this case, Co and Mn have two different atomic positions, which leads to a simplification where the calculations are done only by the size of one unit cell.

A WIEN2k calculation consists of the initialisation and the self-consistent field (SCF) calculation. In the phase of initialisation all inputs for the SCF calculation are created and the initial electron density is calculated. The original formulation of DFT does not include spin-polarisation. Co and Mn are magnetic metals and La is also expected to show a weak spin-magnetisation, especially at 0 K. To account for the existence of the spin moments and to obtain correct energy values in compounds with magnetic order, the calculations were carried out scalar relativistically. Such a calculation divides the density in spin-up and spin-down, with a Kohn-Sham equation (equation 2.65) for each spin-density. In collinear magnetic structures, like LCMO, spin-up and spin-down densities remain uncoupled. The final electron den-

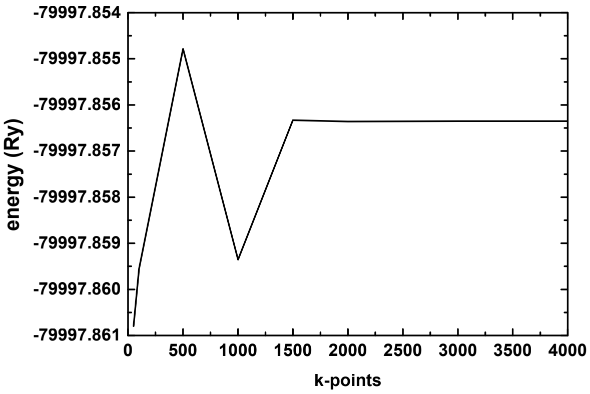

Figure 5.13: k-point convergence of LCMO with the FM configuration. The k-points are increased from 50 to 4000.

sity and thus the potential is calculated in the SCF phase to solve the Schrödinger equation (equation 2.62), which describes the electronic wave function to determine the electron density again. The SCF cycle is repeated, until a specific convergence criterion is reached.

The general gradient approximation (GGA) formulation of Perdew, Burke and Ernzerhof [112] was used for the WIEN2k calculations. The determination of total energy shows that both, the ferromagnetic (FM) state and ferrimagnetic (FiM) state with La spin-down and Co, Mn spin-up, reach the lowest energy. The FM configuration achieves the lowest ground state as reported by literature [109, 110]. Hence, for the following calculation the FM state was used.

The convergence criterion for the SCF cycle was 10^{-6} Ry. Figure 5.13 exhibits the k-point convergence, which was determined by increasing the k-points from 50 to 4000 and no change of the energy could be observed from 2000 to 4000 k-points. Therefore, 2000 k-points were chosen for the simulations. Considering the electronic correlation effects the effective Hubbard parameter $U_{eff} = U - J$ with $J = 0$ was used. The GGA+U calculations were done with a U value of 3 eV for Co and Mn 3d orbitals, which is recommended by the literature [17, 109, 110].

After the convergence of the SCF calculations, several material properties inter alia the DOS can be determined. The total DOS plots with GGA and GGA+U for FM LCMO are shown in figure 5.14. In both cases the material is spin-polarised and shows magnetic behaviour in a way that the areas of the spin-up and spin-down states are not identical. The calculations indicate that LCMO is a FM half-

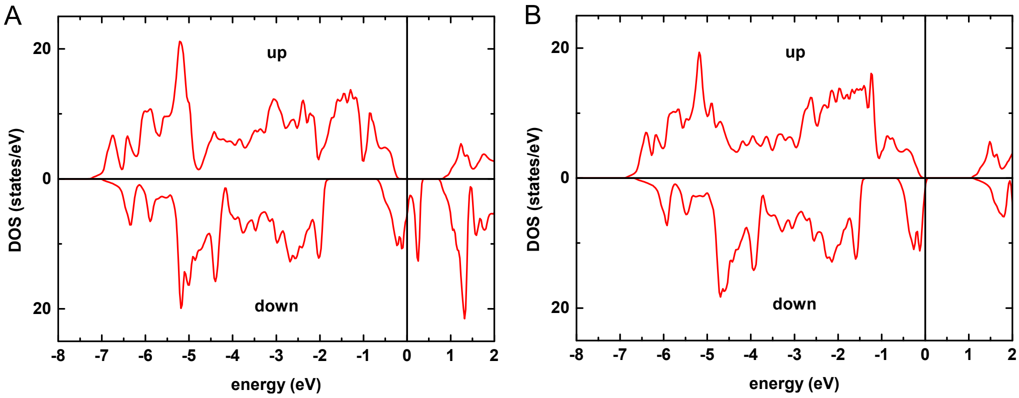

Figure 5.14: Total DOS plots of LCMO calculated using A) GGA and B) GGA+U methods. Both cases, spin-up and spin-down, are spin-polarised due to the different shape of the spin state and shows magnetic behaviour.

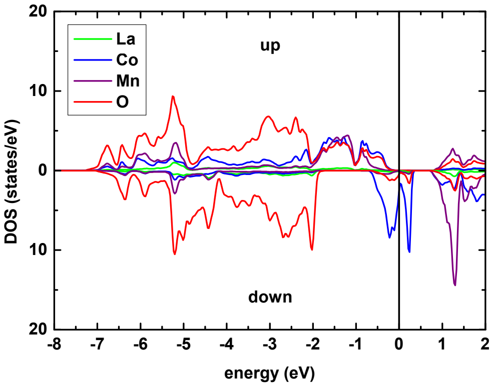

Figure 5.15: The DOS plot of La, Co, Mn and O is calculated by using GGA method and shows the spin-up and spin-down states, which exhibit the spin-polarisation of LCMO.

metal, which shows no insulator gap in figure 5.14A. GGA+U allows a bandgap development (see figure 5.14B) and thus, LCMO is a FM semiconductor. Figure 5.15 offers a closer look to the DOS of the included elements and shows that the O-2p states are mainly below -3 eV, the Co and Mn 3d states are in the range from -3 eV to 2 eV and La is more or less not represented in the range of this DOS plot.

The calculation of low loss EELS spectra by using DFT is very well known and in a good agreement to the experimental spectra [113]. WIEN2k offers the possibility to determine the VEELS spectrum by calculating the optical properties using the package OPTIC developed by Ambrosch-Draxl and Sofo [114]. The first step to

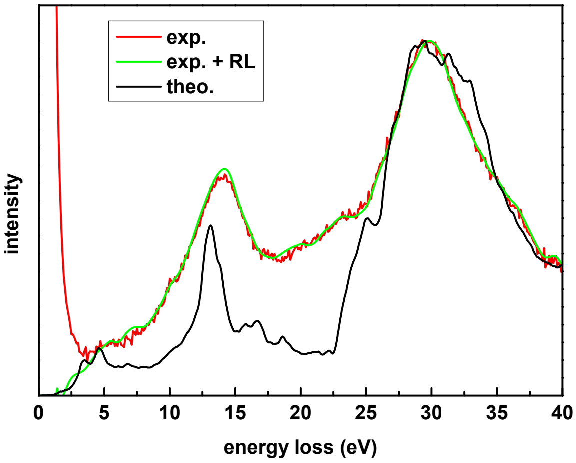

Figure 5.16: Comparison of experimental and theoretical VEELS spectra of LCMO. The red spectrum is detected at 40 keV and 85 K. This measurement is processed by RL algorithm and the ZLP was removed by power law tail approximation (green). The theoretical VEELS (black) spectrum is calculated by WIEN2k with the package OPTIC.

run the SCF cycle was already done for the previous DOS plots with a mesh of 2000 k-points. The next step is the dielectric function calculation by following the routine of OPTIC. One of the crucial conditions is the k-point mesh. The number of k-points defines the reciprocal space sampling and has to span a fine mesh in a way that all interband transitions are considered as reported from Keast [105]. Keast showed that the theoretical VEELS spectrum is very sensitive to the number of k-points and in case of Au at a number of 5000 k-points the low loss region was not changing. Hence, the k-points are increased to 5000 by running the program kgen at the beginning of the OPTIC routine.

The resulting calculated VEELS spectrum in figure 5.16 is in a good agreement with the experiment. It shows similar features, especially at approximately 5 eV. This peak corresponds to the measured data presented in figure 5.10. In both cases an interband transition is shown at an energy loss of 5 eV.

Chapter 6

Core Losses

This chapter summarises the magnetic behaviour observations of LCMO using energy loss spectrometry. It provides an insight into element specific magnetisation of LCMO with respect to different temperatures.

6.1 EMCD Results

The magnetic behaviour of the double perovskite LCMO is analysed by temperature dependent EMCD measurements. Several investigations [8–10] reported that the temperature affects the magnetic behaviour of the material in macroscopic observations and thus there is an influence on the consequences of the CMR effect. As described in section 3.1.2, the EMCD technique of EELS gives an access to the magnetisation in smaller scale.

Compared to the previous low loss investigations, a variation of the external magnetic field in the range from 1.9 T (200 keV beam energy) to 0.9 T (40 keV beam energy) does not show a significant distinction on the EMCD signal. In both cases, the magnetic moments are saturated and aligned with respect to the objective lens magnetic field. The coercive field of LCMO at 10 K is $\sim$0.6 T and at RT almost zero as reported by Mahato et al. [10]. Hence, the literature declares that the highest possible coercive field of 0.6 T is achieved at 10 K and is decreasing with an increase of temperature. Consequently, in both temperature dependent EMCD experiments, at 85 K and at RT, the coercive field is smaller then 0.9 T and therefore, it does not matter which external magnetic field is applied in TEM. The standard working condition of the microscope is at 200 kV high tension, which makes the measuring

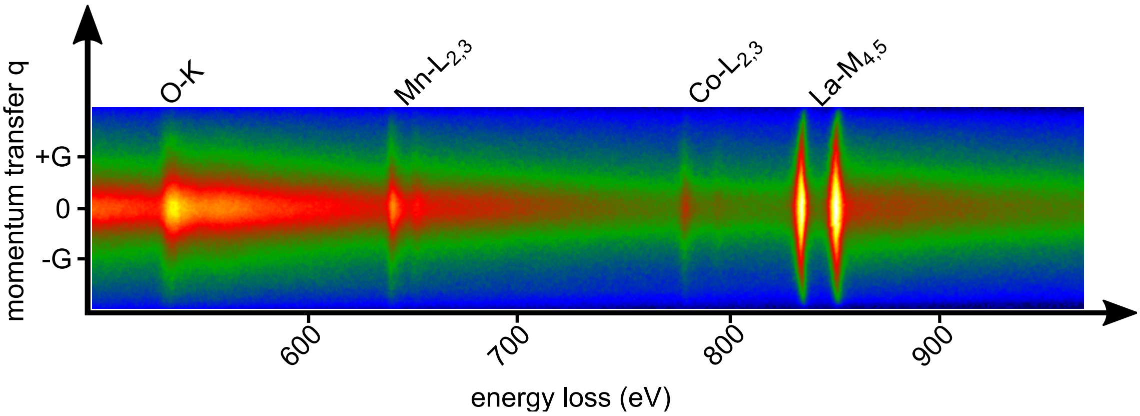

Figure 6.1: $\Delta E - q$ map of LCMO measured at 85 K showing the O-K edge, the Mn-$L_{2,3}$ edges, the Co-$L_{2,3}$ edges and the La-$M_{4,5}$ edges. [27]

conditions very stable. In addition, the beam intensity is very low in EMCD due to the specific off-axis orientation, which means that the intensity is satisfactory when the beam energy is high, e.g. 200 keV.

According to the Čerenkov theory it is known that there is an intensity contribution to the EELS spectrum when the beam energy is above a certain limit, the Čerenkov limit (see equation 5.4 in chapter 5). However, the Čerenkov effect plays no role for EMCD. This statement is comprehensible by comparing the low loss region with the core loss region and by having figure 3.1 in mind. The intensities in these two regions are completely different. The influence of the Čerenkov contribution can not be measured due to the plural scattering, which means that the noise is much bigger than the Čerenkov effect and therefore the probability for measuring it is too low. Hence, a beam energy of 200 keV was chosen for the EMCD investigations due to stability and intensity reasons.

The EELS spectrum image of LCMO measured at 85 K can be seen in figure 6.1. It shows the $\Delta E - \vec{q}$ map including the O-K edge, the Mn-$L_{2,3}$ edges, the Co-$L_{2,3}$ edges and the La-$M_{4,5}$ edges. The spectral intensity $I_{\pm}$ after background subtraction measured at the specific off-axis positions is described by the double differential inelastic scattering cross section (see section 3.1.2):

$$I_{\pm} = I_0 \cdot \sigma_{\pm} \cdot N \cdot e^{-t/\lambda} \tag{6.1}$$

or

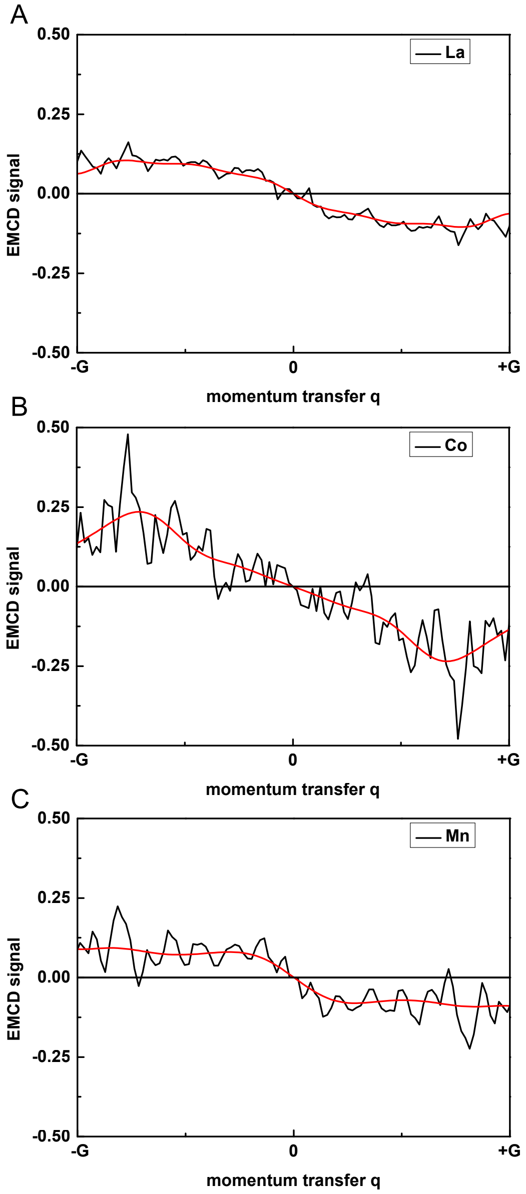

Figure 6.2: Asymmetric angular distribution of A) La-M_5 edge, B) Co-L_3 edge and C) Mn-L_3 edge. The red line in the graphs is the corresponding smoothed curve. All graphs show more or less a sinus-shaped curve, however, Co shows the most pronounced EMCD signal.

$$I_{\pm} = I_0 \cdot \frac{4\gamma^2}{a_0^2}\frac{k_f}{k_i}\left[|a|^2\frac{S(\vec{q},E)}{q^4} + |b|^2\frac{S(\vec{q'},E)}{q'^4} \pm 2\Re\left(ab^*\frac{S(\vec{q},\vec{q'},E)}{q^2q'^2}\right)\right]\cdot N\cdot e^{-t/\lambda} \quad (6.2)$$

where I_0 is the incident intensity, N is the number of atoms per unit volume of the specimen, t is the specimen thickness and λ is the mean free path. The equation 6.2 consists of two parts, the symmetric or Lorentz-shape distribution and the asymmetric distribution. The first two terms in the square bracket of equation 6.2 belong to the symmetric distribution, whereas the last term corresponds to the asymmetric distribution. The EMCD signal is the difference between I_+ and I_- and therefore, the symmetric part disappears and only the asymmetric part, the MDFF remains.

The magnetic potential of this asymmetric distribution can be seen by calculating the normalised dichroic signal [81, 115], which is obtained by

$$I_{EMCD} = \frac{I_+ - I_-}{I_+ + I_-} \quad (6.3)$$

The calculation of this asymmetric angular distribution of the EMCD signal can be done by integrating the intensity of the observed element edge from the reciprocal lattice vector +G to -G [83].

Theoretical considerations attribute magnetic behaviour to Co and Mn. Whereas O has no d-electrons and thus, no magnetic contribution. La itself is paramagnetic, has fully occupied 3d and 4d orbitals and only one 5d-electron. It is possible for La to show a magnetic behaviour, but it depends on the remaining elements in the compound. However, in TEM it is influenced by a magnetic field of 1.9 T and therefore, La can be sightly magnetic. The EMCD signals of the La-M_5 edge, the Co-L_3 edge and Mn-L_3 edge at 85 K are shown in figure 6.2. The La-M_5 edge provides a small dichroic signal, which shows that La contributes to the magnetic behaviour. The Co-L_3 edge shows the most pronounced EMCD signal, whereas for the Mn-L_3 edge the EMCD signal is smaller due to the non-optimised specimen thickness.

6.1.1 LCM100/STO

Figure 6.3 illustrates the normalised EMCD spectra of LCM100/STO showing the chemical sensitivity of EMCD. The EELS spectra of LCMO layer were pre-edge normalised and the background was subtracted by the power law method. Afterwards the spectra were normalised to the corresponding highest L_3 edge peak in the respective spectrum for the comparison of the EELS measurements at the ”+” and ”-” detector positions.

The upper row in figure 6.3 shows the experiments at 85 K with the $L_{2,3}$ edges of Mn at 640 eV energy loss (figure 6.3A) and Co at 779 eV energy loss (figure 6.3B). In the lower row the respective EMCD results of Mn (figure 6.3C) and Co (figure 6.3D) measured at RT are presented. By comparing the experiments at 85 K and RT it can be seen that in case of the experiments at 85 K intensity variations of the Co and Mn L_3 were detected, which shows induced chiral electronic transitions. While at RT no intensity variation was observed and thus, no EMCD effect was measured.

A crucial parameter for the detection of an EMCD signal is the sample thickness [80], which was in the range of 20 nm to 25 nm. The EMCD signal strength was not simulated [84], thus the optimum EMCD sample thickness was probably not used. The low signal-to-noise ratio during the experiments is caused by the preconditions of the classical EMCD method. The intensity of the EMCD signal is weak due to the tilting of the sample to a specific three-beam diffraction geometry and the off-axes positions of the signal detector, which were placed on the Thales circle besides the Bragg spots. Li et al. [116] has reported that a reason for the weak L_2 edge signal is the strong background noise.

Due to several aspects like the not optimized sample thickness and the low signal-to-noise ratio, which is caused by short recording times due to sample drift, a quantitative statement about the magnetisation cannot be given. However, the magnetism of the LCMO layer was proved with the EMCD experiments at 85 K and confirmed the expected behaviour at different temperatures. An effective EMCD signal of about 20 % at the Mn (figure 6.3A) and Co (figure 6.3B) edges was detected.

6.1.2 LCM300/Si

Compared to the previous sample LCM100/STO, the magnetic behaviour of the sample LCM300/Si was investigated by the EMCD setup corresponding to figure 3.4.

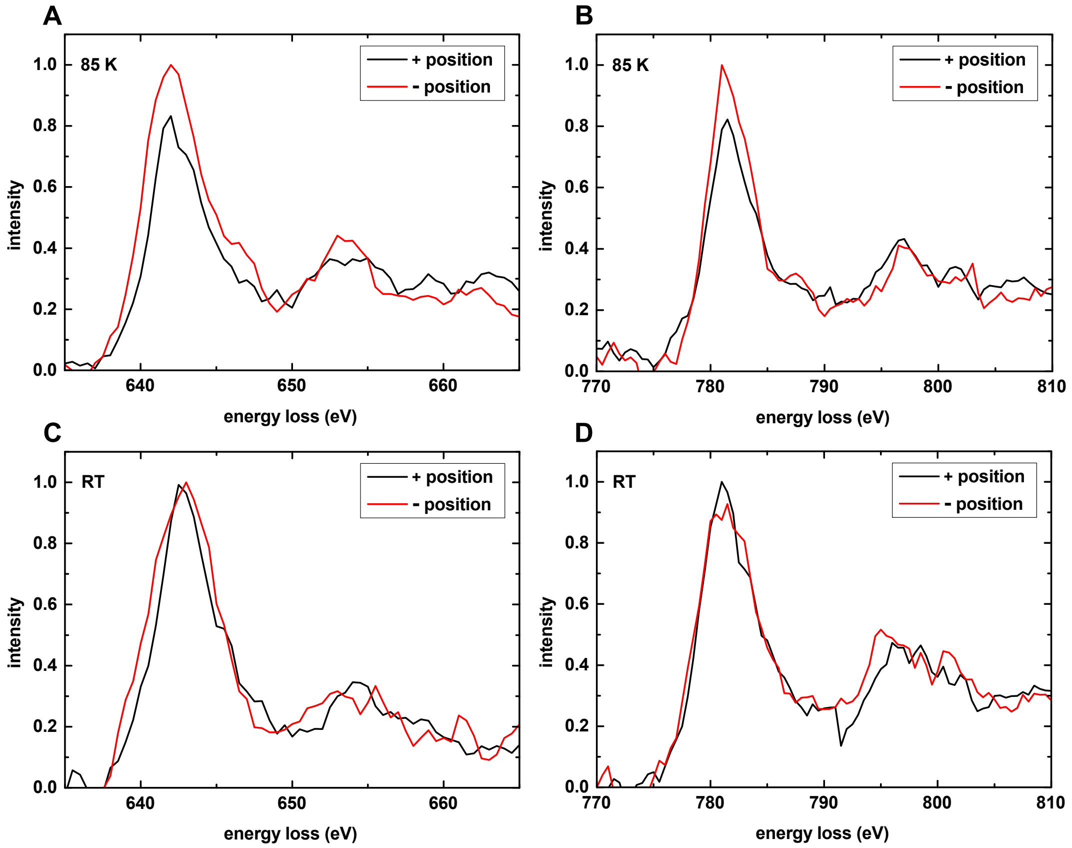

Figure 6.3: LCM100/STO: Normalised EMCD spectra of LCMO. The A) Mn and the B) Co edges show induced chiral electronic transitions at 85 K. At RT no EMCD signal is observed in either C) Mn or D) Co.

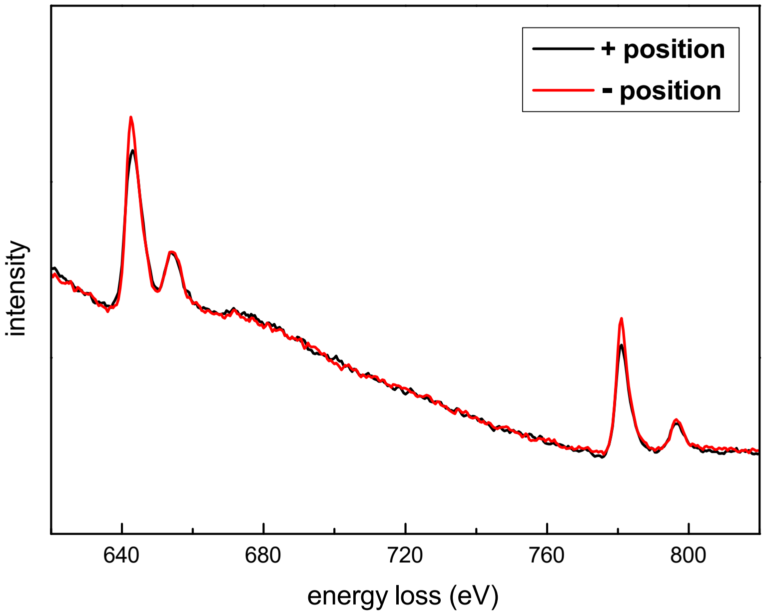

Figure 6.4: EELS spectra of sample LCM300/Si measured at 85 K with a beam energy of 200 keV presenting induced chiral electronic transitions at Mn (640 eV) and Co (779 eV) edges.

An $\Delta E - \vec{q}$ map was recorded with the same preconditions, which means that the three-beam case is configured in this way that a simultaneously recording of both "+" and "-" positions with different chiralities and both, Mn (640 eV) and Co (779 eV) edges is achieved (see figure 6.1). The acquisition of this spectrum image does not need long recording times for a good signal-to-noise ratio and thus, the recording time can be reduced and counteracts the sample drift.

The non-post treated EMCD spectra of sample LCM300/Si at 85 K are shown in figure 6.4. The EELS spectra show induced chiral electronic transitions and confirm the magnetic behaviour of the LCMO layer at lower temperatures. The experiments measured at RT are presented in figure 6.5 and exhibit the Mn and the Co edges with no intensity variation due to the perfect accordance of the EELS spectra at the "+" and "-" position. The used EMCD method improves the signal-to-noise ratio and thus, the spatial and energy resolution, which is reported by Hébert et al. [117].

For the purpose of verification, the spectra (figure 6.6) were post treated like the EMCD spectra from the previous sample LCM100/STO. After pre-edge normalisation and the background subtraction, the spectra were normalised to the corresponding highest L_3 edge peak in the respective spectrum.

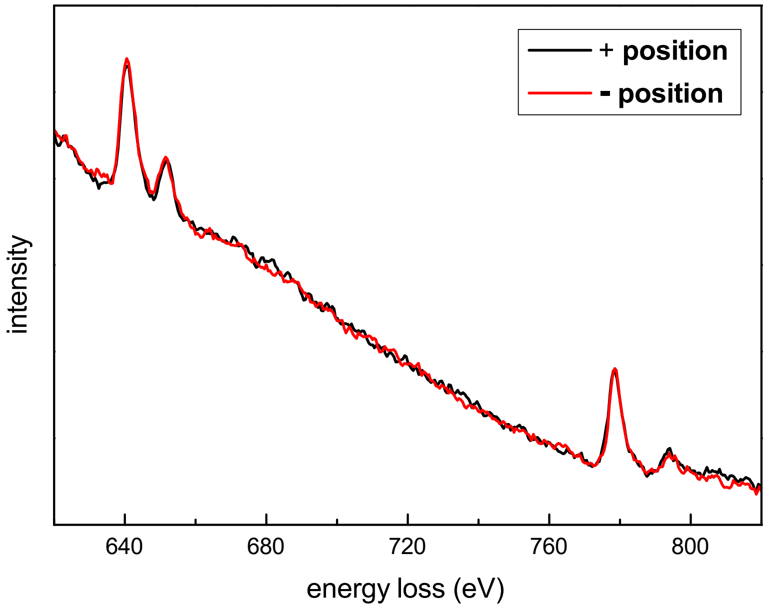

Figure 6.5: EELS spectra of sample LCM300/Si measured at RT with a beam energy of 200 keV showing no EMCD signal at Mn (640 eV) and Co (779 eV) edges.

In summary, the EMCD investigations confirm the literature by determining a strong magnetic effect in the Mn and Co $L_{2,3}$ edges at 85 K. At RT no EMCD signal was observable, which means that LCMO shows no magnetic behaviour.

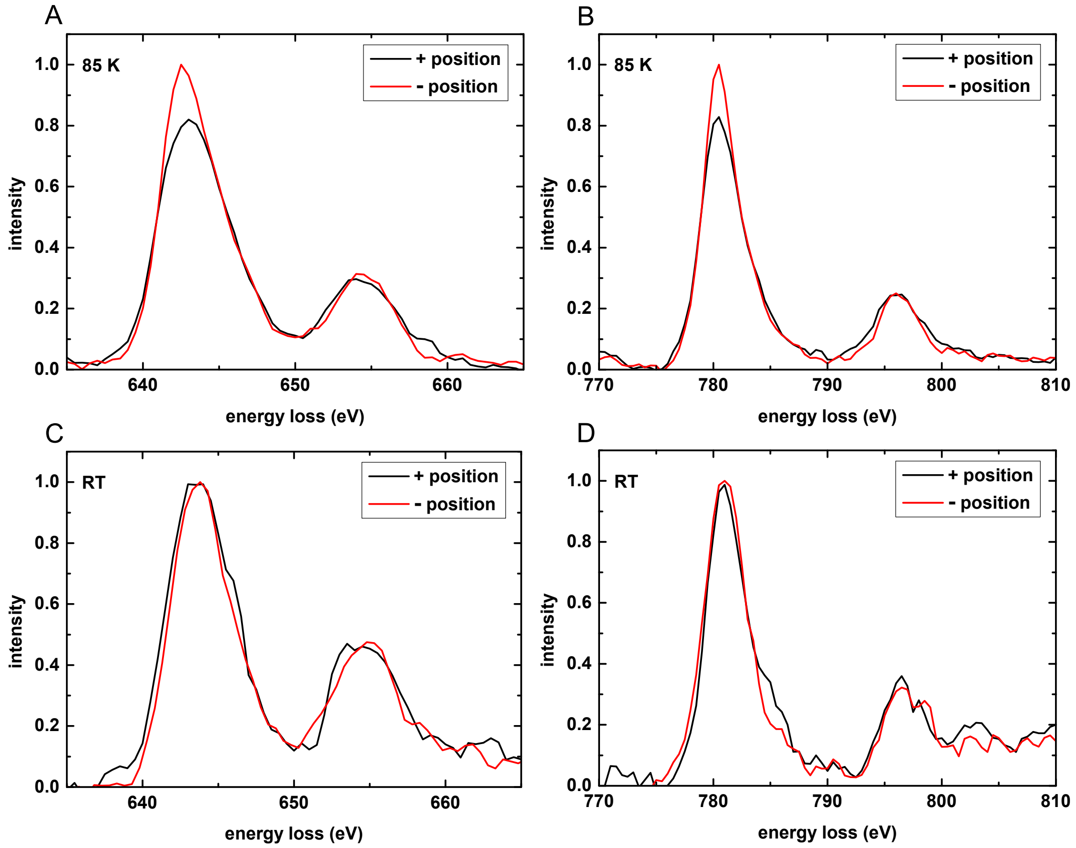

Figure 6.6: LCM300/Si: Normalised EMCD spectra of LCMO. The A) Mn and the B) Co edges show induced chiral electronic transitions at 85 K. At RT no EMCD signal is observed in either C) Mn or D) Co.

Chapter 7

Conclusion

7.1 Résumé in English

Over the last decades double perovskite manganites have been of great interest in many fields, such as magnetic storage or for solid oxide fuel cells. In particular, their huge negative magnetoresistance, which is known as CMR effect, is an interesting metal-insulator transition describing the electronic, optical and magnetic transformation of the material, such as the change in resistivity when applying a magnetic field.

In this work, a novel approach is introduced for detecting the consequences of the CMR effect on the nanometre scale. The combination of VEELS and EMCD experiments in TEM provides the opportunity to investigate the bandgap and the element specific magnetisation. Precise results are achieved by measuring the change of the interband transitions and the magnetisation both above and below T_C.

Double perovskites show a CMR effect which react very sensitive to defects and strains as caused, e.g., by the lattice misfit between thin film and substrate. The measure of distortion given by the Goldschmidt tolerance factor (see section 2.1) is high and deviates from the ideal cubic case. Hence, it is particularly important to characterise the CMR effect on the microscopic scale. The microstructure and its characteristics are analysed within section 3.3 and show an interesting behaviour of strain. The evolution of strain is induced more or less by the substrate and arises at the interface (figure 3.8). The investigations show tensile in-plane strain in the layer growing on STO and compressive in-plane strain for LAO. The applied synthesis pressure (figure 3.11) and the thickness (figure 3.12) of the layer have an important role in the formation and dominance of defects like columnar structure (figure 3.9) and take an influence on the dielectric and magnetic properties.

The compound LCMO is an ideal model system for investigating the consequences of the CMR effect in TEM (see figure 1.1) due to its material properties (see section 1.1). The VEELS experiments are focused on the detection of bandgap variations. No difference in the bandgap region could be determined above T_C by changing the applied magnetic field (see section 5.2 and figure 5.4B). However, below T_C the increase of the intensity was detected by lowering the external field from 1.9 T (200 keV) to 0.9 T (40 keV) and thus, a variation of the bandgap width. Consequently, a change of the resistivity was measured by means of VEELS (figure 5.4A). A qualitative change in the interband transitions of 0.14 eV was observed at 40 keV beam energy (see figure 5.5). The ellipsometry experiments of LCMO exhibit an increase of intensity in the low loss region by increasing the beam energy and therefore, the results below the Čerenkov limit are not influenced by relativistic losses. The experiments are supported by the calculation of the spin-dependent electronic density of states with DFT using the WIEN2k code. The GGA simulations corroborate that LCMO is a FM half-metal, which shows no insulator gap. GGA+U allows a bandgap development and thus, LCMO behaves like a FM semiconductor. The spectrum was calculated by using the package OPTIC (figure 5.16). The calculations confirm the interband transition peak at 5 eV (see figure 5.10) and support the interpretation of the interband transition shift of the VEELS measurements.

The magnetic observations by EMCD show that LCMO remains nearly unchanged with an applied external magnetic field above T_C and no magnetic behaviour was determined. When LCMO is cooled below T_C the properties are changing and an influence of the CMR effect can be seen at the L-ionization edges of both Co and Mn. This means that an EMCD signal was measured and thus, LCMO shows a ferromagnetic behaviour.

The insights gained by the new approach open new possibilities for solving challenging questions in the field of nanotechnology and its application in high-end healthcare techniques as well as information technology systems, spintronics and multiferroics.

In the future it would be interesting to repeat the experiments with a material which has a smaller refractive index and thus a higher Čerenkov limit. Hence, the impact of different external magnetic fields below the Čerenkov limit can be measured at low temperatures. Additionally, the direct detection of the CMR effect inside the strained region at nanometre scale is interesting to investigate in the future. However, the general CMR effect takes place close to T_C and for these investigations very stable measuring conditions are needed. The standard working temperature of a TEM has to be changed from RT close to T_C (e.g. T_C of LCMO is 210 K), which influences the working stability of the TEM. The cryo-transfer holder is very stable at RT or at 85 K and for adjusted temperatures the sample has to be permanently cooled. The holder tries to obtain the adjusted temperature, which induces small temperature oscillations. These temperature oscillations cause sample drifts which affect the TEM investigations at high magnifications. It would be interesting to investigate the CMR effect by using other types of cryo-transfer holders. In conclusion, the novel approach developed within this thesis detects the consequences of the CMR effect on nanometre scale at stable measuring conditions.

7.2 Résumé in German

Doppelperovskitmanganite sind seit Jahrzehnten von besonderem Interesse für die magnetische Speicherung, Brennstoffzellen und viele andere Anwendungen. Insbesondere ist ihr großer negativer Magnetowiderstand, welcher als CMR-Effekt bekannt ist, ein interessanter Metall-Isolator Übergang. Dieser Übergang beschreibt die elektronische, optische und magnetische Umwandlung des Materials, beispielsweise die Änderung des Widerstands beim Anlegen eines Magnetfelds.

In dieser Arbeit wird ein neuer Ansatz vorgestellt, um die Konsequenzen des CMR-Effekts im Nanometerbereich zu erfassen. Die Kombination von VEELS- und EMCD-Experimenten im TEM bietet die Möglichkeit Bandlücken und elementspezifische Magnetisierungen zu untersuchen. Sowohl die Änderung der Interbandübergänge als auch die Magnetisierung oberhalb sowie unterhalb von T_C werden präzise bestimmt.

Der CMR-Effekt bei Doppelperovskiten reagiert sehr empfindlich gegenüber Defekten und Spannungen, welche beispielsweise durch Gitterfehlanpassungen zwischen Dünnfilm und Substrat verursacht werden. Das Maß für die Verzerrung durch den Goldschmidt-Toleranzfaktor (siehe Abschnitt 2.1) ist hoch und weicht vom idealen kubischen Fall ab. Es ist daher von besonderer Bedeutung, den CMR-Effekt auch im mikroskopischen Maßstab zu bestimmen. Im Abschnitt 3.3 werden die Mikrostruktur und ihre Eigenschaften untersucht, die ein interessantes Spannungsverhalten aufweisen. Das Substrat ist für die induzierte Spannung in der Dünnschicht verantwortlich, welche durch Gitterfehlanpassungen im Grenzflächenbereich ersichtlich ist (Abbildung 3.8). Die Untersuchungen der Mikrostruktur zeigen, dass die Verwendung von STO als Substrat zu Zugspannungen in der Schicht und bei LAO zu Druckspannungen führt. Synthesedruck (Abbildung 3.11) und Schichtdicke (Abbildung 3.12) spielen eine wichtige Rolle bei der Bildung und Dominanz von Defekten wie der Säulenstruktur (Abbildung 3.9) und beeinflussen daher die dielektrischen und magnetischen Eigenschaften.

Die LCMO Verbindung ist ein ideales Modellsystem zur Untersuchung der Konsequenzen des CMR-Effekts im TEM (siehe Abbildung 1.1) aufgrund seiner Materialeigenschaften (siehe Abschnitt 1.1). Die VEELS-Experimente konzentrieren sich auf die Detektion der Bandlückenänderungen, mit welchen oberhalb von T_C trotz Änderung des Magnetfeldes kein Unterschied in der Bandlückenregion festgestellt werden konnte (siehe Abschnitt 5.2 und Abbildung 5.4B). Unterhalb von T_C wurde eine Änderung der Intensität durch Absenken des externen Feldes von 1,9 T (200 keV) auf 0,9 T (40 keV) und damit einer Änderung im Bandlückenbereich gemessen (Abbildung 5.4A). Bei einer Hochspannung von 40 keV wurde eine qualitative Änderung der Interbandübergänge von 0,14 eV von Raumtemperatur zu 85 K beobachtet (siehe Tabelle 5.1). Die Ellipsometrie-Experimente an LCMO zeigen durch Erhöhung der Hochspannung eine Intensitätszunahme im Bereich des Energieverlustspektrums schneller Elektronen, die auf relativistische Verluste (Čerenkov-Effekt) zurückzuführen ist. Die experimentellen Ergebnisse werden durch DFT-Berechnung der spinabhängigen elektronischen Zustandsdichten unter Verwendung des WIEN2k Codes unterstützt. Die GGA-Simulationen bestätigen, dass LCMO ein FM-Halbmetall ist und daher keine Isolatorlücke aufweist. Unter Einbeziehung des Hubbard Models mit den GGA+U-Berechnungen ist die Berücksichtigung einer Bandlücke möglich, sodass sich LCMO wie ein FM-Halbleiter verhält. Mit dem WIEN2k-Paket OPTIC wurde ein Energieverlustspektrum für LCMO berechnet, welches einen Interbandübergang bei 5 eV zeigt (Abbildung 5.16). Diese Berechnungen stimmen mit der gemessenen Interbandübergangsspitze bei 5 eV überein (siehe Abbildung 5.10) und unterstützen dadurch die Interpretation der Interbandübergangsverschiebung der VEELS Messungen.

Die magnetischen Untersuchungen mit EMCD zeigen, dass LCMO in einem externen Magnetfeld über T_C kein magnetisches Verhalten aufweist. Wenn LCMO auf eine Temperatur unter seiner T_C abgekühlt wurde, änderten sich die Eigenschaften und der Einfluss des CMR-Effekts ist an den L-Ionisationskanten von Co und Mn zu erkennen. Bei tiefen Temperaturen wurde ein EMCD-Signal von LCMO gemessen und somit zeigt LCMO ein ferromagnetisches Verhalten.

Die Erkenntnisse des neuen Ansatzes eröffnen neue Möglichkeiten für die Lösung herausfordernder Fragen im Bereich der Nanotechnologie und deren Anwendung in High-End-Gesundheitstechniken sowie in Informationstechnologiesystemen, Spintronik und Multiferroika.

In der Zukunft wird es interessant sein, die Versuche mit einem Material zu wiederholen, welches einen kleineren Brechungsindex und damit eine höhere Čerenkov-Grenze aufweist. Dadurch kann der Einfluss verschiedener äußerer Magnetfelder unterhalb der Čerenkov-Grenze bei tiefen Temperaturen gemessen werden. Darüber hinaus ist die direkte Erfassung des CMR-Effekts innerhalb des verspannten Bereichs bei höheren Vergrößerungen sehr interessant. Der allgemeine CMR-Effekt tritt in der Nähe von T_C auf und das bedeutet für das TEM, dass die Standardarbeitstemperatur von RT auf T_C geändert werden muss (z. B. T_C von LCMO = 210 K) und dabei die Arbeitsstabilität des TEM beeinflusst. Der Cryo-Transfer-Halter arbeitet sehr stabil bei RT und bei 85 K, bei dazwischenliegenden Temperaturen muss die Probe gekühlt oder erwärmt werden um die eingestellte Temperatur zu halten, dadurch werden kleine Temperaturschwankungen induziert. Diese Temperaturschwankungen verursachen einen Probendrift und dies beeinflusst die TEM-Untersuchungen bei hohen Vergrößerungen. Es wäre daher interessant, den CMR-Effekt unter Verwendung von moderneren Cryo-Transfer-Haltern zu untersuchen.

Der in dieser Arbeit präsentierte Ansatz ermöglicht die Ermittlung der Folgen des CMR-Effekts im Nanometerbereich unter stabilen Messbedingungen.

Bibliography

[1] G. H. Jonker and J. H. Van Santen. “Ferromagnetic compounds of manganese with perovskite structure”. In: *Physica* 16.3 (1950), pp. 337–349. DOI: `10.1016/0031-8914(50)90033-4`.

[2] G. Rathenau and J. Snoek. “Philips Research”. In: *Philips Ressearch Reports* 1 (1946), p. 239.

[3] J. Volger. “Further experimental investigations on some ferromagnetic oxidic compounds of manganese with perovskite structure”. In: *Physica* 20.1-6 (1954), pp. 49–66. DOI: `10.1016/S0031-8914(54)80015-2`.

[4] R. M. Kusters, J. Singleton, D. A. Keen, R. McGreevy, and W. Hayes. “Magnetoresistance measurements on the magnetic semiconductor $Nd_{0.5}Pb_{0.5}MnO_3$”. In: *Physica B: Physics of Condensed Matter* 155.1-3 (1989), pp. 362–365. DOI: `10.1016/0921-4526(89)90530-9`.

[5] R. von Helmolt, J. Wecker, B. Holzapfel, L. Schultz, and K. Samwer. “Giant negative magnetoresistance in perovskitelike $La_{2/3}B_{1/3}MnO_x$ ferromagnetic films”. In: *Physical Review Letters* 71.14 (1993), pp. 2331–2333. DOI: `10.1103/PhysRevLett.71.2331`.

[6] R. I. Dass and J. B. Goodenough. “Multiple magnetic phases of $La_2CoMnO_{6-\delta}$ ($0 < \delta < 0.05$)”. In: *Physical Review B* 67.1 (2003), p. 014401. DOI: `10.1103/PhysRevB.67.014401`.

[7] M. G. Masud, A. Ghosh, J. Sannigrahi, and B. K. Chaudhuri. “Observation of relaxor ferroelectricity and multiferroic behaviour in nanoparticles of the ferromagnetic semiconductor La_2NiMnO_2”. In: *Journal of physics. Condensed matter : an Institute of Physics journal* 24.29 (2012), p. 295902. DOI: `10.1088/0953-8984/24/29/295902`.

[8] R. X. Silva, A. S. De Menezes, R. M. Almeida, R. L. Moreira, R. Paniago, X. Marti, H. Reichlova, M. Maryško, M. V. D. S. Rezende, and C. W. A. Paschoal. “Structural order, magnetic and intrinsic dielectric properties of magnetoelectric La_2CoMnO_6”. In: *Journal of Alloys and Compounds* 661 (2016), pp. 541–552. DOI: `10.1016/j.jallcom.2015.11.097`.

[9] W. Z. Yang, X. Q. Liu, H. J. Zhao, and X. M. Chen. “Magnetic, dielectric and transport characteristics of Ln_2CoMnO_6 (Ln=Nd and Sm) double perovskite ceramics”. In: *Journal of Magnetism and Magnetic Materials* 371 (2014), pp. 52–59. DOI: `10.1016/j.jmmm.2014.07.017`.

[10] R. N. Mahato, K. Sethupathi, and V. Sankaranarayanan. “Colossal magnetoresistance in the double perovskite oxide La_2CoMnO_6”. In: *Journal of Applied Physics* 107.9 (2010), p. 09D714. DOI: `10.1063/1.3350907`.

[11] S. Yoo, A. Jun, Y.-W. Ju, D. Odkhuu, J. Hyodo, H. Y. Jeong, N. Park, J. Shin, T. Ishihara, and G. Kim. “Development of Double-Perovskite Compounds as Cathode Materials for Low-Temperature Solid Oxide Fuel Cells”. In: *Angewandte Chemie International Edition* 53.48 (2014), pp. 13064–13067. DOI: `10.1002/anie.201407006`.

[12] A. M. Haghiri-Gosnet, J. Wolfman, B. Mercey, C. Simon, P. Lecoeur, M. Korzenski, M. Hervieu, R. Desfeux, and G. Baldinozzi. “Microstructure and magnetic properties of strained $La_{0.7}Sr_{0.3}MnO_3$ thin films”. In: *Journal of Applied Physics* 88.7 (2000), p. 4257. DOI: `10.1063/1.1309040`.

[13] J. Krishna Murthy and A. Venimadhav. “Magnetodielectric behavior in La_2CoMnO_6 nanoparticles”. In: *Journal of Applied Physics* 111.2 (2012), p. 024102. DOI: `10.1063/1.3673862`.

[14] M. Viswanathan, P. S. A. Kumar, V. S. Bhadram, C. Narayana, A. K. Bera, and S. M. Yusuf. “Influence of lattice distortion on the Curie temperature and spin-phonon coupling in $LaMn_{0.5}Co_{0.5}O_3$”. In: *Journal of Physics-Condensed Matter* 22.346006 (2010), pp. 1–8. DOI: `10.1088/0953-8984/22/34/346006`.

[15] S. Yáñez-Vilar, M. Sánchez-Andújar, J. Rivas, and M. A. Señarís-Rodríguez. “Influence of the cationic ordering in the dielectric properties of the La_2MnCoO_6 perovskite”. In: *Journal of Alloys and Compounds* 485.1-2 (2009), pp. 82–87. DOI: `10.1016/j.jallcom.2009.05.103`.

[16] M. Ullah, S. Ayaz Khan, G. Murtaza, R. Khenata, N. Ullah, and S. Bin Omran. "Electronic, thermoelectric and magnetic properties of La_2NiMnO_6 and La_2CoMnO_6". In: *Journal of Magnetism and Magnetic Materials* 377 (2015), pp. 197–203. DOI: `10.1016/j.jmmm.2014.10.069`.

[17] N. Yuan, X. Liu, F. Meng, D. F. Zhou, and J. Meng. "First-principles study of La_2CoMnO_6: a promising cathode material for intermediate-temperature solid oxide fuel cells due to intrinsic Co-Mn cation disorder". In: *Ionics* 21.6 (2015), pp. 1675–1681. DOI: `10.1007/s11581-014-1320-z`.

[18] S. Baidya and T. Saha-Dasgupta. "Electronic structure and phonons in La_2CoMnO_6: A ferromagnetic insulator driven by Coulomb-assisted spin-orbit coupling". In: *Physical Review B - Condensed Matter and Materials Physics* 84.3 (2011), pp. 1–5. DOI: `10.1103/PhysRevB.84.035131`.

[19] M. Stöger-Pollach. "Low voltage TEM: Influences on electron energy loss spectrometry experiments". In: *Micron* 41.6 (2010), pp. 577–584. DOI: `10.1016/j.micron.2010.04.007`.

[20] M. Stöger-Pollach. "Comment on: "optical properties of metallic nanowires by valence electron energy loss spectroscopy"". In: *Materials Letters* 72 (2012), pp. 168–169. DOI: `10.1016/j.matlet.2011.10.055`.

[21] M. Stöger-Pollach. "Optical properties and bandgaps from low loss EELS: Pitfalls and solutions". In: *Micron* 39.8 (2008), pp. 1092–1110. DOI: `10.1016/j.micron.2008.01.023`.

[22] M. Stöger-Pollach. "A short note on how to convert a conventional analytical TEM into an analytical Low Voltage TEM". In: *Ultramicroscopy* 145 (2014), pp. 94–97. DOI: `10.1016/j.ultramic.2014.01.008`.

[23] I. Ennen, S. Löffler, C. Kübel, D. Wang, A. Auge, A. Hütten, and P. Schattschneider. "Site-specific chirality in magnetic transitions". In: *Journal of Magnetism and Magnetic Materials* 324.18 (2012), pp. 2723–2726. DOI: `10.1016/j.jmmm.2012.03.050`.

[24] P. Schattschneider, S. Rubino, C. Hébert, J. Rusz, J. Kunes, P. Novák, E. Carlino, M. Fabrizioli, G. Panaccione, and G. Rossi. "Detection of magnetic circular dichroism using a transmission electron microscope." In: *Nature* 441.7092 (2006), pp. 486–488. DOI: `10.1038/nature04778`.

[25] P. Schattschneider, M. Stöger-Pollach, S. Rubino, M. Sperl, C. Hurm, J. Zweck, and J. Rusz. “Detection of magnetic circular dichroism on the two-nanometer scale”. In: *Physical Review B* 78.10 (2008), p. 104413. DOI: `10.1103/PhysRevB.78.104413`.

[26] M. Stöger-Pollach. “Comment on: ”Direct measurement of local magnetic moments at grain boundaries in iron””. In: *Scripta Materialia* 69.11-12 (2013), pp. 820–822. DOI: `10.1016/j.scriptamat.2013.05.045`.

[27] W. Wallisch, M. Stöger-Pollach, and E. Navickas. “Consequences of the CMR effect on EELS in TEM”. In: *Ultramicroscopy* 179 (2017), pp. 84–89. DOI: `10.1016/j.ultramic.2017.04.011`.

[28] M. Johnsson and P. Lemmens. “Crystallography and Chemistry of Perovskites”. In: *Handbook of Magnetism and Advanced Magnetic Materials.* American Cancer Society, 2007. ISBN: 9780470022184. DOI: `10.1002/9780470022184.hmm411`.

[29] A.-M. Haghiri-Gosnet and J.-P. Renard. “CMR manganites: physics, thin films and devices”. In: *Journal of Physics D: Applied Physics* 36.8 (2003), R127–R150. DOI: `10.1088/0022-3727/36/8/201`.

[30] Y. Tokura and Y. Tomioka. “Colossal magnetoresistive manganites”. In: *Journal of Magnetism and Magnetic Materials* 200.1-3 (1999), pp. 1–23. DOI: `10.1016/S0304-8853(99)00352-2`.

[31] V. M. Goldschmidt. “Die Gesetze der Krystallochemie”. In: *Die Naturwissenschaften* 14.21 (1926), pp. 477–485. DOI: `10.1007/BF01507527`.

[32] H. Y. Hwang, S. W. Cheong, P. G. Radaelli, M. Marezio, and B. Batlogg. “Lattice effects on the magnetoresistance in doped $LaMnO_3$”. In: *Physical Review Letters* 75.5 (1995), pp. 914–917. DOI: `10.1103/PhysRevLett.75.914`.

[33] H. A. Jahn and E. Teller. “Stability of Polyatomic Molecules in Degenerate Electronic States. I. Orbital Degeneracy”. In: *Proceedings of the Royal Society A: Mathematical, Physical and Engineering Sciences* 161.905 (1937), pp. 220–235. DOI: `10.1098/rspa.1937.0142`.

[34] S. Krupička. *Physik der Ferrite und der verwandten magnetischen Oxide.* Vieweg+Teubner Verlag, 1973. ISBN: 978-3-528-08312-0. DOI: `10.1007/978-3-322-83522-2`.

[35] W. Nolting. “Austauschwechselwirkung”. In: *Quantentheorie des Magnetismus.* Vol. 80. Vieweg+Teubner Verlag, 1986, pp. 223–293. ISBN: 978-3-663-01080-7. DOI: `10.1007/978-3-663-01080-7_5`.

[36] C. Zener. “Interaction between the d-shells in the transition metals. II. Ferromagnetic compounds of manganese with Perovskite structure”. In: *Physical Review* 82.3 (1951), pp. 403–405. DOI: `10.1103/PhysRev.82.403`.

[37] P. W. Anderson and H. Hasegawa. “Considerations on double exchange”. In: *Physical Review* 100.2 (1955), pp. 675–681. DOI: `10.1103/PhysRev.100.675`.

[38] P. G. De Gennes. “Effects of double exchange in magnetic crystals”. In: *Physical Review* 118.1 (1960), pp. 141–154. DOI: `10.1103/PhysRev.118.141`.

[39] A. J. Millis, P. B. Littlewood, and B. I. Shraiman. “Double Exchange Alone Does Not Explain the Resistivity of $La_{1-x}Sr_x MnO_3$”. In: (1995). DOI: `10.1103/PhysRevLett.74.5144`.

[40] E. Dagotto, J. Burgy, and A. Moreo. “Nanoscale phase separation in colossal magnetoresistance materials: Lessons for the cuprates?” In: *Solid State Communications* 126.1-2 (2003), pp. 9–22. DOI: `10.1016/S0038-1098(02)00662-2`.

[41] E. Dagotto, T. Hotta, and A. Moreo. “Colossal magnetoresistant materials: the key role of phase separation”. In: *Physics Reports* 344.1-3 (2001), pp. 1–153. DOI: `10.1016/S0370-1573(00)00121-6`.

[42] R. Y. Gu, Z. D. Wang, and C. S. Ting. “Theory of electric-field-induced metal-insulator transition in doped manganites”. In: 77204 (2003), pp. 1–4. DOI: `10.1103/PhysRevB.67.153101`.

[43] T. Becker, C. Streng, Y. Luo, V. Moshnyaga, B. Damaschke, N. Shannon, and K. Samwer. “Intrinsic inhomogeneities in manganite thin films investigated with scanning tunneling spectroscopy”. In: *Physical Review Letters* 89.23 (2002), pp. 237203/1–237203/4. DOI: `10.1103/PhysRevLett.89.237203`.

[44] C. Jooss, L. Wu, T. Beetz, R. F. Klie, M. Beleggia, M. A. Schofield, S. Schramm, J. Hoffmann, and Y. Zhu. “Polaron melting and ordering as key mechanisms for colossal resistance effects in manganites”. In: *Proceedings of the National Academy of Sciences* 104.34 (2007), 13597 LP –13602.

[45] A. J. Millis. “Lattice effects in magnetoresistive manganese perovskites”. In: *Nature* 392.6672 (1998), pp. 147–150. DOI: `10.1038/32348`.

[46] M. Jaime, M. Salamon, M. Rubinstein, R. Treece, J. Horwitz, and D. Chrisey. “High-temperature thermopower films: Evidence for polaronic transport”. In: *Physical Review B - Condensed Matter and Materials Physics* 54.17 (1996), pp. 11914–11917. DOI: `10.1103/PhysRevB.54.11914`.

[47] P. Dai, J. A. Fernandez-Baca, N. Wakabayashi, E. W. Plummer, Y. Tomioka, and Y. Tokura. “Short-range polaron correlations in the ferromagnetic $La_{1-x}Ca_xMnO_3$”. In: *Physical Review Letters* 85.12 (2000), pp. 2553–2556. DOI: `10.1103/PhysRevLett.85.2553`.

[48] J. W. Lynn, D. N. Argyriou, Y. Ren, Y. Chen, Y. M. Mukovskii, and D. A. Shulyatev. “Order and dynamics of intrinsic nanoscale inhomogeneities in manganites”. In: *Physical Review B - Condensed Matter and Materials Physics* 76.1 (2007), pp. 1–8. DOI: `10.1103/PhysRevB.76.014437`.

[49] J. M. D. Coey, M. Viret, and S. von Molnár. “Mixed-valence manganites”. In: *Advances in Physics* 48.2 (1999), pp. 167–293. DOI: `10.1080/000187399243455`.

[50] H. Reinhardt. *Quantenmechanik 2*. DE GRUYTER, 2013. ISBN: 9783486855883. DOI: `10.1524/9783486855883`.

[51] P. Schattschneider. *Fundamentals of Inelastic Electron Scattering*. Springer Vienna, 1986, pp. 1–4. ISBN: 978-3-211-81937-1. DOI: `10.1007/978-3-7091-8866-8`.

[52] R. Egerton. *Electron Energy-Loss Spectroscopy in the Electron Microscope*. 2011, p. 491. ISBN: 978-1-4419-9582-7. DOI: `10.1007/978-1-4419-9583-4`. URL: `http://link.springer.com/10.1007/978-3-7091-8866-8fermi%20golden%20rule`.

[53] P. Schattschneider, B. Jouffrey, and M. Nelhiebel. "Dynamical diffraction in electron-energy-loss spectrometry: The independent Bloch-wave model". In: *Physical Review B - Condensed Matter and Materials Physics* 54.6 (1996), pp. 3861–3868. DOI: `10.1103/PhysRevB.54.3861`.

[54] R. H. Ritchie. "Plasma Losses by Fast Electrons in Thin Metal Films". In: *Physical Review* 106.5 (1957), pp. 874–881.

[55] M. Creuzburg. "Energieverlustspektren der Alkalihalogenide und der Metalle Cu, Ag und Au und Vergleich mit optischen Messungen". In: 463 (1966).

[56] J. Daniels. "Energieverlustmessungen an Silber mit hoher Energieauflösung". In: *Zeitschrift für Physik* 249 (1967), pp. 235–249.

[57] K. Zeppenfeld and H. Raether. "Energieverluste von 50 keV-Elektronen an Ge und Si". In: *Zeitschrift für Physik* 193.3 (1966), pp. 471–478. DOI: `10.1007/BF01326444`.

[58] C. Von Festenberg and E. Kröger. "Retardation effects for the electron energy loss probability in GaP and Si". In: *Physics Letters A* 26.8 (1968), pp. 339–340. DOI: `10.1016/0375-9601(68)90360-5`.

[59] E. Kröger. "Berechnung der Energieverluste schneller Elektronen in dünnen Schichten mit Retardierung". In: *Zeitschrift für Physik* 216.2 (1968), pp. 115–135. DOI: `10.1007/BF01390952`.

[60] E. Kröger. "Transition radiation, Cerenkov radiation and energy losses of relativistic charged particles traversing thin foils at oblique incidence - Theoretical calculations and numerical computations". In: *Zeitschrift für Physik* 235.5 (1970), pp. 403–421. DOI: `10.1007/BF01394931`.

[61] J. Daniels, C. von Festenberg, H. Raether, and K. Zeppenfeld. "Optical Constants of Solids by electron spectroscopy". In: *Springer tracts in modern Physics* 54 (1970), pp. 77–135. DOI: `10.1007/BFb0045978`.

[62] R. Erni and N. D. Browning. "The impact of surface and retardation losses on valence electron energy-loss spectroscopy". In: *Ultramicroscopy* 108.2 (2008), pp. 84–99. DOI: `10.1016/j.ultramic.2007.03.005`.

[63] M. Stöger-Pollach and P. Schattschneider. “The influence of relativistic energy losses on bandgap determination using valence EELS”. In: *Ultramicroscopy* 107.12 (2007), pp. 1178–1185. DOI: `10.1016/j.ultramic.2007.01.015`.

[64] S. Cottenier. *Density Functional Theory and the Family of (L)APW-methods: a step-by-step introduction.* 2013. ISBN: 9789080721517.

[65] P. Hohenberg and W. Kohn. “Inhomogeneous Electron Gas”. In: *Physical Review* 136.3B (1964), B864–B871. DOI: `10.1103/PhysRev.136.B864`.

[66] W. Kohn and L. J. Sham. “Self-consistent equations including exchange and correlation effects”. In: *Physical Review* 140.4A (1965). DOI: `10.1103/PhysRev.140.A1133`.

[67] P. Blaha, K. Schwarz, G. K. H. Madsen, D. Kvasnicka, J. Luitz, R. Laskowski, T. F., and L. D. Marks. *WIEN2k: An Augmented Plane Wave + Local Orbitals Program for Calculating Crystal Properties.* Karlheinz Schwarz, Techn. Universität Wien, Austria, 2018. ISBN: 3950103112.

[68] D. B. Williams and C. Carter. *Transmission Electron Microscopy.* Vol. 5. 721. Springer International Publishing, 2016, p. 760. ISBN: 978-3-319-26649-7. DOI: `10.1007/978-3-319-26651-0`.

[69] E. Abbe. “Beiträge zur Theorie des Mikroskops und der mikroskopischen Wahrnehmung”. In: *Archiv für Mikroskopische Anatomie* 9.1 (1873), pp. 413–418. DOI: `10.1007/BF02956173`.

[70] M. Knoll and E. Ruska. “Das Elektronenmikroskop”. In: *Zeitschrift für Physik* 78.5-6 (1932), pp. 318–339. DOI: `10.1007/BF01342199`.

[71] A. Gloter, A. Douiri, M. Tencé, and C. Colliex. “Improving energy resolution of EELS spectra: An alternative to the monochromator solution”. In: *Ultramicroscopy* 96.3-4 (2003), pp. 385–400. DOI: `10.1016/S0304-3991(03)00103-7`.

[72] M. Terauchi, R. Kuzuo, F. Satoh, M. Tanaka, K. Tsuno, and J. Ohyama. “Performance of a new high-resolution electron energy-loss spectroscopy microscope”. In: *Microscopical and Microanalytical Microstructures* 2 (1991), pp. 351–358. DOI: `10.1051/mmm:0199100202-3035100`.

[73] P. Schattschneider and B. Jouffrey. “Plasmons and Related Excitations”. In: *Energy-Filtering Transmission Electron Microscopy.* Ed. by L. Reimer. Springer Berlin Heidelberg, 1995, pp. 151–224. ISBN: 978-3-540-48995-5. DOI: `10.1007/978-3-540-48995-5_3`.

[74] D. Muller and J. Silcox. “Delocalization in inelastic scattering”. In: *Ultramicroscopy* 59.1-4 (1995), pp. 195–213. DOI: `10.1016/0304-3991(95)00029-Z`.

[75] R. F. Egerton. “New techniques in electron energy-loss spectroscopy and energy-filtered imaging”. In: *Micron* 34.3-5 (2003), pp. 127–139. DOI: `10.1016/S0968-4328(03)00023-4`.

[76] M. Stöger-Pollach. “Low voltage EELS-How low?” In: *Ultramicroscopy* 145 (2014), pp. 98–104. DOI: `10.1016/j.ultramic.2013.07.004`.

[77] R. F. Egerton. “Electron energy-loss spectroscopy in the TEM”. In: *Reports on Progress in Physics* 72.1 (2008), p. 016502. DOI: `10.1088/0034-4885/72/1/016502`.

[78] P. Schattschneider, S. Rubino, and C. Hébert. “Circular Dichroism in the Transmission Electron Microscope”. In: *Reference Module in Materials Science and Materials Engineering* (2016). DOI: `10.1016/B978-0-12-803581-8.03437-8`.

[79] G. Schütz, W. Wagner, W. Wilhelm, P. Kienle, R. Zeller, R. Frahm, and G. Materlik. “Absorption of circularly polarized x rays in iron”. In: *Physical Review Letters* 58.7 (1987), pp. 737–740. DOI: `10.1103/PhysRevLett.58.737`.

[80] P. Schattschneider, S. Rubino, M. Stöger-Pollach, C. Hébert, J. Rusz, L. Calmels, and E. Snoeck. “Energy loss magnetic chiral dichroism: A new technique for the study of magnetic properties in the electron microscope (invited)”. In: *Journal of Applied Physics* 103.7 (2008). DOI: `10.1063/1.2836680`.

[81] C. Hébert and P. Schattschneider. “A proposal for dichroic experiments in the electron microscope”. In: *Ultramicroscopy* 96.3-4 (2003), pp. 463–468. DOI: `10.1016/S0304-3991(03)00108-6`.

[82] H. Kohl and H. Rose. *Theory of Image Formation by Inelastically Scattered Electrons in the Electron Microscope.* Ed. by P. W. Hawkes. Vol. 65. C. Academic Press, 1985, pp. 173–227. ISBN: 9780120146659. DOI: `10.1016/S0065-2539(08)60878-1`.

[83] P. Schattschneider, C. Hébert, S. Rubino, M. Stöger-Pollach, J. Rusz, and P. Novák. "Magnetic circular dichroism in EELS: Towards 10 nm resolution". In: *Ultramicroscopy* 108.5 (2008), pp. 433–438. DOI: `10.1016/j.ultramic.2007.07.002`.

[84] S. Löffler and P. Schattschneider. "A software package for the simulation of energy-loss magnetic chiral dichroism". In: *Ultramicroscopy* 110.7 (2010), pp. 831–835. DOI: `10.1016/j.ultramic.2010.02.044`.

[85] H. Tompkins and E. A. Irene. *Handbook of ellipsometry.* 2005, p. 886. ISBN: 978-0-8155-1499-2.

[86] R. N. Mahato, K. K. Bharathi, K. Sethupathi, V. Sankaranarayanan, R. Nirmala, A. K. Nigam, and J. Lamsal. "Magnetic, transport, and magnetocaloric properties of double perovskite oxide $LaCaMnCoO_6$". In: *Journal of Applied Physics* 105.7 (2009), 07A908. DOI: `10.1063/1.3059592`.

[87] G. Van Tendeloo, O. Lebedev, and S. Amelinckx. "Atomic and microstructure of CMR materials". In: *Journal of Magnetism and Magnetic Materials* 211.1-3 (2000), pp. 73–83. DOI: `10.1016/S0304-8853(99)00716-7`.

[88] E. Navickas, Y. Chen, Q. Lu, W. Wallisch, T. M. Huber, J. Bernardi, M. Stöger-Pollach, G. Friedbacher, H. Hutter, B. Yildiz, and J. Fleig. "Dislocations Accelerate Oxygen Ion Diffusion in $La_{0.8}Sr_{0.2}MnO_3$ Epitaxial Thin Films". In: *ACS Nano* 11.11 (2017), pp. 11475–11487. DOI: `10.1021/acsnano.7b06228`.

[89] O. I. Lebedev, G. V. Tendeloo, A. M. Abakumov, S. Amelinckx, B. Leibold, and H. U. Habermeier. "A study of the domain structure of epitaxial $La_{1-x}Ca_xMnO_3$ films by high-resolution transmission electron microscopy". In: *Philosophical Magazine A* 79.6 (1999), pp. 1461–1478. DOI: `10.1080/01418619908210372`.

[90] T. Götsch, W. Wallisch, M. Stöger-Pollach, B. Klötzer, and S. Penner. "From zirconia to yttria: Sampling the YSZ phase diagram using sputter-deposited thin films". In: *AIP Advances* 6.2 (2016), p. 025119. DOI: `10.1063/1.4942818`.

[91] C. Gammer, C. Mangler, C. Rentenberger, and H. Karnthaler. "Quantitative local profile analysis of nanomaterials by electron diffraction". In: *Scripta Materialia* 63.3 (2010), pp. 312–315. DOI: `10.1016/j.scriptamat.2010.04.019`.

[92] M. Kogler, E.-M. Köck, B. Klötzer, T. Schachinger, W. Wallisch, R. Henn, C. W. Huck, C. Hejny, and S. Penner. "High-Temperature Carbon Deposition on Oxide Surfaces by CO Disproportionation". In: *The Journal of Physical Chemistry C* 120.3 (2016), pp. 1795–1807. DOI: `10.1021/acs.jpcc.5b12210`.

[93] R. Thalinger, T. Götsch, C. Zhuo, W. Hetaba, W. Wallisch, M. Stöger-Pollach, D. Schmidmair, B. Klötzer, and S. Penner. "Rhodium-Catalyzed Methanation and Methane Steam Reforming Reactions on Rhodium-Perovskite Systems: Metal-Support Interaction". In: *ChemCatChem* 8.12 (2016), pp. 2057–2067. DOI: `10.1002/cctc.201600262`.

[94] J. J. Peters, R. Beanland, M. Alexe, J. W. Cockburn, D. G. Revin, S. Y. Zhang, and A. M. Sanchez. "Artefacts in geometric phase analysis of compound materials". In: *Ultramicroscopy* 157 (2015), pp. 91–97. DOI: `10.1016/j.ultramic.2015.05.020`.

[95] M. J. Hÿtch, E. Snoeck, and R. Kilaas. "Quantitative measurement of displacement and strain fields from HREM micrographs". In: *Ultramicroscopy* 74.3 (1998), pp. 131–146. DOI: `10.1016/S0304-3991(98)00035-7`.

[96] C. Hurm, J. Zweck, M. Stöger-Pollach, S. Rubino, C. Hébert, and P. Schattschneider. "Verification of Electron Magnetic Chiral Dichroism in a TEM by Reversing the Specimen's Magnetisation". In: *Microscopy and Microanalysis* 13.S03 (2007), pp. 19–20. DOI: `10.1017/S1431927607080063`.

[97] T. Schachinger, S. Löffler, M. Stöger-Pollach, and P. Schattschneider. "Peculiar rotation of electron vortex beams". In: *Ultramicroscopy* 158 (2015), pp. 17–25. DOI: `10.1016/j.ultramic.2015.06.004`.

[98] W. Glaser. *Grundlagen der Elektronenoptik*. Springer Berlin Heidelberg, 1952, pp. 14–15. ISBN: 978-3-662-23620-8. DOI: `10.1007/978-3-662-25699-2`.

[99] M. Horák and M. Stöger-Pollach. "The Čerenkov limit of Si, GaAs and GaP in electron energy loss spectrometry." In: *Ultramicroscopy* 157 (2015), pp. 73–8. DOI: `10.1016/j.ultramic.2015.06.005`.

[100] A. O. Turky, M. M. Rashad, A. M. Hassan, E. M. Elnaggar, and M. Bechelany. "Optical, electrical and magnetic properties of lanthanum strontium manganite $La_{1-x}Sr_xMnO_3$ synthesized through the citrate combustion method". In: *Phys. Chem. Chem. Phys.* 19.9 (2017), pp. 6878–6886. DOI: `10.1039/C6CP07333F`.

[101] M. Stöger-Pollach, H. Franco, P. Schattschneider, S. Lazar, B. Schaffer, W. Grogger, and H. W. Zandbergen. "Cerenkov losses: A limit for bandgap determination and Kramers-Kronig analysis". In: *Micron* 37.5 (2006), pp. 396–402. DOI: `10.1016/j.micron.2006.01.001`.

[102] E. Cicerrella, J. L. Freeouf, L. F. Edge, D. G. Schlom, T. Heeg, J. Schubert, and S. A. Chambers. "Optical properties of La-based high-K dielectric films". In: *Journal of Vacuum Science & Technology A: Vacuum, Surfaces, and Films* 23.6 (2005), pp. 1676–1680. DOI: `10.1116/1.2056555`.

[103] S. G. Lim, S. Kriventsov, T. N. Jackson, J. H. Haeni, D. G. Schlom, A. M. Balbashov, R. Uecker, P. Reiche, J. L. Freeouf, and G. Lucovsky. "Dielectric functions and optical bandgaps of high-K dielectrics for metal-oxide-semiconductor field-effect transistors by far ultraviolet spectroscopic ellipsometry". In: *Journal of Applied Physics* 91.7 (2002), pp. 4500–4505. DOI: `10.1063/1.1456246`.

[104] M. Cesaria, A. P. Caricato, G. Leggieri, M. Martino, and G. Maruccio. "Optical response of oxygen deficient $La_{0.7}Sr_{0.3MnO3}$ thin films deposited by pulsed laser deposition". In: *Thin Solid Films* 545 (2013), pp. 592–600. DOI: `10.1016/j.tsf.2013.07.071`.

[105] V. J. Keast. "An introduction to the calculation of valence EELS: Quantum mechanical methods for bulk solids". In: *Micron* 44.1 (2013), pp. 93–100. DOI: `10.1016/j.micron.2012.08.001`.

[106] K. Jorissen, J. J. Rehr, and J. Verbeeck. “Multiple scattering calculations of relativistic electron energy loss spectra”. In: *Physical Review B - Condensed Matter and Materials Physics* 81.15 (2010), pp. 1–6. DOI: `10.1103/PhysRevB.81.155108`.

[107] C. Hébert. “Practical aspects of running the WIEN2k code for electron spectroscopy”. In: *Micron* 38.1 (2007), pp. 12–28. DOI: `10.1016/j.micron.2006.03.010`.

[108] C. L. Bull, D. Gleeson, and K. S. Knight. “Determination of B-site ordering and structural”. In: *Journal of Physics: Condensed Matter* 15 (2003), p. 4927. DOI: `10.1088/0953-8984/15/29/304`.

[109] M. Zhu, Y. Lin, E. W. C. Lo, Q. Wang, Z. Zhao, and W. Xie. “Electronic and magnetic properties of La_2NiMnO_6 and La_2CoMnO_6 with cationic ordering”. In: *Applied Physics Letters* 100.6 (2012), p. 062406. DOI: `10.1063/1.3683550`.

[110] S. Lv, Z. Wang, M. Saito, and Y. Ikuhara. “Atomic and electronic structure of La_2CoMnO_6 on $SrTiO_3$ and $LaAlO_3$ substrates from first principles”. In: *Journal of Applied Physics* 113.20 (2013). DOI: `10.1063/1.4807410`.

[111] S. F. Matar, M. A. Subramanian, A. Villesuzanne, V. Eyert, and M. H. Whangbo. “First principles investigation of the electronic structure of La_2MnNiO_6: An insulating ferromagnet”. In: *Journal of Magnetism and Magnetic Materials* 308.1 (2007), pp. 116–119. DOI: `10.1016/j.jmmm.2006.05.029`.

[112] J. Perdew, J. Chevary, S. Vosko, K. Jackson, M. Pederson, D. Singh, and C. Fiolhais. “Atoms, molecules, solids, and surfaces: Applications of the generalized gradient approximation for exchange and correlation”. In: *Physical Review B* 46.11 (1992), pp. 6671–6687. DOI: `10.1103/PhysRevB.48.4978.2`.

[113] V. J. Keast. “Ab initio calculations of plasmons and interband transitions in the low-loss electron energy-loss spectrum”. In: *Journal of Electron Spectroscopy and Related Phenomena* 143.2-3 SPEC. ISS. (2005), pp. 97–104. DOI: `10.1016/j.elspec.2004.04.005`.

[114] C. Ambrosch-Draxl and J. O. Sofo. “Linear optical properties of solids within the full-potential linearized augmented planewave method”. In: *Computer Physics Communications* 175.1 (2006), pp. 1–14. DOI: `10.1016/j.cpc.2006.03.005`.

[115] S. W. Lovesey and S. P. Collins. *X-ray scattering and absorption by magnetic materials*. 1. Oxford University Press, 1996.

[116] G. Li, D. Song, Z. P. Li, and J. Zhu. “Determination of magnetic parameters in $La_{0.7}Sr_{0.3}MnO_3/SrTiO_3$ thin films using EMCD”. In: *Applied Physics Letters* 108.24 (2016), pp. 3–7. DOI: `10.1063/1.4954168`.

[117] C. Hébert, P. Schattschneider, S. Rubino, P. Novak, J. Rusz, and M. Stöger-Pollach. “Magnetic circular dichroism in electron energy loss spectrometry”. In: *Ultramicroscopy* 108.3 (2008), pp. 277–284. DOI: `10.1016/j.ultramic.2007.07.011`.

List of Figures

List of Tables

List of Abbreviations

BF:	bright field
CMR:	colossal magnetoresistance
DF:	dark field
DFF:	dynamic form factor
DFT:	density functional theory
EDX:	energy-dispersive X-ray spectroscopy
EELS:	electron energy loss spectrometry
ELNES:	energy loss near edge structure
EMCD:	energy-loss magnetic circular dichroism
FIB:	focused ion beam
FiM:	ferrimagnetic
FM:	ferromagnetic
FOXSI:	Functional OXide Surfaces and Interfaces
FT:	Fourier transform
FWHM:	full width half maximum
GGA:	general gradient approximation
GPA:	geometric phase analysis
HRTEM:	high-resolution TEM

JDOS:	joint density of states
KKA:	Kramers-Kronig analysis
KKR:	Kramers-Kronig relation
LAO:	$LaAlO_3$
LCMO:	La_2CoMnO_6
LSF:	$La_{0.6}Sr_{0.4}FeO_{3-\delta}$
LSMO:	$La_{0.8}Sr_{0.2}MnO_3$
MDFF:	mixed dynamic form factor
PLD:	pulse laser deposition
RCE:	rotating compensator ellipsometer
RL:	Richardson-Lucy
RT:	room temperature
SCF:	self-consistent field
SSD:	single volume scattering distribution
STEM:	scanning TEM
STF:	$SrTi_{0.7}Fe_{0.3}O_{3-\delta}$
STO:	$SrTiO_3$
T_C:	Curie temperature
TEM:	transmission electron microscopy
USTEM:	University Service Center for Transmission Electron Microscopy
VEELS:	valence electron energy loss spectrometry
XANES:	X-ray absorption near edge structure

XAS:	X-ray absorption spectroscopy
XMCD:	X-ray magnetic circular dichroism
XRD:	X-ray diffraction
YSZ:	yttria-stabilised zirconia
ZLP:	zero loss peak

Curriculum Vitae

Dipl.-Ing. Wolfgang Wallisch, BSc

Born 27.09.1987 in Vienna, Austria.

Work & Research Experience

12/2018 - present	**Medical physicist** Department of Biomedical Imaging and Image-guided Therapy, Vienna General Hospital (AKH Wien)
05/2018:	**Research assistent** Project with CEITEC in Brno / Czech Republic
05/2015 - 11/2018	**Research assistent** University Service Centre for Transmission Electron Microscopy (USTEM), Technische Universität (TU) Wien
11/2012 - 04/2015	**Research assistent** Institute for Solid State Physics, TU Wien
07/2012 - 10/2012	**Student assistent** Institute for Solid State Physics, TU Wien
07/2011 - 12/2011	**Student assistent** Institute for Solid State Physics, TU Wien

Education

06/2017	Attendance at the CCEM School on Electron Microscopy in Hamilton, Canada.
06/2016	Attendance at the International School on Fundamental Crystallography with applications to Electron Crystallography in Antwerp, Belgium.
10/2015 - 05/2019	PhD program in Technical Physics, TU Wien.
04/2015	Master degree in Technical Physics, TU Wien, *”Synthesis and TEM investigation of (Fe, Co)*$_{2-3}$*B: A compound for rare earth free permanent magnets”.*
09/2014	Attendance at the European Workshop on Quantitative STEM, EELS and EDXSin Piran, Slovenia.
02/2013	Attendance at the ViCoM Winter School in St. Christoph, Austria, *”Phase stability and phase transitions on soft and hard materials”.*
11/2012 - 04/2015	Master program in Technical Physics, TU Wien.
11/2012	Bachelor degree in Technical Physics, TU Wien, *”Preparation and TEM investigation of (FePt) multilayer systems”.*
10/2007 – 10/2012	Bachelor program in Technical Physics, TU Wien.
09/2006 – 02-2007	Basic military service (Präsenzdienst).
06/2006	Matura (school leaving examination), Vienna.

Awards

06/2017	Best Poster Award at the 21st International Conference Solid State Ionics.
04/2014	The project Rare-Earth Free Permanent Magnets (REFREEPERMAG) received an award as one of the “Best on-going Project” in FP7 of the EU.

Publications

Paper

W. Wallisch, M. Stöger-Pollach, E. Navickas: *“Consequences of the CMR effect on EELS in TEM”*; Ultramicroscopy, 179 (2017), S. 84 – 89, DOI: 10.1016/j.ultramic.2017.04.011.

E. Navickas, Y. Chen, Q. Lu, W. Wallisch, T. Huber, J. Bernardi, M. Stöger-Pollach, G.Friedbacher, H. Hutter, B. Yildiz, J. Fleig: *”Dislocations Accelerate Oxygen Ion Diffusion in* $La_{0.8}Sr_{0.2}MnO_3$ *Epitaxial Thin Films”*; ACS Nano, 11 (2017), S. 11475 – 11487, DOI: 10.1021/acsnano.7b06228.

R. Thalinger, T. Götsch, C. Zhuo, W. Hetaba, W. Wallisch, M. Stöger-Pollach, D. Schmidmair, B. Klötzer, S. Penner: *“Rhodium-Catalyzed Methanation and Methane Steam Reforming Reactions on*; *Rhodium-Perovskite Systems: Metal-Support Interaction”*; ChemCatChem, 8 (2016), S. 2057 – 2067, DOI: 10.1002/cctc.201600262.

M. Kogler, E.-M. Köck, B. Klötzer, T. Schachinger, W. Wallisch, R. Henn, C. W. Huck, C. Hejny, and S. Penner: *“High-Temperature Carbon Deposition on Oxide Surfaces by CO Disproportionation”*; Journal of Physical Chemistry C, 120 (2016), no. 3, 1795–1807, DOI: 10.1021/acs.jpcc.5b12210.

T. Götsch, W. Wallisch, M. Stöger-Pollach, B. Klötzer, and S. Penner: *“From zirconia to yttria: Sampling the YSZ phase diagram using sputter-deposited thin films”*; AIP Advances, 6 (2016), no. 2, DOI: 10.1063/1.4942818.

V. Alexandrakis, W. Wallisch, Sven Hamann, G. Varvaro, J. Fidler, A. Ludwig: *”Combinatorial development of Fe-Co-Nb thin film magnetic nanocomposites”*; ACS Combinatorial Science, 17 (2015), 698 – 703, DOI: 10.1021/acscombsci.5b00116.

G. Giannopoulos, L. Reichel, A. Markou, W. Wallisch, M. Stöger-Pollach, I. Panagiotopoulos, V. Psycharis, S. Fähler, J. Fidler, D. Niarchos: *”Structural and magnetic properties of strongly carbon doped Fe-Co thin films”*; Journal of Magnetism and Magnetic Materials, 393 (2015), 479 – 483, DOI: 10.1016/j.jmmm.2015.06.018.

P. Toson, A. Asali, W. Wallisch, G. A. Zickler, J. Fidler: *"Nanostructured Hard Magnets: A Micromagnetic Study"*; IEEE Transactions on Magnetics, 51 (2015), 7400104-1 - 7400104-4, DOI: 10.1109/TMAG.2014.2359093.

W. Wallisch, J. Fidler, P. Toson, H. Sassik, R. Svagera, J. Bernardi: *"Synthesis and characterisation of (Fe,Co)2-3B microcrystalline alloys"*; Journal of Alloys and Compounds, 644 (2015), 199 – 204, DOI: 10.1016/j.jallcom.2015.04.179.

Contributions to Proceedings

W. Wallisch, M. Stöger-Pollach, E. Navickas, S. Löffler: *"Advances towards investigating electronic and optical transformation of* La_2CoMnO_6*"*; Talk: 19th International Microscopy Congress, Sydney, Australia; 09.09.2018 - 14.09.2018; in: "19th International Microscopy Congress", (2018).

W. Wallisch, M. Stöger-Pollach, S. Löffler, E. Navickas: *"EELS experiments influenced by the CMR effect"*; Talk: 13th Multinational Congress on Microscopy, Rovinj, Croatia; 24.09.2017 - 29.09.2017; in: “13th Multinational Congress on Microscopy”, (2017), S. 181 - 182.

W. Wallisch, M. Stöger-Pollach, S. Löffler, E. Navickas: *"Influences of the CMR effect on energy loss signal"*; Talk: Microscopy Conference 2017, Lausanne, Switzerland; 21.08.2017 - 25.08.2017; in: “MC 2017 Lausanne - Microscopy Conference”, (2017), S. 698 - 699.

E. Navickas, T. Huber, Y. Chen, Q. Lu, W. Wallisch, J. Bernardi, M. Stöger-Pollach, H. Hutter, B. Yildiz, J. Fleig: *"Misfit Dislocations Accelerate Oxygen Ion Diffusion in* $La_{0.8}Sr_{0.2}MnO_3$ *Epitaxial Thin Films"*; Poster: Solid State Ionics 21st International Conference, Padua, Italy; 18.06.2017 - 23.06.2017; in: “Solid State Ionics”, (2017), S. 603.

W. Wallisch, M. Stöger-Pollach, E. Navickas, A. Steiger-Thirsfeld, J. Bernardi: *"VEELS investigation of perovskite manganite interfaces"*; Poster: The 16th European Microscopy Congress, Lyon, France; 28.08.2016 - 02.09.2016; in: “The 16th European Microscopy Congress”, (2016).

T. Götsch, W. Wallisch, M. Stöger-Pollach, A. Menzel, B. Klötzer, S. Penner: *”From zirconia to yttria - sampling the YSZ phase diagram using sputter-deposited thin films”*; Poster: Microscopy Conference 2015, Göttingen, Deutschland; 06.09.2015 - 11.09.2015; in: ”Microscopy Conference 2015 Proceedings”, DGE - German Society for Electron Microscopy, e.V., (2015), S. 68 - 69.

T. Götsch, W. Wallisch, M. Stöger-Pollach, A. Menzel, B. Klötzer, S. Penner: *”From zirconia to yttria - Sampling the YSZ phase diagram using sputter-deposited thin films”*; Poster: 12th Multinational Congress on Microscopy, Eger, Hungary; 23.08.2015 – 28.08.2015; in: “12th Multinational Congress on Microscopy”, Hungarian Academy of Sciences, Eger, Hungary (2015), 547 - 549.

W. Wallisch, M. Stöger-Pollach, G. A. Zickler, G. Giannopoulos, D. Niarchos, J. Fidler: *”EMCD investigation of Co-Fe thin films doped with carbon by Analytical TEM”*; Poster: 18th International Microscopy Congress, Prague, Czech Republic; 07.09.2014 – 12.09.2014; in: “18th International Microscopy Congress Proceedings”, Czechoslovak Microscopy Society, (2014), ISBN: 978-80-260-6720-7; Paper ID MS-12-P-2050, 2 pages.

G. A. Zickler, W. Wallisch, M. Stöger-Pollach, J. Bernardi, K. Üstüner, J. Fidler: *”TEM investigation of grain boundaries from Nd2Fe14B hard magnets”*; Poster: 18th International Microscopy Congress, Prague, Czech Republic; 07.09.2014 - 12.09.2014; in: ”18th International Microscopy Congress Proceedings”, Czechoslovak Microscopy Society, (2014), ISBN: 978-80-260-6720-7; Paper-Nr. MS-12-P-1643, 2 pages.

G. Giannopoulos, C. Sarafidis, M. Gjoka, L. Reichel, A. Markou, W. Wallisch, V. Psycharis, J. Fidler, D. Niarchos: *”Rare Earth Free Permanent Magnets”*; in: “REPM 2014 - 23 Int. Workshop on Rare Earth and Future Permanent Magnets and Their Applications”, University of Delaware, USA, 2014, 388 - 392.

Talks and Poster Presentations

W. Wallisch: *”Detecting the Consequences of the CMR Effect in Electron Energy-Loss Spectrometry in TEM”*; Talk: IFP-Seminar, Vienna, Austria; 27.11.2018.

W. Wallisch, M. Stöger-Pollach, E. Navickas, S. Löffler: *Advances towards investigating electronic and optical transformation of* La_2CoMn_6; Talk: 19th International Microscopy Congress, Sydney, Australia; 05.09.2018 - 09.09.2018.

W.Wallisch: *"Detecting electron energy losses by measuring colossal magnetoresistance"*; Invited Talk: Seminar of the Department of Solid State Physics and Surfaces, Brno University of Technology, Czech Republic; 02.05.2018.

W. Wallisch, M. Stöger-Pollach, E. Navickas, S. Löffler: *"CMR Effect Investigations by Energy Loss"*; Invited Poster: 8th ASEM-Workshop, Vienna, Austria; 26.04.2018 - 27.04.2018.

A. Viernstein, E. Navickas, M. Kubicek, W. Wallisch, J. Fleig: *"Electrochemical characterization of Mixed-Conducting* $(Ca, La, Sr)(Co, Mn)O_3$*"*; Poster: 17. Österreichische Chemietage 2017, Salzburg, Austria; 25.09.2017 - 28.09.2017.

W. Wallisch, M. Stöger-Pollach, S. Löffler, E. Navickas: *"EELS experiments influenced by the CMR effect"*; Talk: 13th Multinational Congress on Microscopy, Rovinj, Croatia; 24.09.2017 - 29.09.2017; in: "13th Multinational Congress on Microscopy", (2017), S. 181 - 182.

W. Wallisch, M. Stöger-Pollach, S. Löffler, E. Navickas: *"Influences of the CMR effect on energy loss signal"*; Talk: Microscopy Conference 2017, Lausanne, Switzerland; 21.08.2017 - 25.08.2017; in: "MC 2017 Lausanne - Microscopy Conference", (2017), S. 698 - 699.

E. Navickas, T. Huber, Y. Chen, Q. Lu, W. Wallisch, J. Bernardi, M. Stöger-Pollach, H. Hutter, B. Yildiz, J. Fleig: *"Misfit Dislocations Accelerate Oxygen Ion Diffusion in* $La_{0.8}Sr_{0.2}MnO_3$ *Epitaxial Thin Films"*; Poster: Solid State Ionics 21st International Conference, Padua, Italy; 18.06.2017 - 23.06.2017; in: "Solid State Ionics", (2017), S. 603.

W. Wallisch, M. Stöger-Pollach, E. Navickas: *”How does the CMR effect influence EELS in TEM?”*; Talk: International FOXSI Conference 2017, Vienna, Austria; 15.05.2017 - 17.05.2017.

W. Wallisch, M. Stöger-Pollach, E. Navickas: *”Influences of the CMR effect on dielectric properties”*; Talk: 7th ASEM-Workshop - Advanced Electron Microscopy, Vienna, Austria; 20.04.2017 - 21.04.2017.

W. Wallisch, M. Stöger-Pollach, E. Navickas: *”Focusing on energy losses: How does the CMR effect affect EELS in TEM?”*; Invited Talk: Research Division Electrochemistry of Prof. Fleig, Vienna, Austria; 05.04.2017.

W. Wallisch, M. Stöger-Pollach, E. Navickas, A. Steiger-Thirsfeld, J. Bernardi: *”VEELS investigation of perovskite manganite interfaces”*; Poster: The 16th European Microscopy Congress, Lyon, France; 28.08.2016 - 02.09.2016; in: “The 16th European Microscopy Congress”, (2016).

W. Wallisch, M. Stöger-Pollach, E. Navickas, A. Steiger-Thirsfeld, J. Bernardi: *”Analytical TEM investigation of as LSM thin film layer”*; Poster: International School on Fundamental Crystallography with applications to Electron Crystallography, Antwerpen, Belgium; 27.06.2016 - 02.07.2016.

W. Wallisch, M. Stöger-Pollach, E. Navickas, A. Steiger-Thirsfeld, J. Bernardi: *”Determining optical properties of* $LaSrMnO_3$-$LaAlO_3$ *interfaces by VEELS investigations”*; Poster: International FOXSI Conference, Vienna, Austria; 23.05.2016 - 25.05.2016.

W. Wallisch, M. Stöger-Pollach, E. Navickas, A. Steiger-Thirsfeld, O. Bethge: *”Analysis of optical properties of LSM-LAO interfaces by means of VEELS”*; Talk: 6th ASEM Workshop, Leoben, Austria; 28.04.2016 - 29.04.2016.

T. Götsch, W. Wallisch, M. Stöger-Pollach, A. Menzel, B. Klötzer, S. Penner: *”From Zirconia to Yttria: Sampling the YSZ phase diagram using sputter-deposited thin films”*; Poster: 16. Österreichische Chemietage, Innsbruck, Austria; 21.09.2015 - 24.09.2015.

W. Wallisch, M. Stöger-Pollach, W. Hetaba, T. Schachinger, A. Steiger-Thirsfeld, S. Schwarz, J. Bernardi: *”Analytical Electron Microscopy of FOXSI (Functional Oxide Surfaces and interfaces)”*; Poster: 4th Annual SFB FOXSI Symposium, Stadtschlaining, Austria; 14.09.2015 - 16.09.2015.

T. Götsch, W. Wallisch, M. Stöger-Pollach, A. Menzel, B. Klötzer, S. Penner: *”From Zirconia to Yttria: Sampling the YSZ phase diagram using sputter-deposited thin films”*; Poster: 4th Annual SFB FOXSI Symposium, Stadtschlaining, Austria; 14.09.2015 - 16.09.2015.

E. Navickas, T. Huber, Y. Chen, W. Wallisch, J. Bernardi, G. M. Rupp, H. Hutter, B. Yildiz, J. Fleig: *”Oxygen exchange and diffusion in Sr-doped* $LaMnO_3$ *Epitaxial thin films”*; Poster: 4th Annual SFB FOXSI Symposium, Stadtschlaining, Austria; 14.09.2015 - 16.09.2015.

T. Götsch, W. Wallisch, M. Stöger-Pollach, A. Menzel, B. Klötzer, S. Penner: *”From zirconia to yttria - sampling the YSZ phase diagram using sputter-deposited thin films”*; Poster: Microscopy Conference 2015, Göttingen, Germany; 06.09.2015 – 11.09.2015; in: ”Microscopy Conference 2015 Proceedings”, DGE - German Society for Electron Microscopy, e.V., (2015), 68 - 69.

T. Götsch, W. Wallisch, M. Stöger-Pollach, A. Menzel, B. Klötzer, S. Penner: *”From zirconia to yttria - Sampling the YSZ phase diagram using sputter-deposited thin films”*; Poster: 12th Multinational Congress on Microscopy, Eger, Hungary; 23.08.2015 - 28.08.2015; in: ”12th Multinational Congress on Microscopy”, Hungarian Academy of Sciences, Eger, Hungray (2015), 547 - 549.

V. Alexandrakis, W. Wallisch, S. Hamann, J. Fidler, A. Ludwig: *”Combinatorial Development of Fe-Co-Nb thin Film magnetic nanocomposites”*; Poster: 20th International Conference on Magnetism, Barcelona, Spain; 05.07.2015 – 10.07.2015.

W. Wallisch, P. Toson, M. Stöger-Pollach, J. Bernardi, J. Fidler: *”SEM and TEM investigation for the characterization of* $(Fe,Co)_{2-3}B$ *alloys”*; Talk: 5th ASEM Workshop on Advanced Electron Microscopy, Medical University Graz, Austria; 07.05.2015 – 08.05.2015.

W. Wallisch, M. Stöger-Pollach, G. Giannopoulos, S. Löffler, D. Niarchos, J. Fidler: *”Energy loss magnetic chiral dichroism analysis of carbon doped Co-Fe thin films”*; Poster: European Workshop on Quantitative STEM Imaging, EELS and EDXS (AdSTEM 2014), Piran, Slovenia; 29.09.2014 - 03.10.2014.

W. Wallisch, M. Stöger-Pollach, G. A. Zickler, G. Giannopoulos, D. Niarchos, J. Fidler: *”EMCD investigation of Co-Fe thin films doped with carbon by Analytical TEM”*; Poster: 18th International Microscopy Congress, Prague, Czech Republic; 07.09.2014 – 12.09.2014; in: “18th International Microscopy Congress Proceedings”, Czechoslovak Microscopy Society, (2014), ISBN: 978-80-260-6720-7; Paper ID MS-12-P-2050, 2 pages.

G. A. Zickler, W. Wallisch, M. Stöger-Pollach, J. Bernardi, K. Üstüner, J. Fidler: *”TEM investigation of grain boundaries from* $Nd_2Fe_{14}B$ *hard magnets”*; Poster: 18th International Microscopy Congress, Prague, Czech Republic; 07.09.2014 – 12.09.2014; in: ”18th International Microscopy Congress Proceedings”, Czechoslovak Microscopy Society, (2014), ISBN: 978-80-260-6720-7; Paper ID MS-12-P-1643, 2 pages.

G. Giannopoulos, C. Sarafidis, M. Gjoka, L. Reichel, A. Markou, W. Wallisch, V. Psycharis, J. Fidler, D. Niarchos: *”Rare Earth Free Permanent Magnets”*; Talk: REPM2014 - Rare Earth and Future Permanent Magnets and Their Applications Workshop 2014, Annapolis, USA; 17.08.2014 – 21.08.2014.

P. Toson, A. Asali, W. Wallisch, G. A. Zickler, J. Fidler: *"Nanostructured Hard Magnets: A Micromagnetic Study"*; Poster: 10th European Conference on Magnetic Sensors and Actuators (EMSA 2014), Vienna, Austria; 04.07.2014 - 09.07.2014.

W. Wallisch, G. A. Zickler, M. Stöger-Pollach, J. Bernardi, J. Fidler: *"Analytical TEM investigations of* $(Fe, Co)_{2-3}B$ *microcrystalline alloys"*; Poster: 4th ASEM-Workshop, University of Vienna, Austria; 08.05.2014 - 09.05.2014; in: "4th ASEM-Workshop on Advanced Electron Microscopy", (2014).

G. A. Zickler, K. Zagar, W. Wallisch, M. Stöger-Pollach, J. Bernardi, J. Fidler: *"Nanoanalytical TEM/STEM methods for the characterisation of grain boundary phases from rare earth permanent magnets"*; Poster: 4th ASEM-Workshop, University of Vienna, Austria; 08.05.2014 - 09.05.2014; in: "4th ASEM-Workshop on Advanced Electron Microscopy", (2014).

G. Giannopoulos, L. Reichel, A. Markou, S. Kauffmann-Weiß, I. Panagiotopoulos, K. Mergia, V. Psycharis, A. Lagogiannis, A. Edstrom, W. Wallisch, E. Delczeg, M. Werwinski, J. Rusz, S. Fähler, J. Fidler, D. Niarchos: *"Structural and magnetic properties of strongly carbon doped Fe-Co thin films"*; Poster: IEEE Int. Magnetics Conference (Intermag 2014), Dresden, Germany; 04.05.2014 – 08.05.2014.

W. Wallisch, P. Toson, A. Asali, H. Sassik, J. Fidler: *"Synthesis and analysis of* $(Fe, Co)_{2-3}B$ *microcrystalline alloys"*; Talk: JEMS 2013, Joint European Magnetic Symposia, Rhodes, Greece; 25.08.2013 – 30.08.2013.

P. Toson, A. Asali, W. Wallisch, J. Fidler: *"Simulation of hysteresis properties of realistically packed nanorod structures"*; Talk: JEMS 2013, Joint European Magnetic Symposia, Rhodes, Greece; 25.08.2013 - 30.08.2013.